Interface and Transport Properties of Fe/GaAs(001) Heterostructures

Luke Roger Fleet

Submitted for the Degree of Doctor of Philosophy

The University of York
Department of Physics

March 2012

Abstract

Fe/GaAs(001) is one of the leading candidate systems for achieving efficient spin-polarised injection. Although there have been numerous studies on the magnetotransport properties of Fe/GaAs(001) systems there is relatively little knowledge of the interface structure. In this study the atomic interface structure of Fe/GaAs(001) films has been investigated using both TEM and STEM techniques. The images show that as-deposited films consist of different interface structures. Although predominantly abrupt, the observation of partial mixing at the interface in some regions leads to a distribution of Schottky barrier heights. Ab-initio calculations were used to show that the partially mixed structure also forms interface resonance states. These states could provide a route for minority spin injection leading to bias dependent effects. Low temperature annealing has been shown to reduce the level of mixing in the films, thereby reducing the injection of minority spins through interface states. This explains the previously observed increase in injection efficiencies after annealing. Annealing also changes the shape of the Schottky barrier height distribution, explaining the increase in the effective Schottky barrier height after annealing. The magnetotransport properties of devices fabricated from the same film were investigated using both electrical and optical techniques. The magnetotransport properties show that reproducible devices can be created exhibiting well behaved characteristics, free from bias dependent phenomena. This is the first time that the atomic interface structure has been correlated to the magnetotransport properties in Fe/GaAs(001) films.

Contents

List of Figures

List of Tables

Acknowledgements

This thesis would not have been possible without the help and support of many people. I would first like to acknowledge my supervisors Prof. K. O'Grady, Dr. A. Hirohata and Prof. Y. Ohno for giving me the opportunity to work on this project. Without their guidance, continued support and excellent humours the last three years would have not have been possible.

I would like to thank the JST and the EPSRC for funding the past three years. I have also received funding from the IOP to attend various workshops. I am also grateful for the IEEE magnetics society for providing me the opportunity to attend the 2009 summer school in Nanjing, China.

During this work I was very fortunate to visit several labs. I would like to thank Prof. C. Barnes for allowing me access to the Cavendish laboratory, Prof. N. Tanaka for allowing me access to the Nagoya University & the JFCC and particularly Prof. H. Ohno for allowing me access to the facilities at the RIEC. I have been helped by so many students and postgraduates during my visits but I would like to give special mentions to H. Kurebayashi, H. Kobayashi, Y. Kaneko, S. Matsuzaka and particularly K. Yoshida.

I have to thank all of the students and visitors to SO20, past and present, who made my PhD years so enjoyable. There are too many people to name but I must give special mentions to Alex, Jay and Mike. Thank you for being such good friends.

Most of all I would like to thank my fiancé who has been there for me for so many years. Without her continued support none of this would have been possible. I cannot thank Carla enough. She is always there for me and always willing to help me, with anything! Thank you so much.

Declaration

I declare that the work presented in this thesis is based purely on my own research, unless otherwise stated, and has not been submitted for a degree in either this or any other university.

Signed

Luke Roger Fleet

April 2012

Chapter 1. Introduction

Since the discovery of giant magnetoresistance the field of spintronics has attracted considerable attention. Billions of GMR sensors can be found in hard drives around the world. The field of spintronics continues to expand and now consists of many sub-disciplines. Semiconductor spintronics offers the possibility of devices that combine magnetic recording and information processing into a single technology. One of the key requirements for semiconductor spintronic devices is efficient spin-polarised injection. This remains the greatest challenge in the field. Fe/GaAs(001) remains one of the leading candidate systems to achieve this feat but there are some key issues that need to be overcome if this system is to be utilised in future devices.

1.1 Spintronics

The integrated circuit has truly revolutionised technology and now finds its way into most aspects of modern living. Silicon complementary metal-oxide-semiconductor (CMOS) technologies, using both n and p-channel metal-oxide-semiconductor field effect transistors (MOSFETs) are the building blocks of the integrated circuit industry [1]. This field has undergone an astonishing advance in recent years driven largely by the ability to scale down the transistor size, thereby increasing the processing power. Moore's law, which states that the number of transistors on a single chip doubles every 18 months, has held true for over 30 years [2]. This trend, however, cannot continue. Soon devices will become so small that CMOS and MOSFET technologies will

no longer be able to function due to various factors such as high leakage currents and lithography limitations. A new technology is required to continue the rapid progress made in the semiconductor industry.

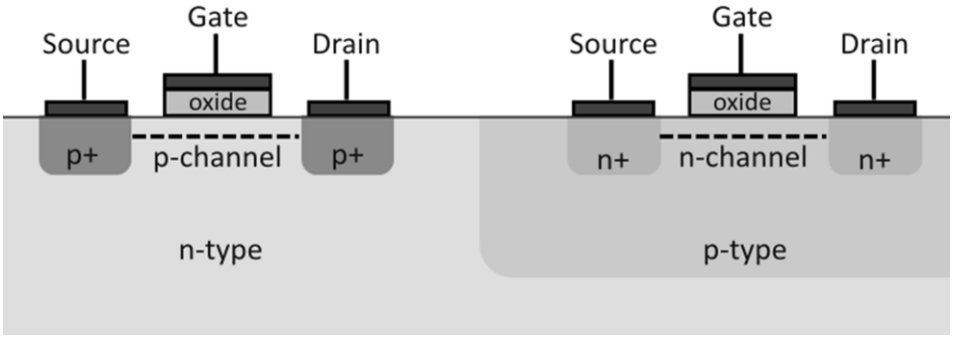

Figure 1.1 Schematic of MOSFET transistors used in CMOS technologies. A voltage is applied to the gate to alter the carrier concentration, altering the conductance of the channel [1].

It was early in the 20th Century that Pauli first pointed out that the electron as well as having a charge had another intrinsic property known as spin. The electron spin is quantised in units of angular momentum that can be thought of as being either up or down. This intrinsic two-state property of the electron offers great potential for new technologies [3]. Currently all semiconductor devices only make use of the charge of the electron. Spin electronics, or spintronics, is the field that aims to make use of the electron spin. Spintronics has grown considerably in recent years and has subsequently developed various sub-disciplines such as magnetoelectronics [4], concerned with all-metallic systems, and semiconductor spintronics which will be discussed in the next section [5].

The most basic effect in magnetoelectronics is magnetoresistance, of which there are several types. The first was discovered in 1857 by W. Thomson (later known as Lord Kelvin) [6] and is known as anisotropic magnetoresistance (AMR). AMR is present in all magnetic materials and is the directional dependence of the resistivity when the current travels at an angle to the magnetization, with contributions also arising from the magnetocrystalline anisotropy. Typically AMR is a very small effect (usually only a few percent) but AMR up to 50% has been observed in some Uranium compounds [7]. AMR was used in magnetic sensors for many years until the discovery of other magnetoresistive effects, particularly Giant Magnetoresistance (GMR).

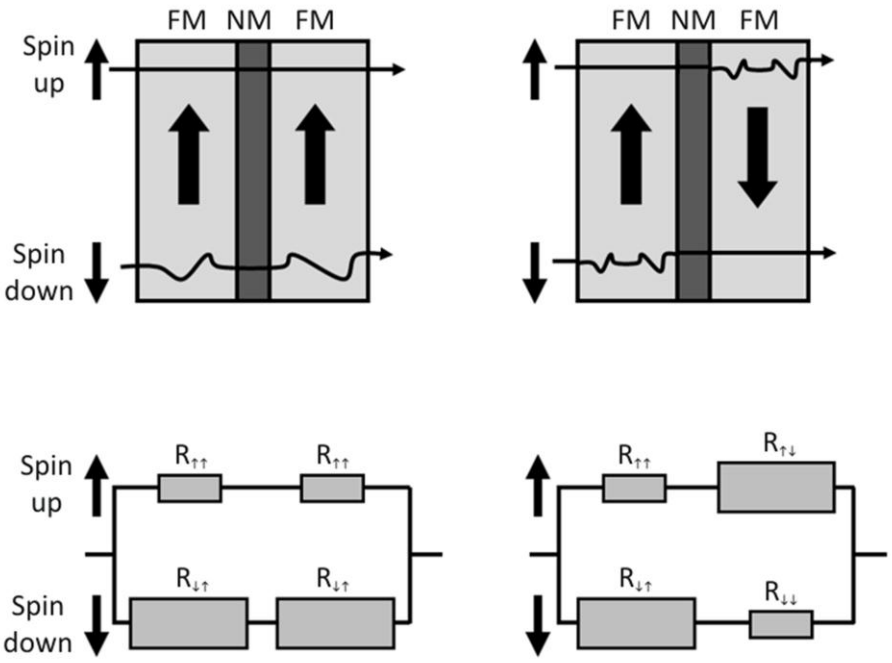

Figure 1.2 Schematic of GMR effect. For parallel alignment one spin orientation experiences a low resistance, giving a low resistance state, whilst for the antiparallel orientation both spins experience a high resistance, leading to a high resistance state [10].

GMR was discovered by Grunberg *et al.* [8] and Fert *et al.* [9] in the last 1980s, for which the pair received the 2007 Nobel prize in Physics. Since the discovery of GMR the field of spintronics has attracted increased attention and has grown considerably, discussed in detail in the review by Thompson [10]. Both of the initial discoveries were made with the observation of a large resistance drop in magnetic multilayer structures when the magnetisation of ferromagnetic layers, separated by a metallic spacer, went from an antiparallel to parallel alignment.

The first observation of spin dependent tunnelling between two ferromagnetic electrodes separated by a non-metallic spacer was actually observed by Julliere in 1975 [11]. This phenomenon is known as tunnelling magnetoresistance (TMR). Julliere performed measurements at 4.2K on a magnetic tunnel junction (MTJ), where the magnetic layers are separated by a thin insulating layer. The resistivity was found to vary by up to 14% between the antiparallel and parallel orientations of the magnetisation of the electrodes. This effect was not observed at room temperature for another 20 years due to the technological demands relating to the fabrication process [12, 13]. Developments by Ohno *et al.* using MgO tunnel barriers means TMR ratios of over 600% can now be achieved at 300K [14].

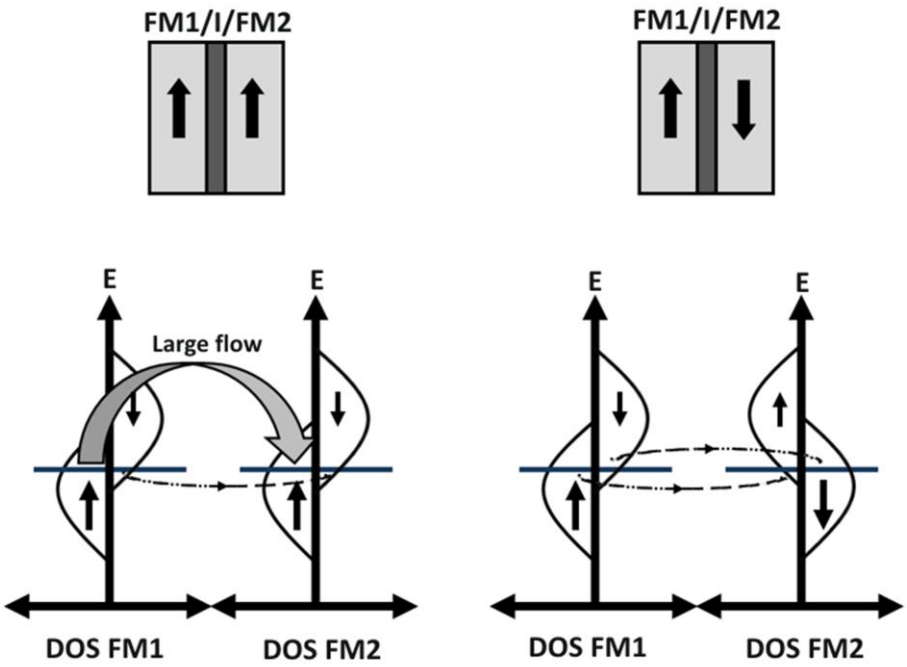

Figure 1.3 Schematic of the TMR effect. For the parallel orientation a large current can flow from FM1 to FM2 for the majority carriers, leading to a low resistance. All other channels have high resistance as there are few available states.

Despite being a relatively new field the principles used to describe these magnetoresistive effects have their origins in 1936. Sir Neville Mott used a two current model to explain the sudden decrease in the resistivity of ferromagnets as they cooled through the Curie point [15]. The two types of current each have their own independent channel, dependent upon their spin. This is known as the two-current model and has been extended by Campbell *et al.* [16] and Fert *et al.* [17] and can be used to explain the various magnetoresistive phenomena such as AMR, GMR and TMR.

1.2 Semiconductor spintronics

1.2.1 Historical overview

Semiconductor spintronics offers the possibility of the development of hybrid devices that could perform logic, communications and storage operations within the same materials technology. This could unify the information-processing and information-storage industries, which are based on semiconductor and magnetic thin film technologies respectively.

GaAs is particularly interesting for future device applications as it is a high electron mobility material. The electron mobility for GaAs with a doping density of $1x10^{16}$ cm^{-3} is ~5400 cm^2 $V^{-1}s^{-1}$ whereas for Si the mobility is just ~1400 cm^2 $V^{-1}s^{-1}$. A higher electron mobility allows for faster, lower-noise performance and high power performance devices [18]. There are, however, several advantages for Si: the native oxide forms a useful insulator, utilised in conventional devices; it has a higher hole mobility, useful for high-speed p-channel devices; it's also abundant and cheap to process. These advantages have helped keep Si at the forefront of device technologies. As the industry is now, more than ever, striving for high speed, low power devices the interest in GaAs is growing rapidly.

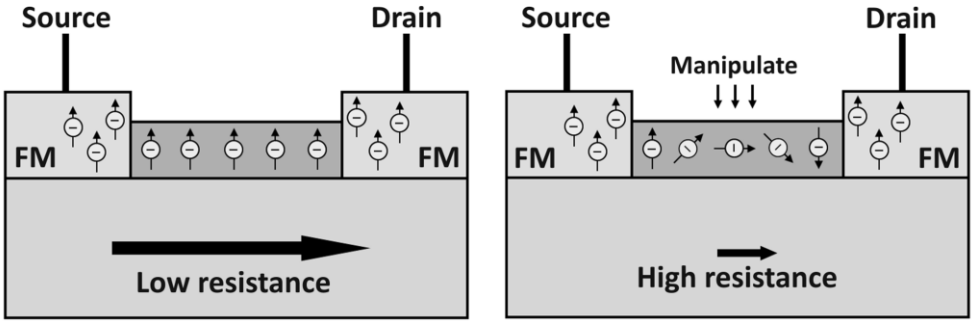

Figure 1.4 Schematic of spin-FET. Manipulating the spins to change the orientation allows the device to switch between high and low resistance states [19].

The first proposal for a semiconductor-based spin dependent device was put forward in 1990 by Datta and Das and is known as a spin-polarised field effect transistor (FET) or spin-FET [19]. The device consists of ferromagnet (FM) source and drain contacts, used for spin-polarised injection and detection, separated by a two-dimensional electron gas (2DEG), which provides high mobility and long electron spin lifetimes. Altering the spin orientation, by performing a gate manipulation (discussed in section 4.2), causes a change in the device resistance as the probability that the carrier is transmitted or reflected is dependent on the relative orientation of its spin compared to the drain FM electrode. Hence the spin-FET operates in a similar fashion to a conventional FET, in that the resistance is varied through a gate operation but the effect now arises due to a change in the spin orientation.

Since the proposal of the spin-FET there has been much interest in the operation of spin-polarised devices and various device concepts have been proposed such as

spin light emitting diodes (Spin-LED), spin resonant tunnelling diodes, coulomb blockade transistors, etc. [20]. There are four fundamental requirements for semiconductor spintronic devices. These are:

1. efficient electrical injection of spin-polarised carriers into a semiconductor
2. spin transport with sufficiently long spin lifetimes (~nanoseconds)
3. effective manipulation of the spin carrier to provide the desired functionality
4. efficient electrical detection of spin-polarised carriers

In order for a material to be suitable as a spin injector it must contain single orientation spin-polarised carriers, either electrons or holes, at room temperature. There have been many proposals for spin injectors but the most obvious choice is a ferromagnet due to their high Curie temperatures, low coercivities and fast switching times. Metallisation is also a standard process in many semiconductor device fabrication lines so a ferromagnetic metallisation step could easily be incorporated. There are, however, some problems with using an FM as a spin injector, many of which will be discussed in more detail in the following sections. The main problem is the so called 'conductivity mismatch' which occurs at the interface between an FM and a semiconductor (SC) [21]. If the contact between the FM and SC is perfectly Ohmic then the spin injection efficiency drops to almost zero. There are three possible solutions to this problem: use a 100% spin-polarised material as the injector; use a material with a similar conductivity to the semiconductor; or use a tunnel barrier [22, 23].

The first possible solution is to use a half metallic ferromagnet (HMF). The idea for HMFs was first discussed by de Groot *et al.* [24] in the early 1980s. HMFs are materials that possess a band-gap at the Fermi level for one of the spin sub-bands, generally the minority-spin sub-band, making them 100% spin-polarised. There are four different types of HMFs that have been predicted theoretically i.e. oxide compounds, perovskites, Zinc-blende compounds and Heusler alloys [25]. Although there is significant research being performed on HMFs, there are currently no reported systems that exhibit 100% spin-polarisation at room temperature [26].

The second possible solution is to use a magnetic material with a similar conductivity, such as a dilute magnetic semiconductor (DMS) or some oxide compounds. The most extensively studied DMS is Mn-doped GaAs [27] but the Curie temperature for such materials is still well below room temperature. The highest Curie temperature obtained for (Ga,Mn)As is 191K although this can enhanced to 200K in nanostructures due to the increased efficiency of post-growth annealing [28-30]. There are several proposals for enhancing the Curie temperature towards room temperature such as using a high-index substrate to increase the effective Mn concentration [31, 32] and co-doping of donors to reduce the self-compensating Mn interstitials [33-35]. Despite these proposals, creating ferromagnetic semiconductors capable of operating at room temperature remains a significant challenge.

Another solution is to use either an extrinsic or intrinsic tunnel barrier. The advantage of using a tunnel barrier is that it allows a conventional FM to be used as the source of spin-polarised electrons. Extrinsic barriers such as MgO have been studied by various groups and some promising systems have been reported such as CoFe/MgO/GaAs(001) [36]. Efficient room temperature spin injection does, however, remain elusive [26]. When a FM material is placed in contact with a SC an intrinsic barrier is formed, known as a Schottky barrier [1]. This intrinsic barrier overcomes the limitations of the conductivity mismatch without the need for the deposition of a tunnel barrier. For efficient electrical injection to be achieved uniform interfaces are required to preserve the Bloch states that arise from the periodic crystal [37]. Fe on GaAs remains one of the leading candidate materials for such a system due to the small lattice mismatch of less than 1.4% that exists between the materials, allowing for high quality epitaxial growth. Various groups have shown the potential for Fe/GaAs systems but there is still much that remains unknown, discussed in chapters 3 and 4. Calculations suggest that the spin injection efficiency could be enhanced when operating in the ballistic transport regime as the band structure mismatch between the FM and SC leads to spin filtering [38-40]. Despite the theoretical reports there have been no experimental studies using electrical methods to inject spin-polarised electron across the Fe/GaAs(001) interface using ballistic transport.

1.2.2 Experimental reports on Fe/GaAs(001) systems

The first demonstration of spin injection in Fe/GaAs was reported in 2001 by Zhu *et al.* [41]. In this study a spin-LED structure was used to perform optical injection and detection with an observed efficiency of approximately 2%. Spin polarisation efficiencies of up to 32% were observed by Hanbicki *et al.* in similar spin-LED structures using Fe/AlGaAs [42]. Although spin-LED experiments are very useful for understanding the physics behind spin injection the real aim is to achieve electrical injection, preferably at room temperature. The first detection of electrical spin injection was performed by Crooker *et al.* [43] who used optical techniques to image the spin accumulation in a GaAs channel of a lateral device at 4K. The first all-electrical injection and detection was performed by the same group in 2007 [44], with the signal detectable at temperatures up to approximately 100K. The study also showed a bias dependent polarisation inversion in two different electrical devices, the origins of which are not fully understood. One key piece of information that is lacking in these systems is knowledge of the interface structure.

There have been only two major experimental observations of the interface structure in Fe/GaAs(001) films. These reported interface structures differ greatly from those used for theoretical calculations [45-47]. Knowledge of the atomic interface structure, and its relationship to spin transport, is essential for the development of these systems [47]. The only report on the interface structure and subsequent effect on spin injection is that performed by Schultz *et al.* [48] in 2008. In their study the interface ordering at the Fe/GaAs(001) interface was explored for films where the Fe was grown at high temperatures or the structures post-annealed at high temperatures (above 400°C). It was found that annealing or growing at high temperatures can lead to the formation of the ferromagnetic Fe_3Ga phase which could cause a reversal of the spin polarisation. This report does not, however, explain the observed reversals from previous studies in which the growth was performed at much lower temperatures, around room temperature or below. The formation of FeGa compounds was not observed at these low growth temperatures. It is clear that other mechanisms are required to explain the phenomenon of a bias dependent polarisation inversion in

Fe/GaAs(001) systems. One further study which is crucial in understanding the origin of this effect was that performed by Moser *et al.* in 2006, who explored the transport across Fe/GaAs/Fe tunnel junctions [49]. In this study a polarisation inversion could be achieved but only when one of the interfaces was epitaxial. It is clear that greater knowledge of the atomic interface structure is required in order to develop this system further for potential applications, with the subsequent relationship to the spin transport of critical importance.

1.3 Notes on units and errors

In this thesis the metric international system (SI) of units has been used for all equations and calculations. The SI units are the standard system for the semiconductor spintronic field despite the significant overlap with the magnetic recording industry which uses Gaussian cgs units. The units of graphs are SI unless otherwise stated.

Where possible errors on numerical data displayed in graphs or tables has been calculated using standard Gaussian error techniques [50]. Where literature or book values are quoted without error this means that the error is not known.

Chapter 2. The Physics of Spin-polarised Injection

Despite the vast knowledge of the physics behind ferromagnetism the ability to inject the spin-polarised electrons from a ferromagnet into other materials remains challenging due to scattering at the interface. Advances in growth techniques allows for high quality epitaxial films to be fabricated but spin injection across a FM/SC interface remains limited due to the conductivity mismatch. There are several mechanisms that may overcome this problem. One possibility is to use the intrinsic Schottky barrier that forms at the interface.

2.1 Ferromagnetic materials for spin injection

2.1.1 Spin polarisation of ferromagnets

Ferromagnets are materials that exhibit spontaneous magnetisation. In transition metals ferromagnetism arises from a balance between the atomic-like exchange interaction, which tends to align the spins, and the inter-atomic hybridisation which tends to reduce spin polarisation. The Heisenberg exchange interaction is described by

$$E_{\mathrm{ex}} = -2J_{\mathrm{ex}}\boldsymbol{S}_i\boldsymbol{S}_j = -2J_{\mathrm{ex}}S_iS_jcos\theta \qquad (2.1)$$

where J_{ex} is known as the exchange integral and θ is the angle between spins S_i and S_j [51]. The energy gain from aligning the spins arises from the Pauli exclusion principle

which keeps the electrons with the same spin orientation further apart, on average, therefore lowering the Coulomb repulsion between them [52]. In transition metals, where the electron states can be described using band theory [53], the band structure will be determined by the competing exchange energy, which favours parallel spins, and the cost of filling electrons into one spin band.

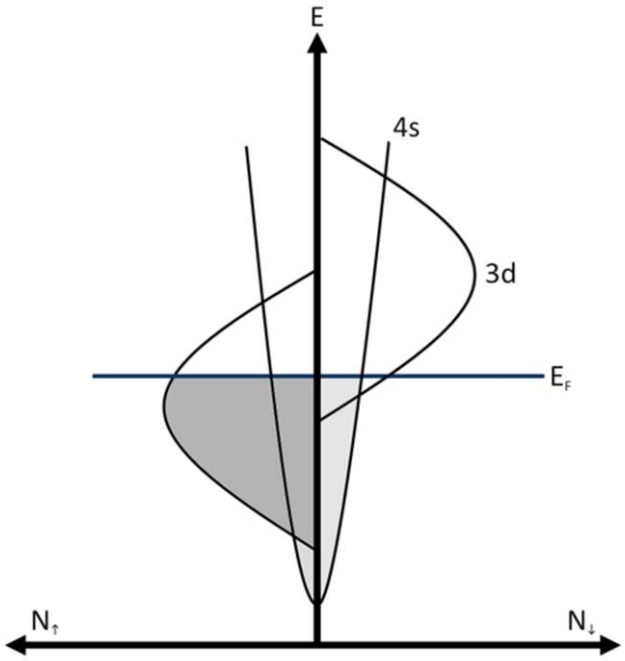

Figure 2.1 A simplified band structure for the ferromagnetic transition metals showing the splitting of the 3d band which gives rise to a non-equilibrium density of spins at the Fermi level [52].

For Fe, Ni and Co the energy gain from the exchange interaction is strong enough to support a splitting of the d-band leading to partially filled 3d and 4s bands. This split causes a unequal density of spin up and spin down electrons giving rise to a net magnetic moment per atom [52]. The conditions suitable for ferromagnetism to occur are described by the Stoner criterion

$$J_{\mathrm{ex}}(E_F)N(E_F) > 1 \qquad (2.2)$$

where $N(E_F)$ is the density of states (DOS) at the Fermi energy (E_F), measured in atom/eV [54]. The majority (minority) electrons represent the electrons in the spin band with highest (lowest) number of occupied states. From the Stoner criterion it can be seen that ferromagnetism will arise in materials which have a strong exchange integral and also a large DOS at the Fermi level. Detailed analysis of the exchange interaction for the transition metals can be found in O'Hanley [55]. The polarisation of a ferromagnet can be defined as the spin asymmetry in the DOS at the Fermi level

$$P = \frac{N_{\uparrow}(E_F) - N_{\downarrow}(E_F)}{N_{\uparrow}(E_F) + N_{\downarrow}(E_F)} \quad (2.3)$$

where $N_{\uparrow(\downarrow)}$ is the majority (minority) DOS. This is a useful definition when the states at the interface are of interest. The polarisation can be determined experimentally using magnetic tunnel junctions. If two ferromagnetic layers are separated by an insulating layer, the spin dependent tunnelling gives rise to a tunnelling magnetoresistance, described in chapter 1. The tunnel current depends directly on the density of states on either side of the tunnel barrier [56]. A simple model, developed by Julliere [11], relates the spin polarisation of the electrodes (P_1 and P_2) to the density of states by

$$TMR = \frac{\Delta R}{R} = \frac{R_A - R_P}{R_A} = \frac{2P_1P_2}{1 - P_1P_2} \quad (2.4)$$

where R_A is when the magnetic layers are antiparallel and R_P when they are parallel. If the polarisation of one of the electrodes is known it is therefore possible to estimate the polarisation of the other electrode from equation 2.4. The largest experimental value for the polarisation of Fe is ~45%, reported by Moodera *et al.* in 1999 [57]. This technique, along with Andreev reflection [58], is often used to characterise Heusler alloys, discussed further in chapter 8.

2.1.2 Magnetisation reversal in thin films

The magnetic moments in a material tend to align along preferred directions, a property known as magnetic anisotropy. Magnetic anisotropy has various origins such as from the sample shape, crystal symmetry, stress and exchange anisotropy [55]. The most important anisotropies for epitaxial thin films is the shape and magnetocrystalline anisotropy. The shape anisotropy ensures that the magnetisation lies in the plane and is also important when analysing nano- and micro-devices as the shape of contacts are often utilised when performing measurements. This is discussed in chapter 5.

Magnetocrystalline anisotropy arises from the spin-orbit interaction. Inside a crystalline solid the regular array of atoms gives rise to a periodic potential. This

potential causes the electrons' orbital angular momentum to effectively become fixed to the lattice. This means that there is no orbital contribution to the magnetic moment and that the electron orbitals are not significantly affected by applying a magnetic field. The spin-orbit interaction couples the electron spin angular momentum to the orbital angular momentum. As the orbital angular momentum is fixed to the lattice, this leads to preferential orientations with which the spin can align. It is worth noting that the spin-orbit interaction is relatively weak in comparison with the strong exchange interaction so the size of the fields required to align the spin along other axes is within experimental reach.

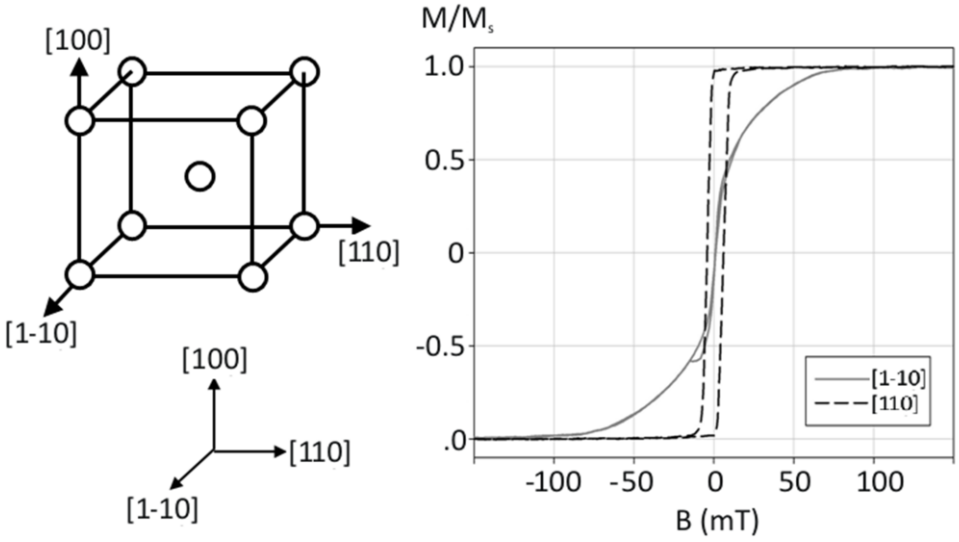

Figure 2.2 Schematic showing the effect of the axis convention for bcc Fe thin films and the hysteresis loops showing the magnetisation along the easy and hard axes (data).

Figure 2.2 shows the axis convention for Fe in thin film form along with hysteresis loops obtained from a 5nm film ([110] direction) of Fe grown onto a GaAs(001) substrate. The easy and hard axes are clearly visible from the loops with a field of only ~15 millitesla (mT) required to reverse the magnetisation along the easy axis, but over 90mT needed to reverse the magnetisation along the hard axis. When the Fe is magnetised along the hard axis there is energy stored in the crystal which is dependent on the uniaxial anisotropy, cubic anisotropy and shape anisotropy.

Shape anisotropy arises due to long-range magnetostatic interactions. A magnetised body produces magnetic charges/poles at the surface. The surface charges produce a field known as the demagnetising field H_D which acts in opposition to the magnetisation that produces it. Subsequently a sample will often break up into

domains in order to minimise the magnetostatic energy. For a prolate spheroid the shape anisotropy K_S is given by

$$K_s = \frac{1}{2}\left(N_{\text{short}} - N_{\text{long}}\right)M_s^2 \qquad (2.5)$$

where N_{short} and N_{long} are the shape demagnetising factors along the short and long axes respectively. It can be seen from equation 2.5 that the shape anisotropy depends on the square of the magnetisation. In materials such as Fe where M_s is as large as 1.714 x10^6 Am^{-1} the shape anisotropy plays a crucial role, particularly as the first order magnetocrystalline anisotropy constant is relatively small in comparison: 4.80 x 10^4 Jm^{-3} [52]. Haematite on the other hand, which has a hexagonal crystal structure, has a magnetisation of 2 x10^3 Am^{-1} and a first order uniaxial anisotropy constant much greater: 1.2 x 10^6 Jm^{-3}. The magnetocrystalline anisotropy is therefore dominant in Haematite [59].

Between domains there is a transition region where the magnetisation orientation changes smoothly, known as a domain wall. In thin films Néel walls [60] are the most favourable due to the large demagnetising field for spins orientated out of the plane. The width of the domain wall is dependent upon the magnetocrystalline anisotropy, which tries to align the spins along the easy axis, and the exchange interaction, which favours a parallel spin alignment. The magnetisation and domain structure inside a thin film is therefore a balance between the exchange, magnetocrystalline and shape anisotropies. A detailed investigation into the effect of the dimensions of patterned structures on the crystal, uniaxial and shape anisotropies in epitaxial Fe/GaAs(001) films was performed by Meng *et al.*, in 2010 [61].

Looking again at figure 2.2 it can be seen that only a small field of ~10 mT is required to nucleate a domain wall in a thin film of Fe. As the film is a single crystal, shown in chapter 6, it contains very few defects. Hence the domain walls are able to propagate easily leading to the small coercivity observed along the easy axis. The effect of patterning the film to create electrical contacts, inducing strong shape anisotropy, will be discussed in chapter 6.

2.2 Theories of spin injection

2.2.1 The electrochemical potential

Before discussing the theory of spin injection across a FM/SC interface it is first necessary to discuss the concept of the chemical and electrochemical potentials. The chemical potential μ_{ch} is defined as the energy required to add an atom to a system. So a system that is in thermodynamic equilibrium has a constant chemical potential. If two systems with different chemical potentials are placed in contact then the chemical potential gradient provides a driving force, producing electron/hole transport. It is conventional to set the chemical potential for an electron at the Fermi surface equal to zero. Small deviations from equilibrium ($\Delta\mu << E_F$) can then be described by the relationship of the excess particle density n above the Fermi level to the density of states at the Fermi energy $N(E_F)$.

$$\mu_{ch} = \frac{n}{N(E_F)} \tag{2.6}$$

As well as kinetic energy an electron also has potential energy. If a system is kept at a constant electrostatic potential difference V it can now be described by the electrochemical potential μ given by

$$\mu = \mu_{ch} - eV \pm \frac{1}{2} g\mu_B B \tag{2.7}$$

where g is the gyromagnetic ratio, e the electronic charge, μ_B the Bohr magneton and B is an applied magnetic field. The term $1/2g\mu_B B$ is the conventional Zeeman energy. As the electrochemical potential is related to the electron density, a gradient in the electrochemical potential provides a driving force leading to diffusion induced electron transport. A gradient in the electrochemical potential is easily measured experimentally as this is the property of the system measured by a voltmeter.

2.2.2 Spin dependent conductivity

If a voltage is applied across a conventional system, the rate of charge flow can be described by the drift and diffusion terms

$$\boldsymbol{j} = \sigma \boldsymbol{E} + eD\nabla\delta n \tag{2.8}$$

where $\boldsymbol{j}$ is the current density, σ the conductivity, $\boldsymbol{E}$ the applied electric field, D the diffusion constant and δn is the change in the carrier density from equilibrium. The first term is Ohm's law which describes the carrier drift, with the second term describing the diffusion of non-equilibrium carriers. This simple model does not, however, take into account the two different spin populations. In ferromagnetic materials the transport equation can be separated into spin dependent channels

$$\boldsymbol{J}_{\uparrow(\downarrow)} = \sigma_{\uparrow(\downarrow)}\boldsymbol{E} + eD_{\uparrow(\downarrow)}\nabla\delta n_{\uparrow(\downarrow)} \tag{2.9}$$

where the symbols have the same meaning as above but are now spin dependent. This idea of two independent conduction channels is called the "two current model" [15-17], discussed in chapter 1.

This idea can be extended to the chemical potential, discussed in the last section, which can also be separated to describe the two spin channels.

$$\mu_{\uparrow(\downarrow)} = \frac{n_{\uparrow(\downarrow)}}{N(E_F)_{\uparrow(\downarrow)}} \tag{2.10}$$

where $N(E_F)_{\uparrow(\downarrow)}$ are the spin dependent excess particle density $n_{\uparrow(\downarrow)}$ and density of states at the Fermi energy. It can be seen from equation 2.10 that if the spins in a non-magnetic material, such as GaAs, are driven out of equilibrium a change in the electrochemical potential occurs. This can be utilised to detect the spin imbalance.

2.2.3 Ferromagnetic/Semiconductor junctions

There are several models that can be used to describe the transport across FM/SC junctions [21]. The method described here is based on that of Smith and Silver

[62]. If it is assumed that the interface resistance gives rise to a spin dependent interface conductivity, then the current flowing across the interface is given by

$$j_{\uparrow(\downarrow)} = \sigma_{\uparrow(\downarrow)} \frac{\nabla \mu_{\uparrow(\downarrow)}}{e} \tag{2.11}$$

where e is the electron charge, $\sigma_{\uparrow(\downarrow)}$ is the interface conductivity (so 1/ $\sigma_{\uparrow(\downarrow)}$ the interface resistivity) and $\Delta\mu_{\uparrow(\downarrow)}$ is the interface discontinuity in the electrochemical potential for the two spin channels, shown in figure 2.3.

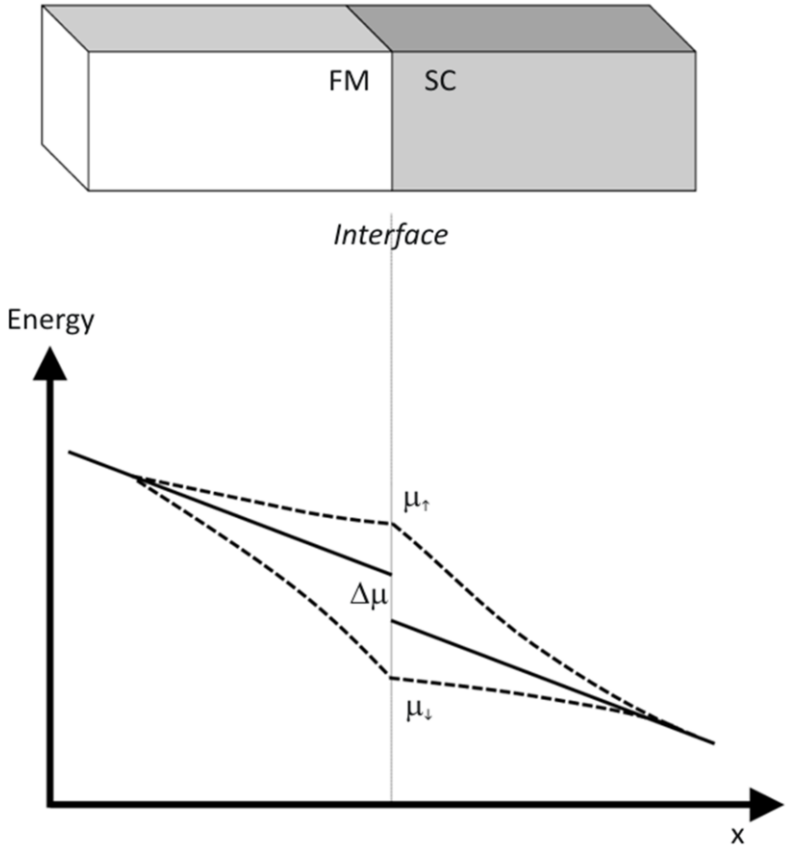

Figure 2.3 Typical slope of the electrochemical potential at the FM/SC interface. The solid line represents the average chemical potential [62].

To achieve spin injection into the semiconductor the system must be driven out of equilibrium by passing an electric current. For a steady state current it is convenient to define a parameter η such that:

$$\boldsymbol{j}_{\uparrow} = \eta \boldsymbol{j} \qquad\qquad \boldsymbol{j}_{\downarrow} = (1-\eta)\boldsymbol{j} \tag{2.12}$$

where $\boldsymbol{j}$ is the total current density. If the total conductivity is fixed and independent of the current density, then a variable α can be defined such that:

$$\boldsymbol{\sigma}_{\uparrow} = \alpha\boldsymbol{\sigma} \qquad \boldsymbol{\sigma}_{\downarrow} = (1-\alpha)\boldsymbol{\sigma} \tag{2.13}$$

where $\boldsymbol{\sigma}$ is the total conductivity. It should be noted that η is continuous at the interface but as the electron density is much greater in the metal than in the semiconductor α is not constant. In the semiconductor α is taken to be a function of current density and position, given the symbol α_s. At the contact α is assumed to be independent of both the position and the current density, given the symbol α_c.

If electrons with different spins are driven out of equilibrium the chemical potential relaxation is described by the diffusion equation

$$\frac{\partial(\mu_{\uparrow}-\mu_{\downarrow})}{\partial x^2} = \frac{(\mu_{\uparrow}-\mu_{\downarrow})}{\lambda} \tag{2.14}$$

where λ is the spin diffusion length. If suitable boundary conditions are applied such that the change in the chemical potential far from the interface is zero $\mu_{\uparrow}(\pm\infty)$-$\mu_{\downarrow}(\pm\infty)=0$ then solutions to the diffusion equation have the form

$$(\mu_{\uparrow} - \mu_{\downarrow}) = A_1 exp\left(\frac{x}{\lambda_c}\right) \tag{2.15a}$$

$$(\mu_{\uparrow} - \mu_{\downarrow}) = A_2 exp\left(\frac{x}{\lambda_s}\right) \tag{2.15b}$$

where $\lambda_{c(s)}$ are the spin diffusion lengths at the contact and in the semiconductor. The relationship between coefficients A_1 and A_2 can be obtained from equation 2.11 giving

$$A_2 - A_1 = ej\left[\eta\left(\frac{1}{\sigma_{\uparrow}} + \frac{1}{\sigma_{\downarrow}}\right) - \frac{1}{\sigma_{\downarrow}}\right] \tag{2.16}$$

Evaluation of the drift-diffusion equation $\frac{\partial(\mu_{\uparrow(\downarrow)})}{\partial x^2} = \frac{ej_{\uparrow(\downarrow)}}{\sigma_{\uparrow(\downarrow)}}$ for the two sides of the interface gives

$$\frac{ej}{\sigma_c}\left[\frac{\eta-\alpha_c}{\alpha_c(1-\alpha_c)}\right] = \frac{A_1}{\lambda_c} \tag{2.17a}$$

$$\frac{ej}{\sigma_S}\left[\frac{\eta-\alpha_S}{\alpha_s(1-\alpha_s)}\right] = \frac{A_2}{\lambda_s} \tag{2.17b}$$

where α and η are evaluated at the interface. Equations (2.16) and (2.17) can be solved to give the injected current polarisation

$$j_{\uparrow} - j_{\downarrow} = \frac{(2\alpha_c - 1)R_c + (2\alpha_s - 1)R_s + \left({}^{1}/_{\sigma_{\downarrow}}\right) - \left({}^{1}/_{\sigma_{\uparrow}}\right)}{R_c + R_s + \left({}^{1}/_{\sigma_{\downarrow}}\right) + \left({}^{1}/_{\sigma_{\uparrow}}\right)} \tag{2.18}$$

where position dependent quantities are given by

$$R_c = \frac{\lambda_c}{\sigma_c \alpha_c (1 - \alpha_c)} \tag{2.19a}$$

$$R_s = \frac{\lambda_s}{\sigma_s \alpha_s (1 - \alpha_s)} \tag{2.19b}$$

It can be seen from equation (2.18) that in the case of a perfect Ohmic contact, where R_c=0, the spin injection efficiency drops off rapidly as $R_c << R_s$. This is known as the conductivity mismatch problem [21]. For a low resistance interface the FM and SC are in good thermal contact, so the electrons stay in local equilibrium. This means that it is difficult to drive electrons away from local quasithermal equilibrium. As the semiconductor has the same density of states for both spin types it is difficult to achieve strong spin injection without extremely large current densities. If the interface resistance is large (~ several hundred Ohms) then electrons on the two sides of the interface are not in good thermal contact. This allows for the spin populations in the semiconductor to be driven out of local quasithermal equilibrium allowing for efficient spin injection. The different mechanisms to overcome the conductivity mismatch problem were first proposed by Rashba in 2000 [22], discussed in chapter 1.

Chapter 3. Transport Across Schottky Barriers

In order to achieve efficient electrical injection from Fe into GaAs(001) a resistive interface is required. When Fe is in contact with GaAs an intrinsic Schottky barrier is formed. Although the transport mechanisms across Schottky barriers were studied several decades ago, new mechanisms observed in Fe/GaAs(001) films are proving problematic for device characteristics and reproducibility.

3.1 The Schottky barrier

3.1.1 Schottky barrier formation

Metal-semiconductor (Metal/SC) junctions were first studied as early as 1875 by Braun [63] who reported on the rectifying properties of copper, iron and lead sulphide crystals. The first major step in the understanding of Metal/SC contacts was through the work performed independently by Schottky [64] and Mott [15, 65] in the late 1930s. It was Schottky who first proposed the existence of a potential barrier at the Metal/SC interface, leading to the unusual rectifying characteristics; this potential barrier is therefore known as the “Schottky barrier”. Schottky and Mott subsequently explained the mechanism of the barrier, and its formation, and also proposed various models for the calculation of parameters such as the barrier shape and height. These simple models were advanced further [66, 67] so that by the early 1940s the

rectification process for most experimental situations could be explained. The formation of the potential barrier, as first proposed by Schottky, is shown in figure 3.1. The intrinsic barrier arises from the fact that a metal and semiconductor have different Fermi energies. When a metal is placed in contact with an n^-doped semiconductor, with a Fermi level $E_{F(SC)}$ that lies close to the bottom of the conduction band (E_C), electrons flow across the interface in order to bring the Fermi levels into coincidence. It should be noted that the electron affinity χ_s is defined as the difference between the bottom of the conduction band and the vacuum level.

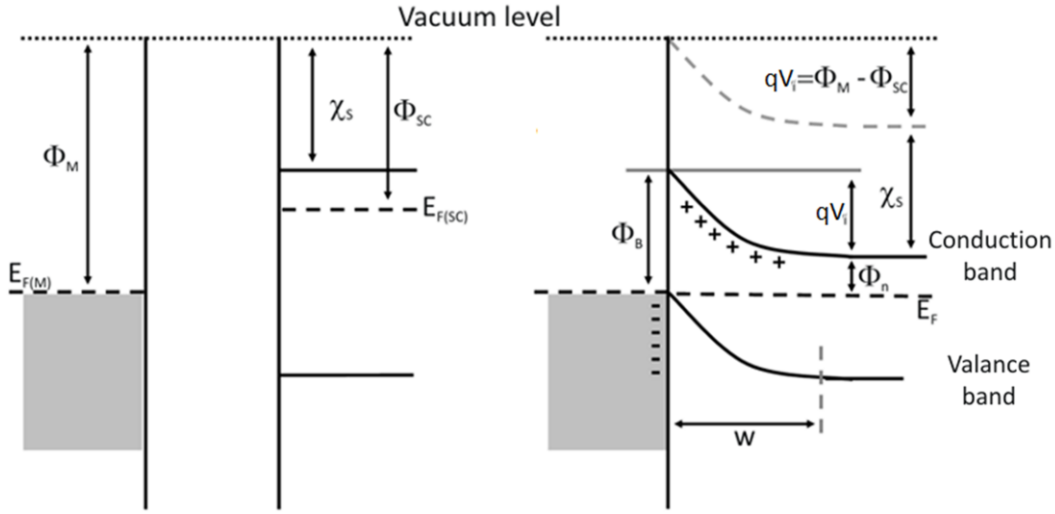

Figure 3.1 Schematic showing the formation of a Schottky barrier at the contact between a metal and a semiconductor [1].

For FM/SC contacts using *n*-type semiconductors, such as the Fe/GaAs(001) junctions explored in this study, electrons will flow from the conduction band of the SC into the metal as they have higher energies. The flow of electrons from the semiconductor causes a depletion of carriers close to the interface, causing the conduction band edge to bend up. This gives rise to an intrinsic potential barrier with a height, known as the Schottky barrier height (Φ_B), given by

$$\Phi_B = qV_i - \Phi_n \tag{3.1}$$

where $qV_i = \Phi_m - \Phi_{SC}$ is difference in the work functions of the metal (Φ_m) and semiconductor(Φ_{SC}) and $\Phi_n = E_c - E_{F(SC)}$ is the penetration of the Fermi level in the band gap of the semiconductor. If the depletion region is assumed to be fully depleted of carrier, so there is full ionization of the dopant impurity levels, then the width of the depletion region (w) can be described using the Poisson equation

$$w = \sqrt{\frac{2\varepsilon_{SC}\,(\Phi_B - V)}{qN_d}} \tag{3.2}$$

where ε_{SC} is the semiconductor permittivity, N_d the doping density and V the applied voltage. This model is known as the full depletion approximation and also assumes that due to the high number of free carriers in the metal there is no charge layer on the metal side of the barrier, so the depletion region occurs only on the side of the semiconductor [1].

The Schottky relationship shown in equation (3.1) suggests that there should be a strong dependence of the barrier height on the metal work function. This is not the case, however, as experiments with some semiconductors have shown an independent relationship between the barrier height and the metal work function. The first model proposed to explain this behaviour was that of Bardeen [68] who in 1947 discussed the pinning of the barrier height due to gap states (states which form in the forbidden gap of the bulk semiconductor). There are various sources of gap states arising from surface states [68], metal induced gap states (MIGS) [69], defect related states [70], disordered gap states (DIGS) [71] and the polarisation of chemical bonds [72]. Regardless of the origin of the gap states they lead to a pinning of the Fermi level, therefore systems show only a weak dependence of the barrier height on the metal work function. Strong Fermi level pinning is referred to as the Bardeen limit.

3.1.2 Schottky barrier bias dependence

Electrons within an Fe/GaAs(001) Schottky junction are able to flow from the GaAs into the Fe or from the Fe into the GaAs. The convention is that a junction which is forward (negative) biased has electrons flowing from the metal into the semiconductor. If the junction is reverse (positive) biased then electrons will flow from the semiconductor into the metal. For the case of Fe/GaAs(001), as the Fe is ferromagnetic, forward bias leads to spin injection whilst reverse bias leads to spin extraction. In consequence a spin accumulation occurs in the GaAs.

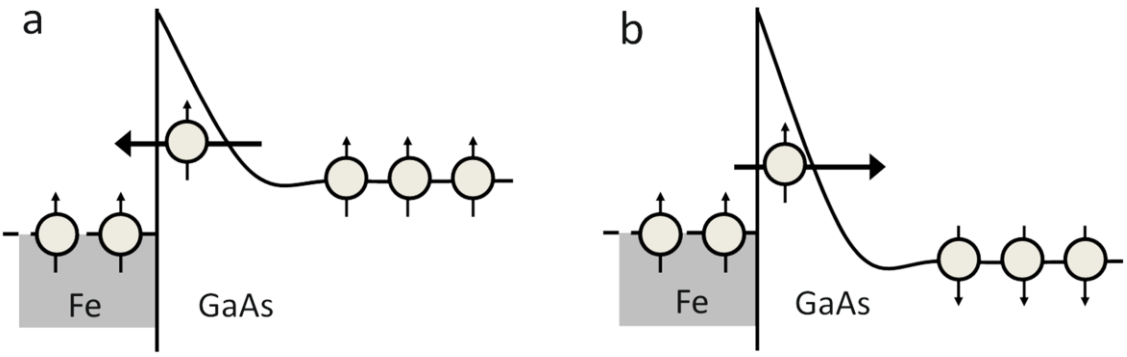

Figure 3.2 Schematic showing a) the injection of spin-polarised carriers for forward bias and b) the extraction of spin-polarised carriers for reverse bias.

Applying a voltage will also change the shape and height of the barrier. If a bias voltage V is applied then the conduction band minimum the value of E_C is modified such that it tends to $E_C - qV(1 - e^{-x/\lambda_e})$, where λ_e is the electron diffusion length and x the distance from the interface. If the junction is reverse biased E_C increases, leading to a lower barrier potential but a larger depletion width. If the junction is forward biased then E_C is reduced leading to a higher barrier potential but a smaller depletion width. It should be noted that the bias dependence of the barrier width is much smaller than the effect on the barrier height.

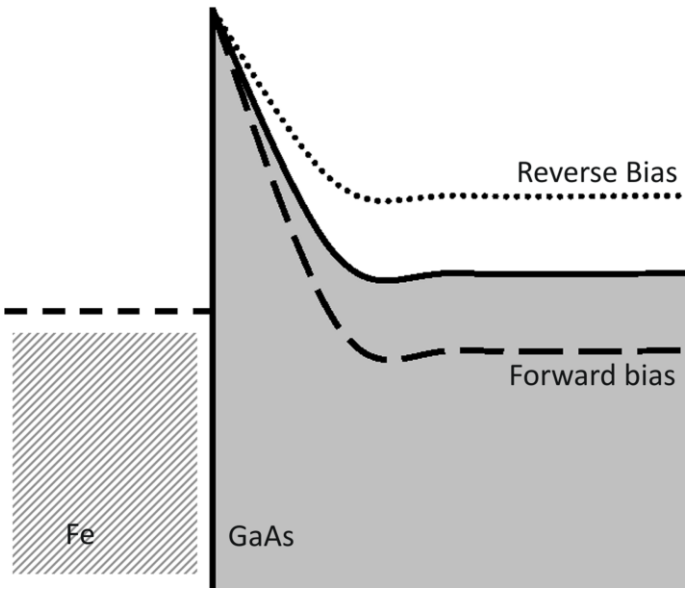

Figure 3.3 Schematic showing the effect of forward and reverse bias on the conduction band across a Schottky barrier.

3.2 Transport Mechanisms

3.2.1 Thermionic emission

Thermionic emission occurs when electrons have enough energy to be emitted over the barrier. Early models of this type of transport performed by Schottky and Spence [66] giving the thermionic emission current

$$I = I_{0_{\mathrm{TE}}}\left[\exp\left(\frac{qV}{n_{\mathrm{ideality}}k_{\mathrm{B}}T}\right) - 1\right] \tag{3.3}$$

where $I_{0_{\mathrm{TE}}}$ is the saturation current, V the applied voltage, T the temperature, q the electron charge, k_{B} Boltzmann's constant and n_{ideality} is known as the idealist factor which gives a measure of the quality of the junction. If a Maxwellian distribution of electron velocities in the semiconductor is assumed, the saturation current I_0 can be expressed as:

$$I_{0_{\mathrm{TE}}} = SAT^2\exp\left(-\frac{\Phi_B}{k_{\mathrm{B}}T}\right) \tag{3.4}$$

where S is the diode area, T the temperature, Φ_B the barrier height, V the applied bias voltage and A is known as the Richardson constant.

The most complete treatment of thermionic emission across Schottky barriers is that of Crowell and Sze [73] which takes into account effects such as electron collisions, image force barrier lowering, optical phonon scattering in the metal and quantum mechanical reflections from the barrier. In the high energy/temperature regime, ensuring thermionic emission dominates, this model can be simplified to the thermionic emission model of Schottky and Spenke but with an effective value for the Richardson constant, A^*, given by

$$A^* = \frac{Af_pf_q}{1+f_pf_q{}^{v_R}/_{v_D}}SAT^2\exp\left(-\frac{\Phi_B}{k_{\mathrm{B}}T}\right) \tag{3.5}$$

where f_p and f_q are the probabilities of transmission and reflection respectively, typically of the order of 0.5; v_R is the recombination velocity; and v_D is the drift velocity. The calculated value of the effective Richardson constant, A^*, for GaAs is 4.4 $\mathrm{Acm^{-2}K^{-2}}$ at 300K.

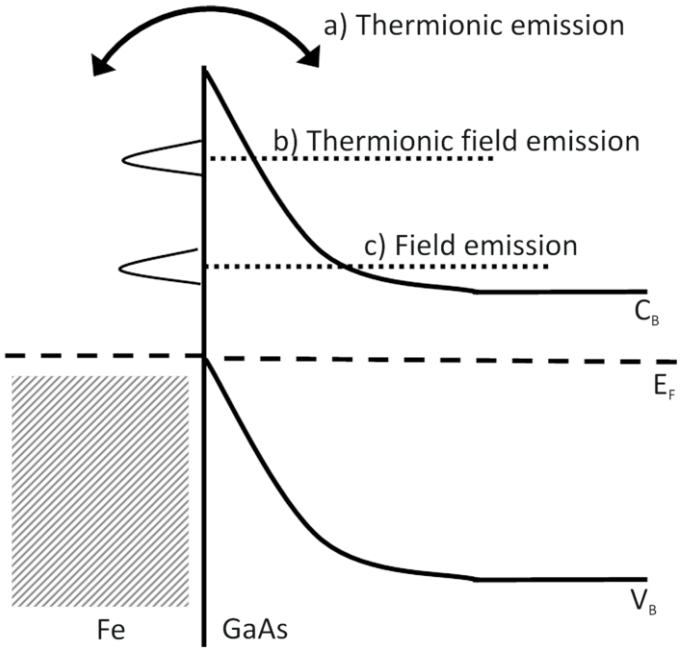

Figure 3.4 Schematic showing the main transport mechanism across Schottky barriers a) Thermionic emission b) Thermionic field emission and c) field emission.

Thermionic emission is expected to be the dominant transport mechanism across lightly doped ($n < 1x10^{16}$ cm^{-3}) FM/SC junctions. In these junctions the model above is often used to calculate the barrier height, usually through plotting I_0/ST^2 against $1/T$ known as a Richardson Plot. The barrier height can be calculated from the slope which is equal to $(-q\Phi_B/k_B)$. This model cannot be used for junctions with high doping concentrations as other transport mechanism become dominant.

3.2.2 Thermionic field and field emission

For moderate to heavily doped semiconductors, where the depletion region becomes very narrow (which is often the case when performing spin injection experiments) or for operations performed at low temperatures the dominant transport mechanism is tunnelling. Thermionic field emission is the tunnelling of carriers towards the top of the barrier, where the barrier is very thin.

Tunnelling through the barrier was first analysed in the late 1960's [74, 75] with the forward bias current-voltage *(I-V)* characteristics described by the relation

$$I = I_{0_{\mathrm{TFE(F)}}} \exp\left(\frac{qV}{E_0}\right) \tag{3.6}$$

where $I_{0_{\mathrm{TFE(F)}}}$ is the saturation current for thermionic field emission and E_0 is the tunnelling constant, given by

$$E_0 = E_{00} \coth\left(\frac{E_{00}}{k_{\mathrm{B}}T}\right) \tag{3.7}$$

E_{00} is a tunnelling parameter that is inherently related to the material properties of the semiconductor given by

$$E_{00} = \frac{qh}{4\pi}\left(\frac{N_d}{m^*\varepsilon_s}\right)^{\frac{1}{2}} \tag{3.8}$$

where N_d is the doping concentration, m^* the effective mass of the electrons and ε_s the static dielectric constant.

For reverse bias, the probability of an electron tunnelling into the semiconductor is increased. The current-voltage characteristics for reverse bias can be described by

$$I = I_{0_{\mathrm{TFE(R)}}} \exp\left(\frac{qV}{\epsilon'}\right) \tag{3.9}$$

where $I_{0_{\mathrm{TFE(R)}}}$ is the saturation current for reverse bias and ε' is the tunnelling parameter under reverse bias given by

$$\varepsilon' = E_{00}\left[\frac{E_{00}}{k_{\mathrm{B}}T} - \tanh\left(\frac{E_{00}}{k_{\mathrm{B}}T}\right)\right]^{-1} \tag{3.10}$$

There is another type of tunnelling that can occur across Schottky barriers known as field emission. Field emission is the process by which electrons tunnel through the barrier close to the Fermi level. This is a particularly important mechanism when dealing with degenerate semiconductors with a small effective mass, such as GaAs. The level of thermionic field emission to field emission is described by the tunnelling parameter E_{00}. If E_{00} is much larger than k_BT then field emission will dominate. The current voltage characteristics for field emission are given by equations of the same form as equations (3.6) and (3.9) but with the saturation current given by I_{SFF} and reverse saturation current by I_{SFR} leading to

$$I = I_{0_{\mathrm{FE(F)}}} \exp\left(\frac{qV}{E_0}\right) \tag{3.11}$$

$$I = I_{0_{\mathrm{FE(R)}}} \exp\left(\frac{qV}{\epsilon\prime}\right) \tag{3.12}$$

To determine properties such as the barrier height or barrier thickness the Brinkman-Dynes-Rowell (BDR) [76] or Simmons [77] models can be applied. These models use the equations above to determine the conductance across the junctions. The BDR model assumes an asymmetrical barrier, giving the conductance by

$$G(V) = G_0\left[1 - \left(\frac{A_0\Delta\Phi_{12}}{16\Phi_{eff}^{3/2}}\right)eV + \left(\frac{9}{128}\frac{A_0^2}{\Phi_{\mathrm{eff}}}\right)(eV)^2\right] \tag{3.13a}$$

where $$G_0 = \left(\frac{q^2}{t_{SB}h^2}\right)\sqrt{2qm_e\Phi_{\mathrm{eff}}}\exp\left(-\frac{t_{SB}\sqrt{8m_e e\Phi_{\mathrm{eff}}}}{\hbar}\right) \tag{3.13b}$$

with $$\Delta\Phi_{12} = \Phi_2 - \Phi_1 \tag{3.13c}$$

$$A_0 = \frac{4t_{SB}\sqrt{2m_e}}{3\hbar} \tag{3.13d}$$

where Φ_1 is the barrier potential on the FM side, Φ_2 the barrier potential on the SC side, t_{SB} the barrier thickness, m_e the electron mass, Φ_{eff} the effective barrier height and e the electronic charge. The main problem when trying to employ this or the Simmons model is that the contribution to the conductance from the different transport mechanisms is not known. It is also possible that small pinholes are present, effectively shorting the tunnelling current.

To determine if tunnelling is the dominant transport *I-V-T* curves are sometimes analysed using the Rowell criteria [78]:

1. The conductance ($G = dI/dV$) should have an exponential dependence on the barrier thickness.
2. The conductance should have a parabolic dependence on the voltage and can be fitted to known models such as BDR or Simmons.
3. The zero-bias resistance (ZBR) should exhibit a weak, insulating-like, temperature dependence.

Although the Rowell criteria can be used to determine if tunnelling is the dominant mechanism, it is still very difficult to determine the exact contributions to the conductance from the different transport mechanisms.

For the samples presented in this study a highly doped n^+GaAs layer is used to ensure a thin barrier, approximately 12nm thick, is formed at the Fe/GaAs(001) interface. With such a thin barrier the dominant transport mechanisms are therefore expected to be thermionic field and field emission. The BDR model should therefore be able to be fit to the data to extract the barrier properties. There are, however, additional mechanisms, discussed in section 3.3, that can dominate the transport properties across the Fe/GaAs(001) interface. When taking into account the additional mechanisms it makes it very difficult to extract the barrier properties using conventional models. This is discussed further in chapter 7 when the transport properties are presented.

3.2.3 Image force lowering

The height of the Schottky barrier can be significantly lowered due to image forces. If an electron is at a distance *x* from the metal surface, a positive charge *q* will be induced in the metal at a distance -*x*. The image force is defined as the force between the electron and the positive charge.

$$F_{\text{image}} = \frac{q^2}{4\pi\varepsilon_s(2x)^2} \tag{3.14}$$

This leads to an image force potential that acts to lower the barrier height, given by

$$\Phi_{\text{image}} = -\frac{q^2}{16\pi\varepsilon_0 x} \tag{3.15}$$

where ε_0 is the permittivity of free space.

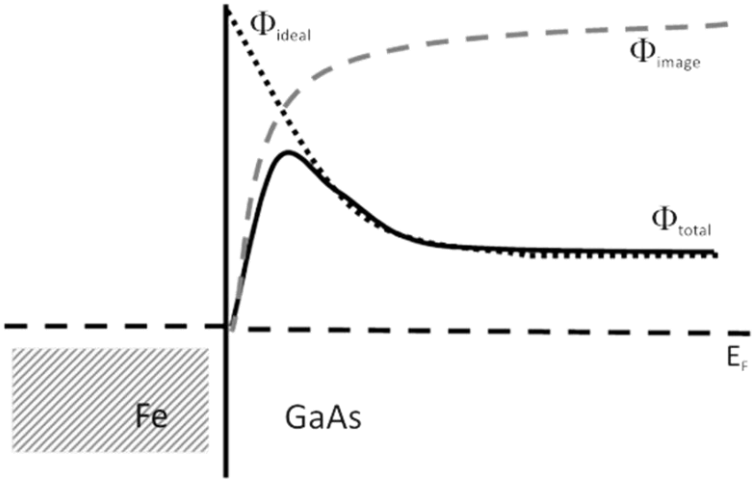

Figure 3.5 Schematic showing the effect of the image force on the Schottky barrier height. The black short dashed line represents the Schottky barrier with no image force lowering, the grey long dashed line shows the image force potential and the solid black line shows the total barrier potential.

This potential does however tend to be very small, typically <0.05eV for x~10nm, when compared to the height of the barrier, ~0.8eV. If an electric field is applied an increase in the electron flow across the barrier occurs, so the image force potential increases. Hence the image force can significantly lower the barrier height at large bias voltages. Image force lowering therefore adds further complexity when trying to determine the Schottky barrier height.

3.3 Bias dependence of the spin polarisation

Recent experimental work in Fe/GaAs films has shown that the spin polarisation of injected/extracted carriers can vary significantly and even change sign, depending on the applied bias voltage. The first observation of an apparent reversal in the current polarisation was observed by Crooker *et al.* in 2005 [43]. In this study scanning Kerr microscopy was used to demonstrate spin injection across the Fe/GaAs(001) interface in 2-terminal devices. The report showed that for both forward and reverse bias a small spin accumulation occurred under the non-injector contact with the same sign of the accumulated spins under the injector contact, shown in figure 3.6. The sign of the accumulation was attributed to reflection off the contact but further investigations, performed by the same group, showed that a polarisation inversion could also be detected using an all-electrical set-up.

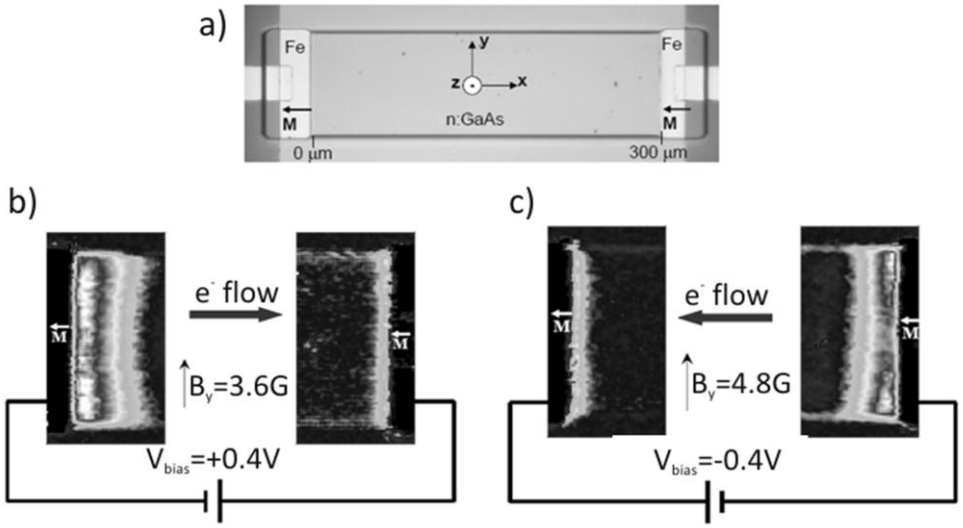

Figure 3.6 a) Device configuration and Kerr microscopy signals reported by Crooker *et al.* for a) reverse and b) forward bias [43].

In 2007 Lou *et al.* [44] used the conventional Hanle and spin-valve effects to explore the transport properties of 5-terminal devices. They also found that a polarisation inversion could be observed for both forward and reverse bias but more importantly that this reversal was non-reproducible. The two devices used in this study reported very different inversion characteristics, seen clearly in figure 3.7, but were formed using the same techniques from the same epilayer.

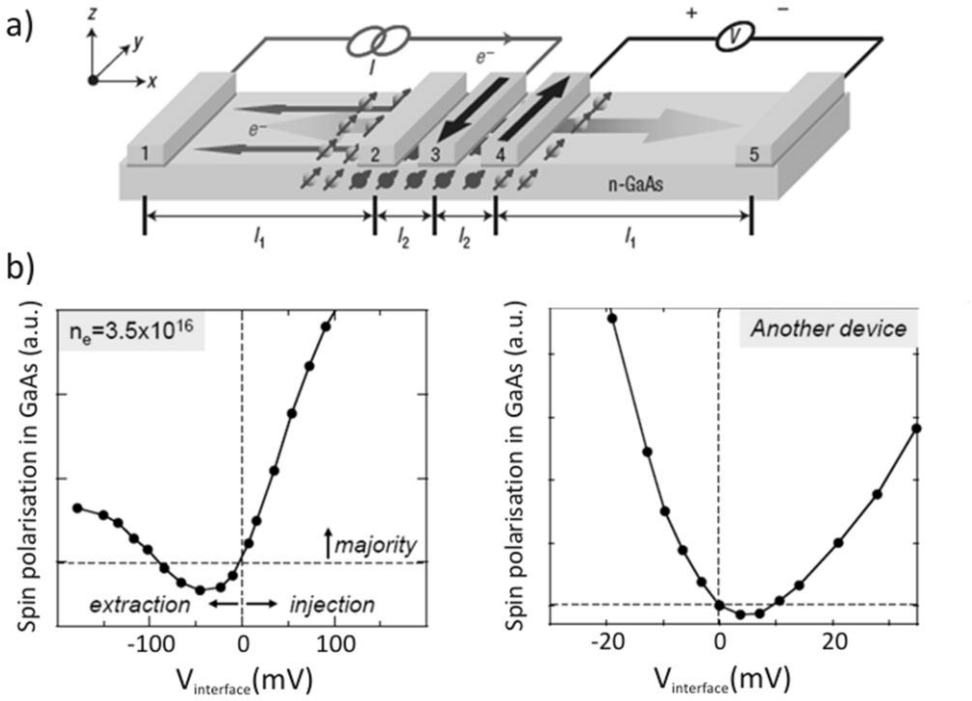

Figure 3.7 a) Schematic of the 5-terminal device and b) bias dependence of the spin polarisation for two devices reported by Lou *et al.* [44].

It is clear that an understanding of the inversion mechanisms are required if these systems are to be used in future device applications. There have been various proposals to explain the phenomenon of bias dependent polarisation inversion but no consensus has been reached.

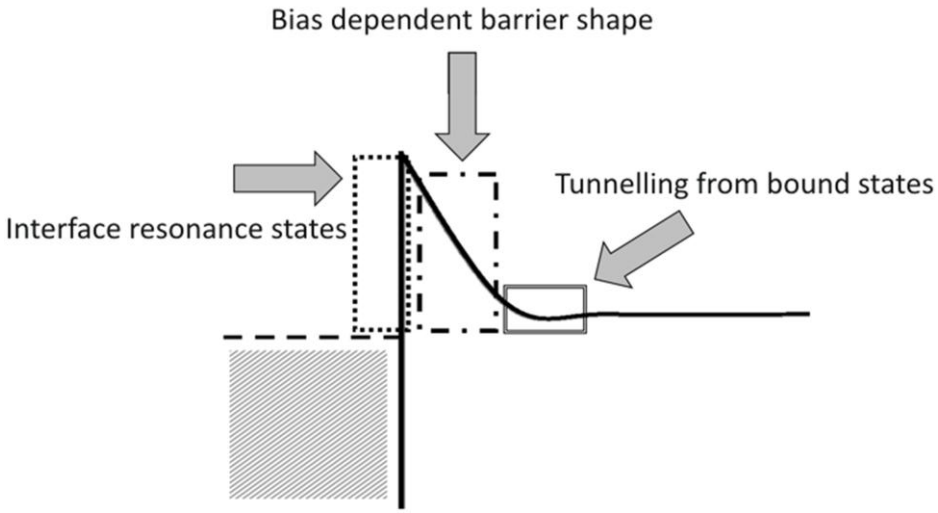

Figure 3.8 Schematic showing the three most promising candidates to explain the observation of a bias dependent polarisation inversion.

The three main proposals to explain the change in the sign of the polarisation are minority carrier interface resonance states, arising from the electronic structure; voltage dependent spin scattering, arising from the bias dependent barrier shape; and tunnelling from semiconductor bound states, arising from the doping profile.

3.3.1 Interface resonance states

The electronic structure at the metal/SC interface can play a key role in transport across the Schottky barrier, particularly on spin dependent transport. The first study of the electronic structure of the Fe/GaAs(001) interface was performed by Demchenko *et al.* [79] with further work performed by Chantis *et al.* [80] and Honda *et al.* [81]. Each of these studies showed that the electronic structure at the Fe/GaAs interface can lead to interface resonance states (IRS) for minority carriers, explaining the origin of polarisation inversion. The key difference between the calculations performed by

Chantis *et al.* [80] and Honda *et al.* [81] is the location of the interface states. Chantis *et al.* [80] used the formation of interface states on the Fe side of the junction to explain the polarisation inversion observed in previous reports. Honda *et al.*, however, used the formation of interface states on the GaAs side of the junction to explain the observed polarisation inversions. As the calculations performed by Honda *et al.* are the only ones capable of explaining the reversals for both forward and reverse bias this method appears to be the most likely candidate to explain the experimental results.

In the report by Honda *et al.* [81] a Green's function method was used to calculate the current by integrating over the energy gap of the Γ-point (the centre of the Brillouin zone)

$$I_{\uparrow(\downarrow)} = \int_{qV}^{0} G_{\uparrow(\downarrow)}(E)dE \qquad \text{for } V > 0 \qquad (3.16a)$$

$$I_{\uparrow(\downarrow)} = \int_{E_c+qV}^{0} G_{\uparrow(\downarrow)}(E)dE \qquad \text{for } V < 0 \qquad (3.16b)$$

where $G_{\uparrow(\downarrow)}(E) = \frac{1}{N_{||}}\sum_{K_{||}} G_{\uparrow(\downarrow)}\left(E, k_{||}\right)$ is the conductance at the Γ-point, $N_{||}$ is the number of atoms on an atomic plane and $k_{||}$ (=k_x, k_y) is the parallel wave vector. For an As-terminated surface a strong intensity in the minority carrier density of states was found near the Γ-point at 0.3eV and 0.7eV below the conduction band. Although these interface states are able to explain the observed bias dependence of the polarisation, they should also give rise to peaks in the current-voltage characteristics. These peaks are yet to be observed.

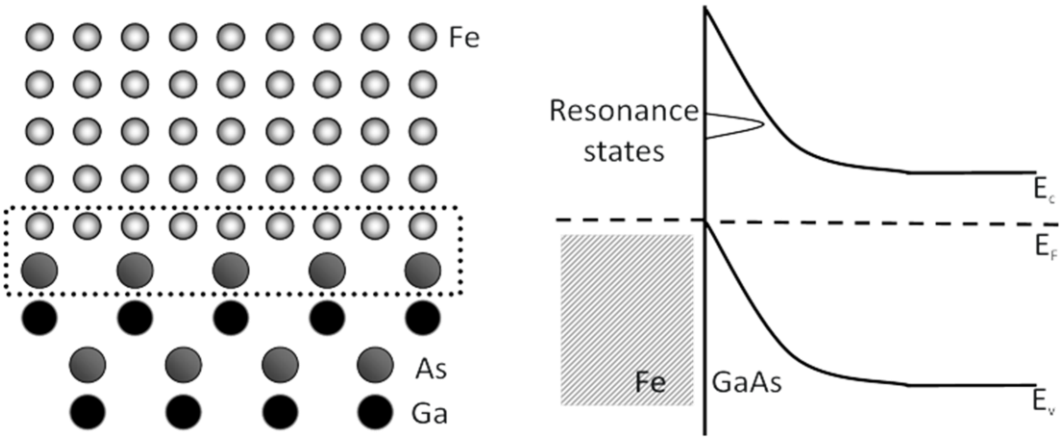

Figure 3.9 Schematic showing the location of interface states in Schottky barriers [81].

In all the calculations performed on the resonance states of Fe/GaAs(001) films the structure is modelled as a perfectly abrupt interface with the Fe lattice constant adjusted to match the GaAs lattice perfectly. As the resonance states are extremely sensitive to the atomic interface structure, a detailed knowledge of the atomic structure of Fe/GaAs(001) films is crucial to further understand the role of interface states and the subsequent effect on the transport properties in these systems.

3.3.2 Barrier shape bias dependence

Something that is often overlooked when considering the transport across a Schottky barrier is what happens to the electrons as they travel through the depletion regions. The effect of the bias voltage on the shape of the potential barrier was first discussed by Smith and Ruden [82]. In their model they calculated the spin dependent transmission coefficient through the depletion region by

$$T_{\uparrow} - T_{\downarrow} \simeq 4k_{z,s}^{0} \frac{(\chi_{\uparrow}-\chi_{\downarrow})|(\ln\psi_{SC})^2-\chi_{\uparrow}\chi_{\downarrow}|}{\phi_1^2[\chi_{\uparrow}^2\chi_{\downarrow}^2+(\chi_{\uparrow}^2-\chi_{\downarrow}^2)(\ln\psi_{SC})^2+(\ln\psi_{SC})^4]} \tag{3.17}$$

where k is the wave vector, $\chi_{\uparrow(\downarrow)}$ a spin dependent scattering coefficient and ψ_{SC} the wavefunction in the semiconductor.

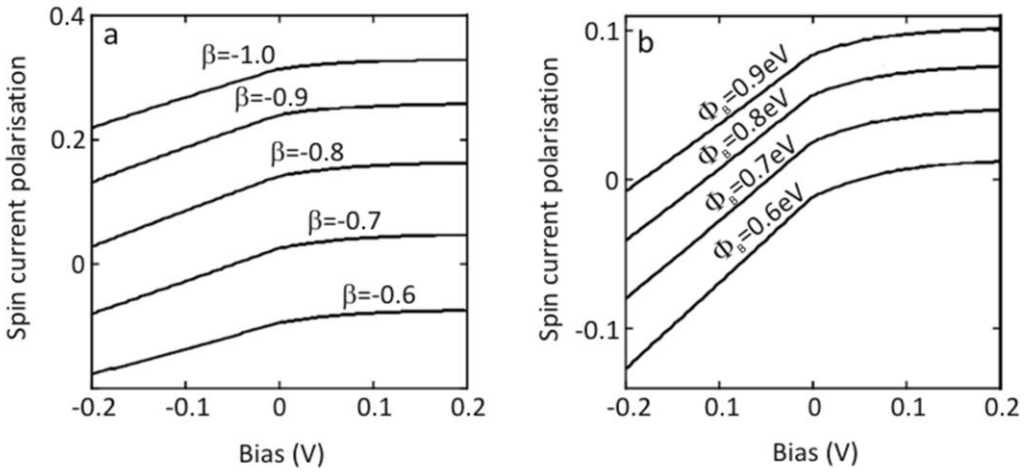

Figure 3.10 The current spin polarisation as a function of applied bias for (a) different coupling parameters β (for Φ_B=0.7 eV) and (b) different barrier heights Φ_B (for β=0.7eV) [82].

The bias dependence in their model arises from the assumption that the potential barrier in the semiconductor is parabolic. The scattering coefficient was assumed to be of the form $\chi = k\left(m^* / m_m^*\right)^{-\beta}$ [83], where m^* is the effective mass in the semiconductor, m^*_m is the effective mass in the metal near the Fermi energy and β is a coupling parameter which plays a vital role in the spin polarisation. The key results from this model are shown in figure 3.10, which shows the effect of the different coupling parameters and different barrier heights on the spin current polarisation. It can be seen that through varying both β and Φ_B a polarisation inversion can be achieved. As discussed in section 3.2 determining the barrier height experimentally is a very challenging task. It is also worth noting that this model has a large number of user-defined parameters, with no techniques currently available to determine β experimentally.

3.3.3 Semiconductor bound states

The first observation of a polarisation inversion in Fe/GaAs(001) devices was made when the junction was reverse biased, leading to spin extraction [43]. Spin extraction through Fe/GaAs(001) contacts was first examined theoretically by Dery and Sham [84]. The main focus of their study was to explore the origin and effect of tunnelling from bound states that can occur in the highly doped region near the interface shown in figure 3.11. Figure 3.11b was taken from [43, 84], with the calculations performed for a 25nm with doping region with a doping density increasing from $4x10^{17}cm^{-3}$ to $5x10^{18}cm^{-3}$. If the semiconductor has a sufficiently high carrier concentration and a width above > 15nm then bound states can form in the conduction band edge which acts like a quantum well. The spin dependent current density due to the escape of localised electrons from bound states in a two-dimensional electron gas is described by

$$J_{2D,\updownarrow} = q\sum_j \frac{n_j}{2\tau^{\mathrm{esc}}_{j,\uparrow(\downarrow)}} \tag{3.18}$$

Where n_j is the areal density of electrons in the *j*th state whose energy is higher than the Fermi energy of the ferromagnet, q the charge and $\tau^{\mathrm{esc}}_{j,\uparrow(\downarrow)}$ is the spin dependent

escape rate. The escape rate calculated for minority states in Fe was calculated to be nearly twice that for majority states. If a reveres bias is applied, reducing the number of free electrons, then the current due to localised electrons, found in the bound states, can dominate. This can lead to a polarisation reversal.

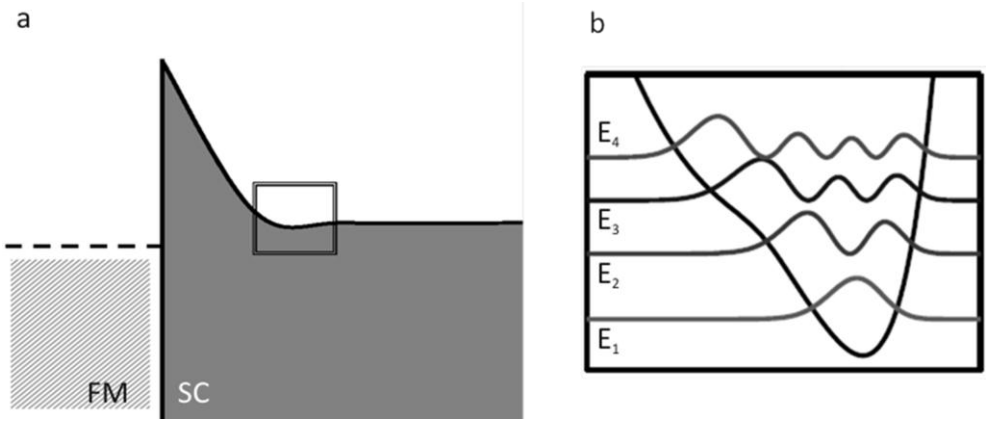

Figure 3.11 Figure showing the (a) conduction band potential in the semiconductor and (b) the bound states at the bottom of the band whose energies are below the semiconductor chemical potential (zero level) [84].

One advantage of this mechanism, if proved to contribute significantly to the transport, is that the doping profile is easily modified experimentally. This opens up the possibility of tuning the doping profile to obtain different device characteristics. It also means that the contribution to the transport for bound states can also be significantly reduced, allowing for the examination of the conductance from the other mechanisms, particularly interface resonance states.

3.4 Spin injection across the Fe/GaAs(001) Schottky barrier

In this chapter the different transport mechanisms across Fe/GaAs(001) Schottky barriers were introduced. In the samples presented in this study the thin barrier used should ensure that tunnelling, thermionic field and field emission, are the dominant transport mechanisms, particularly at low temperatures. Recent experimental work, however, has shown that there are other mechanisms that contribute to and possibly dominate the transport across the Fe/GaAs(001) interface. From the three additional mechanisms discussed interface resonance states (IRS) are expected to have the most

significant effect, discussed further in chapter 6. Tunnelling from semiconductor bound states is not expected to be significant in the samples studied due to the careful choice of the semiconductor doping profile. As was mentioned in section 3.3.2 it is not experimentally possible to determine the decay rates of the spins as they tunnel through the barrier so this mechanism is not discussed again in this study.

There is still some debate as to which side of the junction the interface resonance states form. The GaAs side appears the most promising as it is capable of explaining the polarisation inversions observed for both forward and reverse bias, discussed in section 3.3.1. Honda *et al.* [81] predict IRS for minority carriers that lie 0.3 and 0.7eV below the bottom of the conduction band. These states, however, have not yet been observed. This is most likely due to the fact that the location of the IRS is extremely sensitive to the atomic interface structure. As there is yet to be an experimental report on the interatomic spacings of the Fe/GaAs(001) interface, current calculations can only estimate the location and strength of potential IRS.

Chapter 4. Spin Transport and Relaxation

Once spin-polarised electrons are injected across the FM/SC interface the spin populations will be driven out of equilibrium. Understanding the spin transport and relaxation mechanisms is crucial if devices are to fabricated with the long lifetimes and spin diffusion lengths required. Manipulating the spins inside a semiconducting channel could be achieved by utilising the Rashba spin-orbit interaction.

4.1 Spin Transport

4.1.1 Spin diffusion

A spin-polarised current is essential for spintronic devices. As this will not involve charge transfer the transport is diffusive. Conventional spin-polarised currents are described by the spin dependent form of Ohm's law, discussed in chapter 2

$$j_{\uparrow(\downarrow)} = \sigma_{\uparrow(\downarrow)} \frac{\nabla \mu_{\uparrow(\downarrow)}}{e} \tag{2.11}$$

where e is the electron charge, $\sigma_{\uparrow(\downarrow)}$ are the spin dependent conductivities and $\Delta\mu_{\uparrow(\downarrow)}$ is the difference in the electrochemical potentials for the two spin channels. The conductivities are related to the density of states at the Fermi level and the diffusion constants through the Einstein relation [85]

$$\sigma_{\uparrow(\downarrow)} = N(E_F)_{\uparrow(\downarrow)} e^2 D_{\uparrow(\downarrow)} \tag{4.1}$$

This relationship describes the behaviour of the two spin channels but does not take into account spin-flip processes. These are described by the continuity equations

$$\frac{1}{e}\nabla j_{\uparrow} = -\frac{n_{\uparrow}}{\tau_{\uparrow(\downarrow)}} + \frac{n_{\downarrow}}{\tau_{\downarrow(\uparrow)}} \tag{4.2a}$$

$$-\frac{1}{e}\nabla j_{\downarrow} = -\frac{n_{\uparrow}}{\tau_{\uparrow(\downarrow)}} + \frac{n_{\downarrow}}{\tau_{\downarrow(\uparrow)}} \tag{4.2b}$$

where $n_{\uparrow(\downarrow)}$ are the particle densities and $\tau_{\uparrow(\downarrow)}/\tau_{\downarrow(\uparrow)}$ are the spin flip rates, related by

$$\frac{N_{\uparrow}(E_F)}{\tau_{\uparrow(\downarrow)}} = \frac{N_{\downarrow}(E_F)}{\tau_{\downarrow(\uparrow)}} \tag{4.3}$$

Equation (4.3) can be used to re-write the continuity equations (4.2) to give

$$\frac{1}{e}\nabla j_{\uparrow} = -\frac{1}{e}\nabla j_{\downarrow} = \frac{\mu_{\uparrow}-\mu_{\downarrow}}{N(E_F)\tau_{sf}} \tag{4.4}$$

where $N(E_F)$ is the total DOS at the Fermi level = $N_{\uparrow}(E_F) + N_{\downarrow}(E_F)$ and τ_{sf} is the spin flip time defined as [86]

$$\frac{1}{\tau_{\mathrm{sf}}} = \frac{1}{\tau_{\uparrow(\downarrow)}} + \frac{1}{\tau_{\downarrow(\uparrow)}} \tag{4.5}$$

Equation (4.4) shows that the driving force for spin flip processes is the difference in the electrochemical potentials. Equation (2.9) can be substituted into equation (4.4) to give the relationship

$$\frac{\partial \mu_{\uparrow}-\mu_{\downarrow}}{dx^2} = \frac{\mu_{\uparrow}-\mu_{\downarrow}}{D\tau_{sf}} \tag{4.6}$$

where D is the spin diffusion constant given by [87]

$$\frac{1}{N(E_F)D} = \frac{1}{N_{\uparrow}(E_F)D_{\uparrow}} + \frac{1}{N_{\downarrow}(E_F)D_{\downarrow}} \tag{4.7}$$

The spin diffusion constant and spin flip time are often grouped together to define the spin flip length λ_{sf} given by

$$\lambda_{\mathrm{sf}} = (D\tau_{\mathrm{sf}})^{1/2} \tag{4.8}$$

Equation (4.6) is the fundamental equation used to describe diffusive spin transport providing the spin lifetime is longer than the momentum scattering time [88]. As the spin lifetime in GaAs is often several nanoseconds [89], orders of magnitude greater than the momentum scattering time, equation (4.6) provides a suitable description for the spin transport.

4.1.2 Electron drift

If a voltage is applied across a FM/SC junction the subsequent electric field causes charge carriers in the semiconductor to be accelerated along the direction of force. Using Boltzmann's theory the electron states can be defined by a distribution function *f(k)* [90]. An electric field would cause a change in the distribution function, driving it away from equilibrium. If the distribution function is shifted along a quantity *k'* then to a first approximation the distribution becomes

$$f(\boldsymbol{k}) = f_{FD}(\boldsymbol{k} - \boldsymbol{k}') \approx f_{FD}(\boldsymbol{k}) - \nabla_{\mathrm{k}} f_{FD}(\boldsymbol{k}) \cdot \boldsymbol{k}' \tag{4.9}$$

where $f_{FD}(k)$ is the equilibrium Fermi distribution. When the applied field is sufficiently weak so that only effects that are linear to the applied field are considered it is known as the linear response regime. Using this assumption equation (4.9) can be written as

$$f(\boldsymbol{k}) \approx f_{FD}(\boldsymbol{k}) + f_1(\boldsymbol{k}) \tag{4.10}$$

where $f_1(k)$ is the linear response in the distribution due to the electric field.

In the steady state changes in the distribution due to collisions, drift (transport) and the electric field will all cancel. This is described by the equation

$$\frac{\partial f(\boldsymbol{k})}{\partial t}\Big|_{Drift} + \frac{\partial f(\boldsymbol{k})}{\partial t}\Big|_{coll.} + \frac{\partial f(\boldsymbol{k})}{\partial t}\Big|_{field} = 0 \tag{4.11}$$

This equation can be simplified further if it is assumed that the change in the distribution function due to collisions is of the form

$$\frac{\partial f(\boldsymbol{k})}{\partial t}\Big|_{coll.} = -\frac{f_1(\boldsymbol{k})}{\tau_p(\varepsilon)} \tag{4.12}$$

where $\tau_p(\varepsilon)$ is the momentum relaxation time. This assumption is known as the relaxation time approximation as equation (4.12) means that the function f_1 will exponentially decay to zero if the electric field is removed.

$$\frac{\partial f_1(\boldsymbol{k})}{\partial t} = -\frac{f_1(\boldsymbol{k})}{\tau_p(\epsilon)} \tag{4.13}$$

$$f_1(\boldsymbol{k}, 0) = f_1(\boldsymbol{k}, 0) e^{-t/\tau} \tag{4.14}$$

So in the linear response regime τ relaxes only the momentum (or velocity), with the energy distribution remaining the same as that for the equilibrium function. Using all of the above assumptions, the non-equilibrium part of the distribution function can be described by [90]

$$f_1(\boldsymbol{k}) = -\tau e\boldsymbol{E} \cdot \boldsymbol{v_k} \frac{\partial f_{ED}(\boldsymbol{k})}{\partial \varepsilon_s} \tag{4.15}$$

where $\boldsymbol{E}$ is the electric field, $\boldsymbol{v_k}$ the group velocity and ε_s the dielectric constant.

For an isotropic system the effect of applying an electric field causes a small shift in the distribution function with a *drift velocity* relative to the Fermi Dirac distribution, shown in figure 4.1, given by

$$v_D = \boldsymbol{E} \frac{e\tau_p}{m^*\hbar} \tag{4.16}$$

where m^* is the electron effective mass. The electron mobility μ_e can then be defined as the relationship between the *drift velocity* and the electric field

$$\mu_e = \frac{V_D}{\boldsymbol{E}} \tag{4.17}$$

The shift in the distribution function can be shown as a shift in the Fermi sphere or an unequal occupation of the sub-bands of the $\pm k_x$ direction, both shown in figure 4.1.

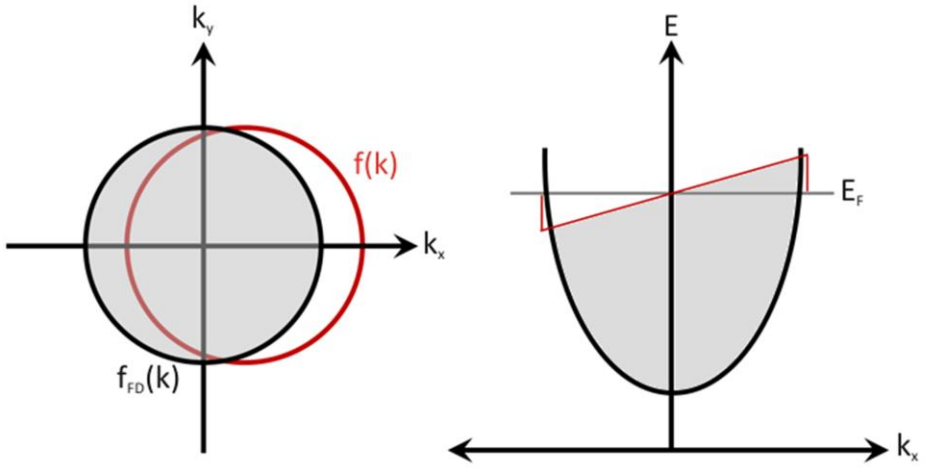

Figure 4.1 Effect of applying an electric field across a semiconductor showing the shift in the Fermi surface or unequal occupation of the sub-bands of the ±kx direction [90].

4.2 Spin-orbit interaction

The spin-orbit interaction arises from the relativistic treatment of an electron moving in an electric field, such as that arising from an atomic nucleus. If the system is treated from the rest frame of the electron then the electric field also has a magnetic component, which can be described by the standard Lorentz transformation [91]

$$\boldsymbol{B}_{eff}(x) = \frac{\boldsymbol{v}\times\boldsymbol{E}(x)}{c} \tag{4.18}$$

where ***v*** is the velocity, ***E*** the electric field and *c* the speed of light. As the system now effectively contains two spins, this affects the spin dynamics of the electron and also the total energy of the system. The spin-orbit interaction can be described by the Hamiltonian

$$H_{so} = -\frac{\hbar}{4(m^*c)^2}(\boldsymbol{\sigma_i}\cdot[\boldsymbol{E}\times\boldsymbol{p}]) \tag{4.19}$$

where m^* is the effective mass, $\boldsymbol{\sigma}_i$ the Pauli matrices, ***E*** and electric field and ***p*** the momentum vector [26]. The term in the square brackets can be replaced with an effective magnetic field $\mathbf{B}_{eff} = \boldsymbol{E} \times \boldsymbol{p}$. The electron spin can therefore be affected not only by externally applied magnetic fields but also by effective internal fields, arising from the crystal structure and from externally applied electric fields.

There are several origins of effective magnetic fields that are intrinsic in III-V semiconductors arising from: the radial distribution of atomic potentials; the bulk inversion asymmetry in the lattice; and structural inversion asymmetry. The first is the usual *ls* coupling that acts on the *p*, *d* and *f* orbitals. The second is known as Dresselhaus-type coupling that is due to the asymmetric crystal field that acts on mobile electrons [92]. The third is known as Rashba-type coupling that occurs in quantum wells and heterostructures [93]. In two-dimensional electron gas (2DEG) systems this provides a very useful method to control/manipulate spins without the need to apply an external magnetic field. If a voltage is applied across a 2DEG, the strength of the spin-orbit interaction changes through the Rashba coupling. The Rashba effect is described by the Hamiltonian

$$H_R = \frac{2\hbar}{m^*}k\left[S_x k_y - S_y k_x\right] \tag{4.20}$$

where k is the wave vector, m* the effective mass, $S_{x(y)}$ the $x(y)$ spin components and $K_{x(y)}$ the $x(y)$ components of the wave vector.

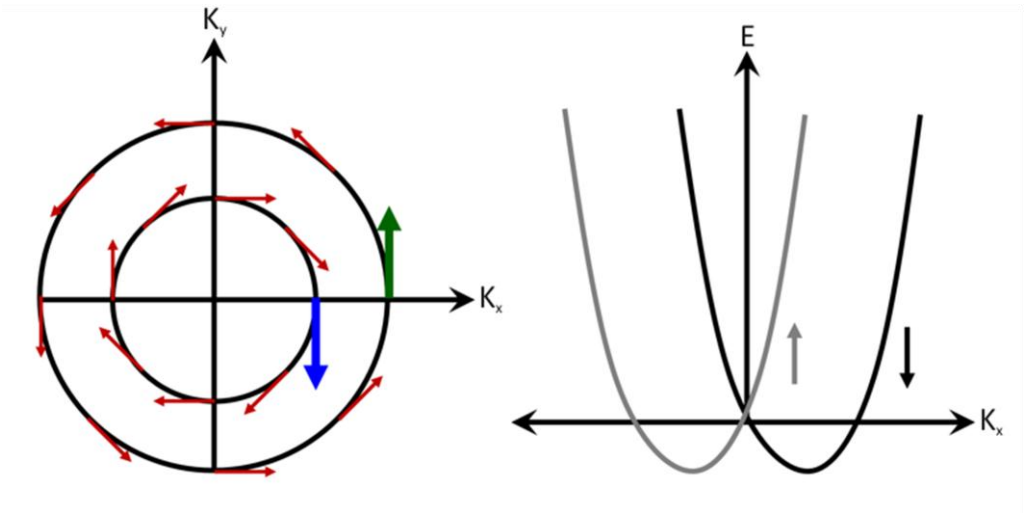

Figure 4.2 Schematic showing the Rashba effect on the Fermi surface and on the spin sub-bands [93].

The Rashba effect causes a momentum dependent spin splitting to occur, shown in figure 4.2. It can be seen from the figure that the Rashba effect causes a horizontal shift in the Fermi surface unlike the Zeeman effect which causes a vertical shift. It is hoped that this mechanism could be utilised in many spintronic devices, such as a spin-FET, to eliminate the need for external magnetic fields.

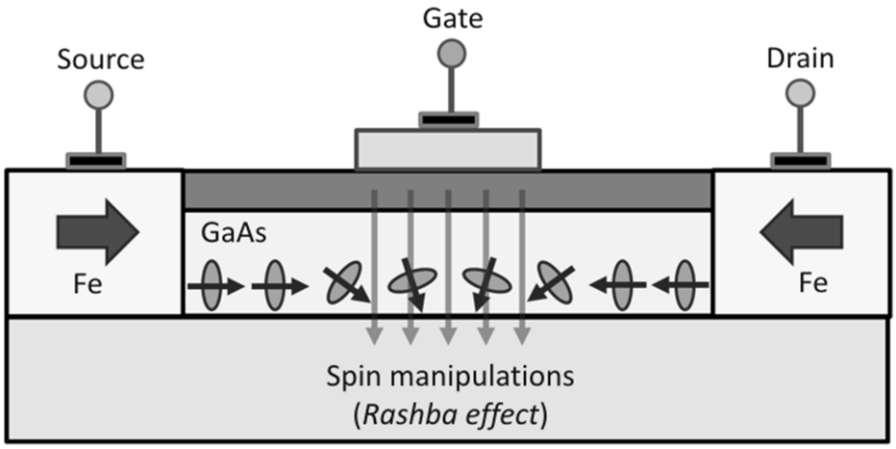

Figure 4.3 Schematic of a spin-FET which uses the Rashba effect to manipulate the spins [19].

Figure 4.3 shows a schematic of a spin-FET [19], with the channel conductance change due to spin dependent scattering at the drain. In order for this type of device to be realised, a reliable method for manipulating the spins is required. This is easily achieved through the Rashba effect by applying a gate voltage.

4.3 Spin relaxation

If a non-equilibrium spin population is created inside a conventional semiconductor such as GaAs the spins will relax to the equilibrium state through processes discussed in section 4.3.2. The spin relaxation can generally be understood as a result of the spins interacting with randomly fluctuating magnetic fields [94]. These fields don't have to be *real* magnetic fields but are usually *effective* magnetic fields which originate from the spin-orbit or exchange interactions. As the spins interact with these effective magnetic fields they will start to precess around the random field direction with a frequency Ω. If this field is assumed to be constant for a time τ_C, known as the correlation time, then after τ_C the direction of the field randomly changes. The spins will therefore start to precess around a new field direction. After numerous steps the initial spin direction will be lost and the spins will have relaxed. A randomly fluctuating magnetic field can therefore be characterised by two parameters; the root mean square (rms) value of the spin precession frequency Ω and the correlation time τ_C. There are two limiting cases that can be considered:

When $\Omega\tau_C \ll 1$ the spins will experience a slow angular diffusion as the precession angle is small. This type of relaxation is the most common that occurs in conventional semiconductors, giving rise to a relaxation time $\tau_S \gg \tau_C$

$$\frac{1}{\tau_S} \sim \Omega^2 \tau_C \tag{4.21}$$

When $\Omega\tau_C \gg 1$ the spins will rotate multiple times around the magnetic field during the correlation time. In this type of relaxation the transverse component of the spin is destroyed on the order of $1/\Omega$ whilst the component directed along the direction of the field decays on a time scale on the order of $\tau_S \sim \tau_C$.

4.3.1 Spin relaxation T_1 and dephasing T_2 times

If an external magnetic field $\boldsymbol{B}$ is applied it will cause a precession of the spins around the field direction with a frequency Ω given by the Larmor equation

$$\Omega = \frac{g\mu_B \boldsymbol{B}}{\hbar} \tag{4.22}$$

where g is the electron g-factor and μ_B the Bohr magneton. It is conventional to distinguish between the relaxation of the spin component along the $\boldsymbol{B}$ direction and the perpendicular components: the *spin relaxation time* T_1, often referred to as the longitudinal or spin-lattice time, and *the spin dephasing time* T_2, often referred to as the transverse or decoherence time. In T_1 processes, energy is transferred from the spin system into the lattice, usually through phonons. T_2 processes cause a loss of phase for an ensemble of spins but in some situations the phase can be recovered. This has lead to two different spin dephasing times denoted by T_2 which represents the irreversible loss of phase and T_2* which is the time for reversible phase losses. The T_2* component can be recovered using spin echo experiments [95]. It should be noted that $T_2^* \sim T_2$ is a very good approximation, particularly when dealing with conduction electrons [96].

It has been found experimentally that $T_1 \sim T_2$ in many systems, first observed in nuclear magnetic resonance experiments by Bloch *et al.* [97] and in electrons spin systems by Pines and Slitcher in 1955 [98]. This is often the case when dealing with isotropic cubic solids but even when dealing with anisotropic systems $2T_2 \leq T_1$. This is very convenient as T_1 is often calculated theoretically but T_2 is determined experimentally. A single symbol τ_s is often used to represent both the spin relaxation and dephasing times.

4.3.2 Spin relaxation mechanisms

The Elliot-Yafet mechanism [99, 100] is a spin relaxation mechanism that arises from phonons and impurities. In Elliot-Yafet scattering the interaction of the electrons with phonons or impurities induces spin-orbit coupling, subsequently causing an effective magnetic field. Hence in Elliot-Yafet scattering, momentum relaxation leads to spin relaxation. When scattering from impurities, the direction of the random magnetic field depends on the geometry of the individual collision sites, with each collision causing the scattered spin to rotate by a small angle. The relaxation rate is

therefore inversely proportional to the impurity concentration $\tau_s^{-1} \alpha n^{-1}$. So although increasing the doping density increases the conductance of the channel, the spin lifetime is subsequently reduced.

The D'yakonov-Perel mechanism [101] is responsible for spin dephasing in crystals that do not have inversion symmetry, such as III-V semiconductors. This mechanism is expect to be the dominant relaxation mechanism in the metallic phase of GaAs for doping densities n_d>2x10^{16}cm^{-3}.The inversion asymmetry gives rise to a momentum dependent magnetic field which leads to momentum dependent spin precession. This is best described by introducing a ***k*** dependent magnetic field into the conventional Larmor frequency equation

$$\boldsymbol{\Omega}(\boldsymbol{k}) = \frac{e}{m}\boldsymbol{B}(\boldsymbol{k}) \tag{4.24}$$

There are two limiting cases for the D'yakonov-Perel mechanisms which can be described by the average magnitude of the intrinsic Larmor frequency Ω_{av} and its relationship to the momentum relaxation time τ_p. The two cases are when $\Omega_{av}\tau_p >>1$, so individual electron spins precess a full cycle before being scattered to another momentum state. For the second case, when $\Omega_{av}\tau_p <1$, the electrons precess around fluctuating magnetic fields. This means that the phase of the individual spins, after many steps, is the sum of the randomly selected frequencies.

For the first case ($\Omega_{av}\tau_p >1$) the electron spins form an ensemble that samples the distribution of $\boldsymbol{\Omega}_{\mathbf{k}}$. The spin dephasing rate is therefore proportional to the width of the distribution of Larmor frequencies $1/\tau_s > \Delta\Omega$.

The second case is usually what is meant when referring to the D'yakonov-Perel mechanism ($\Omega_{av}\tau_p <1$). In this situation after the electron spin interacts with an intrinsic field it rotates and angle $\delta\theta = \Omega_{av}\tau_p$. It then experiences another field and rotates in a different direction. As a result the phase of the spins follows a random walk, with the phase described by $1/\tau_s = \delta\theta\sqrt{t/\tau_p}$. If τ_s is defined as the time where θ(t)=1 then the spin dephasing time is given by $1/\tau_s = \Omega^2_{av}\tau_p$. This means that the faster the momentum relaxation occurs, the slower the spin dephasing. The relaxation rate therefore increases as the impurity concentration decreases $\tau_s^{-1} \alpha n$.

In systems with inversion asymmetry, such as GaAs, both the Elliot-Yafet and D'yakonov-Perel scattering mechanisms occur. As well as these mechanisms there is also an anisotropic exchange interaction of donor-bound electrons. The spins of two localised electrons are coupled through both magnetodipole and exchange interactions. Although the isotropic exchange interactions do not lead to spin relaxation, the inversion asymmetry in III-V semiconductors leads to an anisotropic exchange interaction. The anisotropic exchange gives rise to random effective fields which causes spin relaxation. This was first studied in the context of GaAs by Kavokin [102]. In this report it was shown that this type of relaxation mechanism should dominate for doping densities around n_d=2x10^{16} cm^{-3}, the metal-insulator transition point for GaAs. This was shown to be the case experimentally by Dzhioev *et al.* who explored the effect of the doping density on the relaxation mechanism in GaAs [89].

4.3.3 Electron and Nuclear spin interactions

One of the problems when trying to determine the electron spin relaxation times in semiconductors is that they interact with the nuclear spin through hyperfine interactions. The polarised electrons can undergo *'flip-flop'* interactions with the nuclei, exchanging their spin directions [103]. If the electron spin polarisation is continually injected the nuclear spins can become polarised through this mechanism, known as dynamic nuclear polarisation (DNP) [104]. These interactions are on the order of picoseconds [105]. Once the nuclear spin is polarised it can lead to large effective fields which can have a significant effect on the electron spins.

DNP has been observed in GaAs with current-induced DNP shown to be much greater than optically induced DNP [106]. These effects are expected to be significant for doping concentrations below 2x10^{16} cm^{3} when operating at temperatures below 20K [107]. DNP has also been shown to play a key role in Fe/GaAs(001) systems at low temperature [108, 109] which needs to be taken into account when analysing the electron transport measurements, discussed further in chapter 7.

4.4 Spin transport and relaxation in GaAs

Pure spin currents are required for spintronic devices. When injecting spins into GaAs the spins will diffuse with a characteristic length λ_{sf} given by equation 4.8. The spin diffusion length and spin lifetimes in GaAs vary depending upon the doping density as varying the doping density has a significant effect on the spin relaxation times [89]. For densities up to around n_d=5x10^{15} cm^{-3} the relaxation is dominated by hyperfine interactions. For densities up to the metal-insulator transition point of n_d=2x10^{16} cm^{-3} the relaxation is dominated by anisotropic exchange interactions. For the metallic phase with n_d=2x10^{16} cm^{-3} the relaxation is dominated by D'yakonov-Perel scattering. Typical spin diffusion times for GaAs with doping densities around n_d=2x10^{16} cm^{-3} are on the order 100ns [43, 44, 110, 111]. These long spin lifetimes are the reasons why GaAs has generated such interest with many potential device applications.

Chapter 5. Experimental Techniques

Correlating the atomic interface structure with the transport properties is crucial for the development of future semiconductor spintronics devices. However, this requires the use of many experimental techniques. As well as thin film growth, device fabrication, magnetic and interface characterisation, both electrical and optical methods are needed to explore device characteristics.

5.1 Sample fabrication

5.1.1 MBE growth

Molecular beam epitaxy (MBE) is one of the most important growth techniques in the semiconductor industry and is at the forefront of developing novel devices. The main advantage of MBE growth compared to other techniques is that it allows for excellent compositional control with monolayer resolution in the z-direction (film thickness). One of the greatest problems with MBE growth is that it can lead to a distribution of magnetic properties in the x-y plane of thin films. As discussed in section 2.1.2 the magnetic properties of thin films are dominated by defects. In MBE grown films the defects arise from dislocations or point defects such as vacancies or interstitial defects which occur in a non-reproducible manner. Great care must therefore be taken when designing devices which do not depend on the

reproducibility of the magnetic properties in the x-y plane. The results in this study are concerned with the atomic interface structure and the transport properties, obtained after saturating the Fe layer along the (110) direction. So although the microscopic magnetic properties could have a significant effect on future device operation, they do not play a major role when correlating the macroscopic interface structure to the transport across the Schottky barrier.

Molecular beams can be created using a Knudson cell (K-cell), electron gun (e-gun), effusion cell and through various other techniques [112]. For a molecular beam to form, the mean free path of the molecules needs to be larger than the distance between the source and the substrate. This is easily achieved under ultrahigh vacuum conditions. This does however, limit the growth rate as the gas evolution from the source needs to be as low as possible to maintain the ultrahigh vacuum. A guide to Vacuum physics and techniques can be found in A. Chambers [113]. The surface of the film can be characterised through analysis of the Low Energy Electron Diffraction (LEED) [114] or Reflection High-Energy Electron Diffraction (RHEED) [115] methods. These techniques make it possible to ascertain whether the film growth is epitaxial, polycrystalline or amorphous.

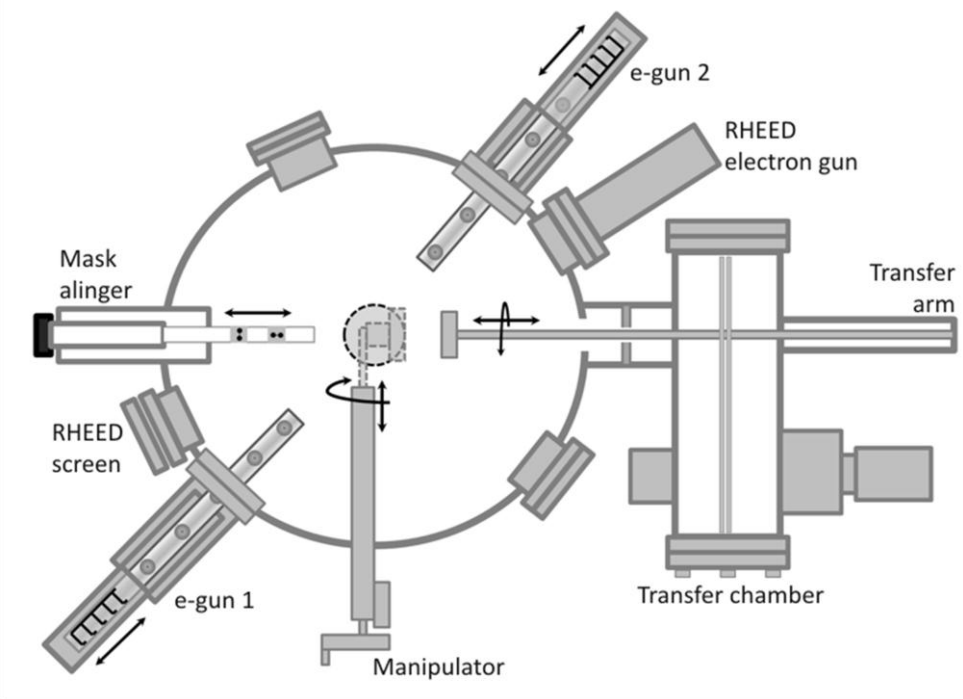

Figure 5.1 Schematic of the MBE system in York.

In the UK there are various centres or institutes with the capabilities to achieve MBE growth of metallic films but achieving high quality epitaxial growth of semiconductors is a much greater challenge. The EPSRC national centre for III-V technologies provides world class MBE growth to UK institutes [116]. The centre comprises of four partners: Sheffield who is the main contractor; Cambridge who prepares GaN structures; Glasgow who deals with nanoscale device fabrication; and Nottingham which prepares ferromagnetic semiconductors and ferromagnetic/semiconductor hybrid structures.

Molecular beam epitaxy was used to prepare the samples studied in this thesis. Epitaxial GaAs layers were grown at 540-580°C using a ultra-high vacuum (UHV) MBE, by Prof. Y. Ohno, H. Kobayashi and Y. kaneko at Tohoku University, onto commercial GaAs(001) wafers. Various buffer layers were used, such as an AlAs/GaAs supper lattice, to ensure a flat interface with minimal surface roughness. A moderately n^- doped GaAs layer with a free carrier density on the order of 5×10^{16} cm^{-3} was grown onto the buffer layers to create a 2000 nm thick conduction channel. A 12nm thin layer of highly n^+ doped GaAs, with a free carrier density on the order of 1×10^{19} cm^{-3}, was grown to help control the contact resistance, creating a narrow Schottky barrier. A thick As-capping layer was then deposited to protect the wafer whilst transferring to another chamber for the metal growth.

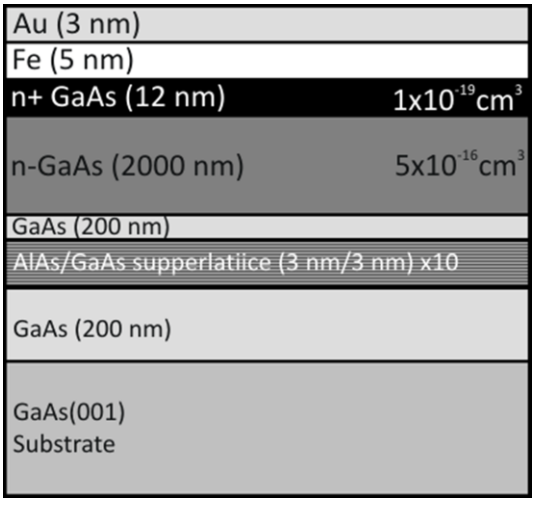

Figure 5.2 Typical structure of the samples used in this study.

The metal deposition was performed at either Cambridge University or the University of York, monitored using LEED or RHEED respectively. After being placed

into the MBE chamber the surface of the substrate was cleaned *in situ* by As desorption by heating the substrate up to a temperature of 750°C. After removal of the As cap, checked using LEED or RHEED, the temperature was held at 500°C to create an As-rich (1x1) surface reconstruction [117]. A thin Fe film, approximately 5nm thick, was then deposited at room temperature at a rate of ~0.1Å/s, monitored using a conventional quartz crystal. The film growth was monitored using RHEED. High quality epitaxial films were grown due to the excellent lattice match between Fe (2.867Å) and GaAs (5.654Å), with only ~1.4% mismatch. The films were then capped with a Au layer, typically between 3 and 10nm thick. The metal growth was always performed at room temperature in UHV with a base pressure better than 2×10^{-8} Pa.

5.1.2 Shape of the semiconductor conduction band

The semiconductor doping profile has a significant effect on the shape of the conduction band. If the band has pronounced bending this can lead to the formation of bound states, as discussed in section 3.3 [84]. Hu *et al.* showed that tunnelling from these bound states could have a significant effect on the spin injection efficiency in Fe/GaAs(001) systems [118]. Simulations were performed to explore the shape of the conduction band for the samples studied in this work. The calculations were performed by solving the Poisson and Schrödinger equations using a programme created by Snider from the University of Notre Dame [119]. The one-dimensional Poisson equation is

$$\frac{d}{dx}\left(\varepsilon_s(x)\frac{d}{dx}\right)V(x) = \frac{-q[N_D(x)-n(x)]}{\varepsilon_0} \qquad (5.1)$$

where ε_s is the dielectric constant, V the electrostatic potential, N_D the ionized donor concentration, n the electron density distribution and ε_0 the permittivity of free space. The energy of the conduction band edge E_c is given by

$$E_c(x) = -qV(x) + \Delta E_c(x) \qquad (5.2)$$

where ΔE_c is the pseudo-potential formed due to the band offset at the heterostructure interface. The one-dimensional Schrödinger equation is

$$-\frac{\hbar^2}{2}\frac{d}{dx}\left(\frac{1}{m^*(x)}\frac{d}{dx}\right)\psi(x) + U_E(x)\psi(x) = E\psi(x) \quad (5.3)$$

where $\psi(x)$ is the wavefunction, m^* the effective mass and U_E the potential energy. The wavefunction and the electron density are related by

$$n(x) = \sum_{k=1}^{m} \psi_k^*(x)\psi(x) \quad (5.4)$$

where m is the number of bound states and n_k is the electron occupation for each state. The electron concentration for each state is given by

$$n(x) = \frac{m^*}{\pi\hbar^2}\int_{E_k}^{\infty} \frac{dE}{1+\exp\left(\frac{E-E_F}{k_BT}\right)} \quad (5.5)$$

where E_k is the eigen-energy. The programme used to calculate the shape of the band structure solves the equations self-consistently [120]. The Schrödinger equation is first solved for a trial potential energy $U_E(x)$, with the corresponding energy eigenvalues E_k used to calculate the electron energy density distribution. This energy distribution and the donor concentrations are used to calculate the electrostatic potential V. The value of V is then used to calculate a new value for the potential energy and the process continued until the two values are close enough to satisfy the programme's error condition. A more detailed description of the iterative procedure can be found in report by Tan *et al.* [121].

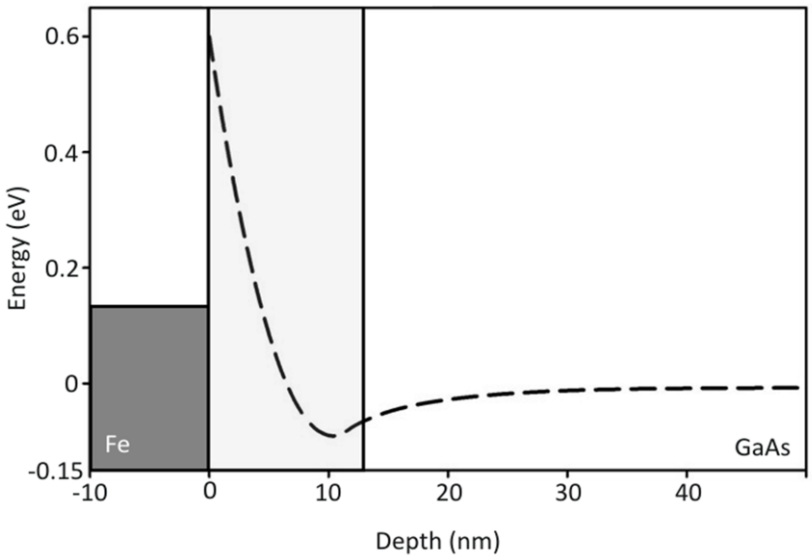

Figure 5.3 Example of a band structure calculation showing the shape of the conduction band for an Fe/GaAs(001) heterostructure with a 12nm thin n^+ GaAs layer with a doping density of $1x10^{19}cm^{-3}$ grown onto a n- layer with a doping density of $1x10^{16}cm^{-3}$ with a Schottky barrier height of 0.4eV.

Figure 5.3 shows an example band structure for an Fe/GaAs(001) heterostructures. The calculations were performed for a Schottky barrier height of 0.6eV for a sample with the sample structure shown in figure 5.2. When using the programme to model a heterostructures with a Schottky barrier, as used in this work, the Schottky barrier introduces an effective electrostatic potential. This, however, is small enough that it does not cause a significant current flow. The programme also assumes that all of the donors in the semiconductor are ionized and neglects electron-electron interactions.

5.1.3 Photolithography

Photolithography is widely used in the semiconductor industry [122]. Photolithography involves coating a sample in a polymeric resist using a spin-coater to achieve a uniform distribution of resist across the sample. A photomask, usually made of fumed silica, is then placed onto the substrate leaving some areas uncovered. A uniform exposure of radiation, typically ultra-violet (UV) radiation from a Mercury gas-discharge lamp, is used to affect the bonds in the polymer. There are two types of resist- positive and negative. If chemical development causes the removal of the exposed resist then it is known as a positive photoresist. If the exposed area is the area that will remain after development then this is a negative photoresist. After developing the resist a layer can be deposited or the exposed areas can be etched. Positive resists are conventionally used in conjunction with lift-off techniques where a film is deposited onto a sample, coating both the previous layer and resist. The sample is then placed into a stripping solution to remove the resist. The resist removal causes a lift-off the film above, thus leaving film only on the exposed regions. As well as depositing films onto the resists, the resists can also be used to protect regions of the sample whilst etching is performed. Etching can be performed through chemical methods, often used to etch semiconductor layers, or physical methods, often used to remove metallic films.

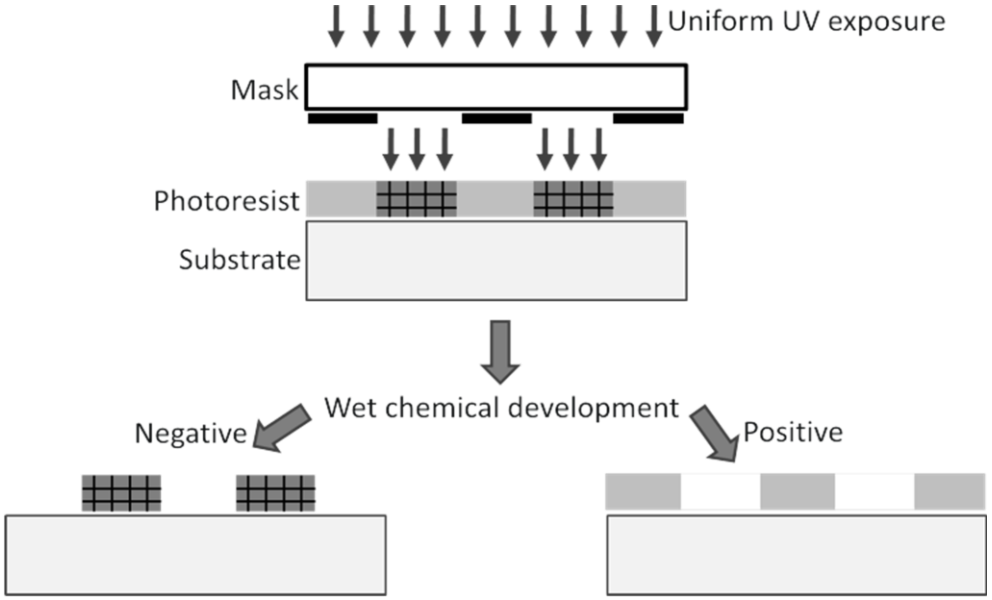

Figure 5.4 Schematic of negative and positive photoresist development [122].

These conventional photolithography techniques were used to fabricate the devices studied in this thesis. All of the Photolithography was performed at the Research Institute of Electrical Communication at Tohoku University. This work was supervised by Prof. Yuzo Ohno and with the experiments performed with the help of Mr Yuki Kaneko and Mr Hiroomi Kobayashi. The steps outlined here are those of the three-terminal Fe/GaAs device.

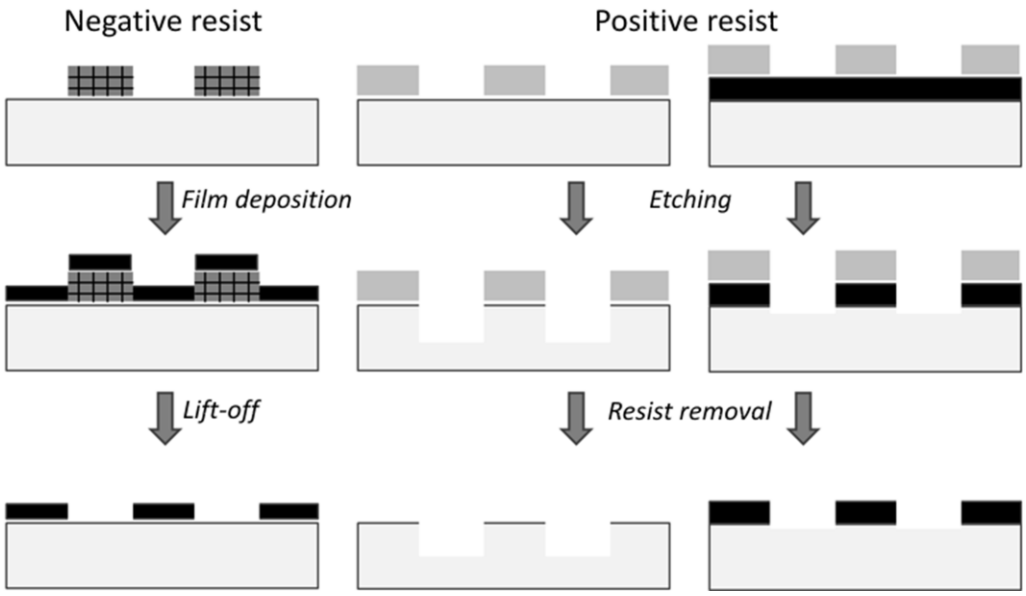

Figure 5.5 Schematic of selective area deposition and etching using photolithography [122].

The first step is to create the Fe contacts and alignment marks. This was achieved using Ar ion milling at a rate of approximately 1.25nm/s to a depth of 100nm. After creating the Fe contacts the GaAs mesa structure was created using wet etching. The sample was etched using a solution NH_4O_4:H_2O_2:H_2O = 20:4:400 with an approximate etching rate of 6nm/s to a depth of 2.75µm. Al_2O_3 insulating pads were then sputtered using conventional rf plasma sputtering at a rate of 0.2nm/s to a thickness of 200nm.

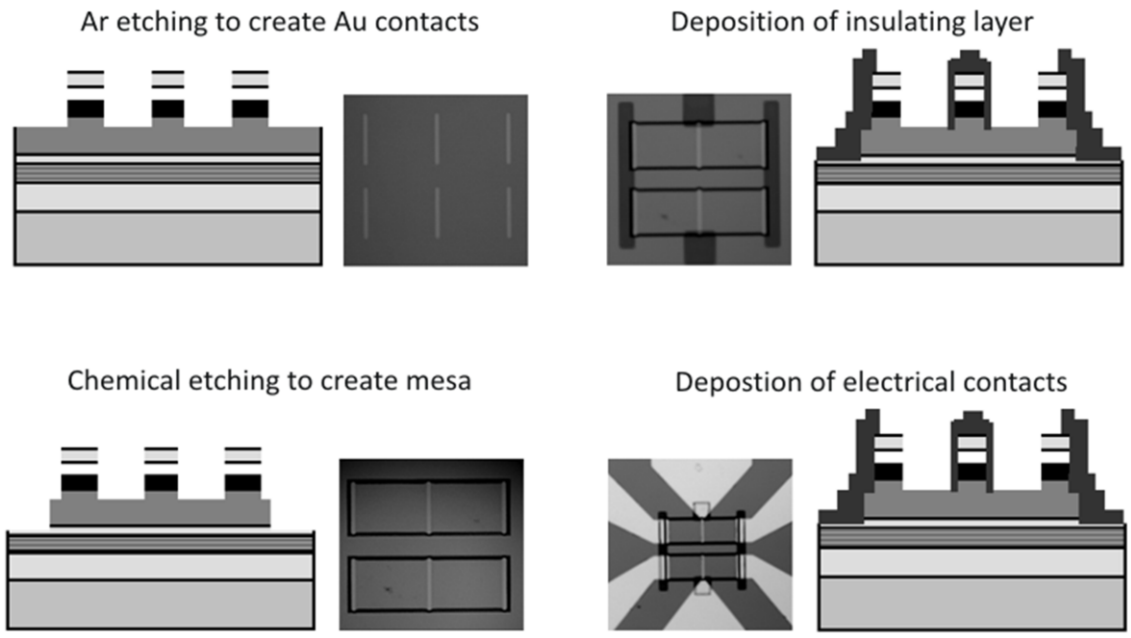

Figure 5.6 Schematics and photos of the 3-terminal device fabrications process showing a) the Fe contacts, b) the mesa structure, c) the insulator pads and d) the electrical pads.

Finally the deposition of Ti and Au contacts was achieved using an evaporator system, with a base pressure of approximately $1x10^{-5}$ Pa, loaded with an electron gun. 90nm of Ti was-deposited at a rate of 0.15nm/s to create strong adhesion to GaAs. 40nm of Au grown at a rate of 0.1nm/s was then deposited to help achieve better electrical contacts.

5.1.4 TEM sample preparation

The preparation of cross-sectional samples thin enough to determine the atomic interface structure is very challenging. Various techniques were used during this study but the most successful samples were those achieved using conventional dimpling and Ar ion polishing [123]. Films were first cut into small pieces approximately 1.5mm square. Two samples were glued together, with the film sides facing, using a 2-part epoxy resin. SiC paper was used to grind the samples to a thickness of approximately 1mm. A sponge polishing pad was used on the dimpler grinder to polish the samples, in a solution containing 0.3µm Alumina balls, to create a smooth surface. This polished side of the sample was then glued onto a Cu TEM grid using the same 2 part epoxy used to glue the films. The process is then repeated- the sample was ground using SiC paper but this time to a thickness of only 120µm. A bronze wheel was then used on the dimpler with diamond paste to grind the sample to a thickness of only 50µm. The sample was then polished using 0.05µm alumina balls to a thickness of ~20µm.

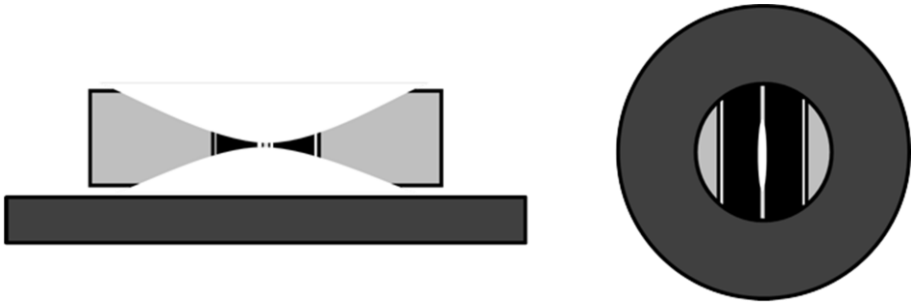

Figure 5.7 Schematic of a cross-sectional TEM sample from the side (left) and below (right).

The final thinning was performed using a conventional precision ion polishing system with Ar ions with an energy of 2.5eV milling from the above and below an angle of 6 degrees. Beam modulation was used to limit heating and ensure uniform etching rates. Once a small hole is formed in the film the sample is milled using Ar ions with energy of 1.0eV at an angle of 4 degrees. A schematic of the final transmission electron microscopy (TEM) samples can be seen in figure 5.7. The area of interest in the electron microscope is the thinnest region lying along the glue line with the areas closest to the hole being the thinnest. If the sample is too thin then it is often damaged, becoming amorphous. This is easy to observe due to the lack of crystallinity

but if an area is chosen that is too thick then atomic resolution imaging is not possible due to multiple electron scattering. Selecting an appropriate region is crucial in obtaining atomic resolution images. Before high resolution imaging, samples are placed in a plasma cleaner to reduce the level of contamination.

Figure 5.8 shows bright field TEM images of a conventional Fe/GaAs(001) sample, prepared using the dimpling method. It can be seen that the film is present on both sides of the hole, separated by the glue line. Higher magnification images show the difference in contrast between the substrate, metallic layers, glue and hole.

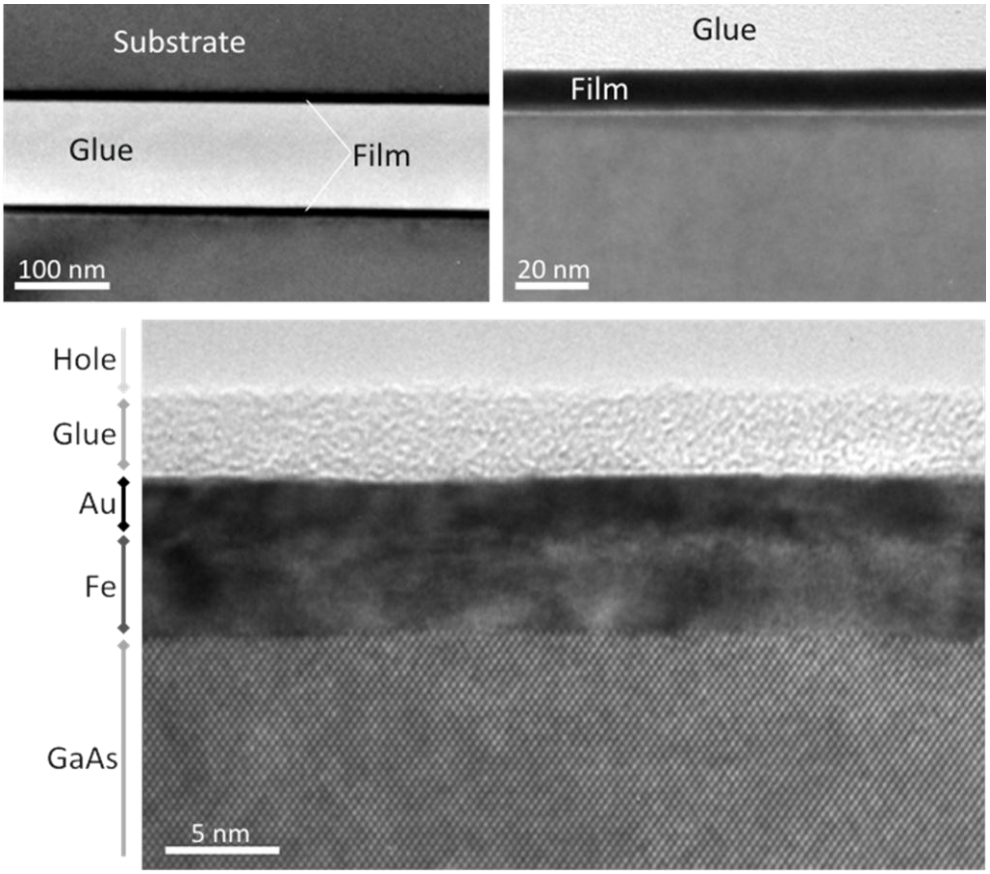

Figure 5.8 TEM images showing very uniform images with large areas suitable for imaging.

The glue is very useful when correcting for astigmatism and spherical aberration, discussed further in section 5.4.4. The GaAs substrate can also be used to calibrate the image as the error in the planar spacings is small. It should be noted that this needs to be done far from the interface as the structure may relax leading to different values for the spacings.

5.2 Magnetic Characterisation

The Magneto-optical Kerr effect (MOKE) magnetometer is one of the most important characterisation techniques for magnetic thin films. This is because the 'Kerr effect'- the change in polarisation or intensity of light reflected from a magnetised sample - is a surface sensitive technique. The effect was first discovered in the late 19th Century by Rev. Jon Kerr [124] after whom the phenomenon was named. There are various configurations of MOKE which can be characterised by the direction of magnetisation: Polar (magnetisation perpendicular to the reflection surface); Longitudinal (magnetisation parallel to the plane of incidence and the surface); and Transverse (magnetisation perpendicular to the plane of incidence and parallel to the surface). A full description of the reflected signal from a magnetic surface can be found in Mansuripur (1995) [125]. One of the most common experimental set-ups is that developed by Bland et al. [126], which analyses the reflected intensity as a function of applied field using a set-up akin to that shown in figure 5.9. In this configuration the change in the detected intensity is directly proportional to the Kerr rotation angle. As the strength of rotation is proportional to the magnetisation, the change in intensity provides information of the sample magnetisation.

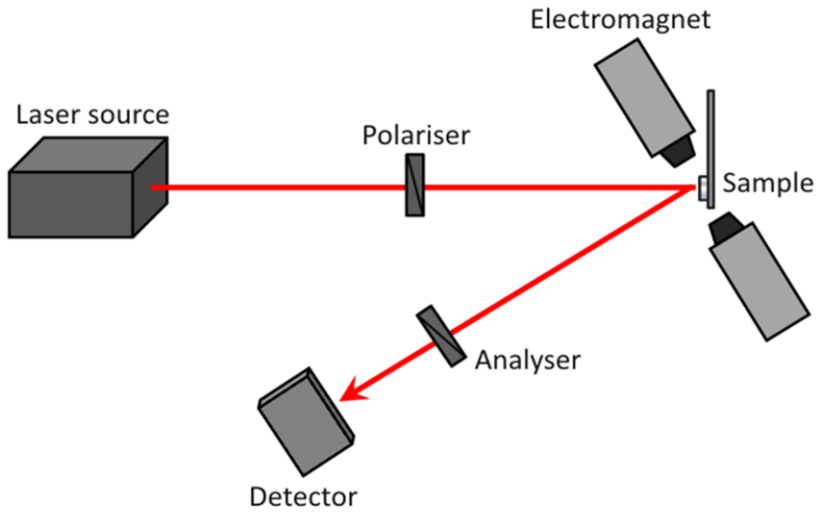

Figure 5.9 Schematic of a MOKE magnetometer [126].

One of the disadvantages of using a MOKE is that an absolute value of the magnetisation cannot be obtained. Hysteresis curves obtained using a MOKE therefore

show the relationship of the normalised magnetisation (M/M_S) to an applied magnetic field. It should be noted that an absolute value of M is not required in this study.

5.3 Transport Characterisation

5.3.1 Scanning Kerr microscopy

An objective lens can be introduced into the MOKE configuration shown in figure 5.9 to create a focussed MOKE system. The advantage of this system is that it allows the magnetisation of nanoelements to be measured.

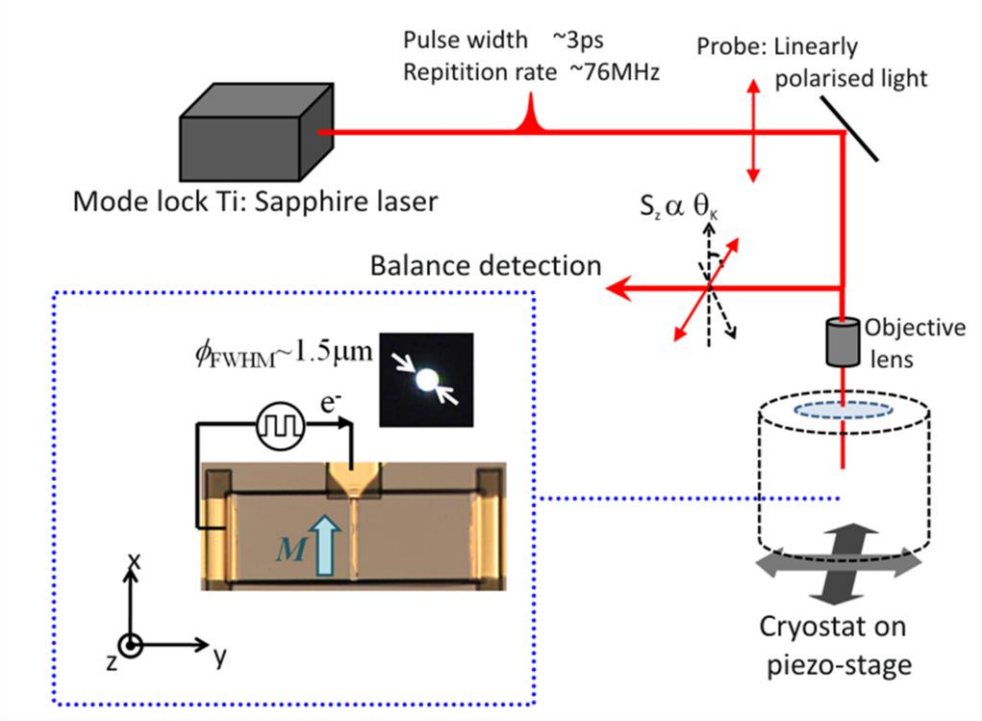

Figure 5.10 Schematic of a scanning Kerr microscopy system.

This configuration is also useful when trying to detect spin accumulation close to an injector contact in conventional spintronic devices. The sample area can be enclosed in a cryostat to allow for temperature dependent measurements to be performed. The introduction of a piezoelectric stage creates a scanning Kerr microscopy (SKEM) system. The advantage of position and scanning with a piezoelectric stage is that it allows the focussed laser probe to be scanned across the area of interest without

affecting the optics. SKEMs are particularly useful when exploring spin accumulation and calculating spin diffusion lengths as the signal can be measured at various distances from the injecting contact.

In this work measurements were obtained by by H. Kobayashi and S. Matsuzaka at the RIEC in Tohoku University using a tuneable pulsed-laser, with an energy linewidth of 10meV, generated by a mode-locked Ti:Sapphire laser. The light is linearly polarised and focussed onto the sample, with a spot size of approximately 1.5μm, through an objective lens. The Kerr rotation of the reflected light is detected by a specially designed balanced detector. The sample is placed in a He-flow cryostat combined with a superconducting magnet, which can apply a static magnetic field, parallel to the optical axis, of up to 5 Tesla. The position of the light probe can be scanned on the sample plane by controlling the position of the cryostat combined with piezo nano-scanning of the stage in two directions.

5.3.2 Electrical measurements

The current-voltage curves are the most important characteristics when it comes to device manufacturing. The electrical measurements were performed with the help of H. Kobayashi and Y. Kaneko at the RIEC at Tohoku University. Conventional *I-V* curves can be obtained through the use of a suitable nanovolt- and nanoamp- meter. The difficulty in measuring samples prepared using photolithography is that despite the deposition of contact pads, the area of the contacts is often very small. After lithography the devices were mounted onto an electrical chip to help protect from damage and also to assist with the electrical measurements. Gold wires were bonded to the electrical contacts using indium and the other end bonded to the chip contact as shown in figure 5.11. The *I-V* characteristics were obtained by applying a constant bias current of between ±400μA and measuring the voltage change. The electrical measurements were performed with the device inside a cryostat so the temperature range was from 10K to room temperature. The currents used are not expected to give rise to any significant Joule heating although this will be discussed further in chapter 6.

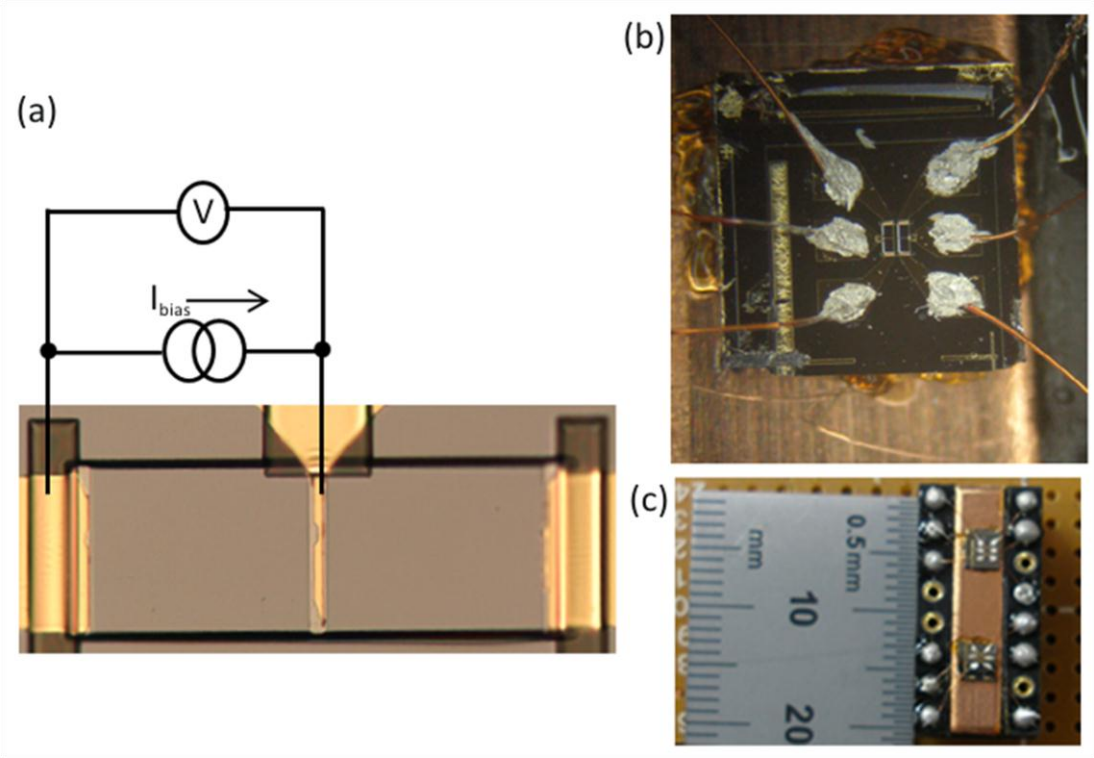

Figure 5.11 (a) Schematic of the electrical set-up with photographs of (b) the indium contacts and (c) the overall chip size.

In order to confirm the injection of spin-polarised electrons across the Fe/GaAs(001) interface the Hanle effect can be utilised [127]. The Fe contacts were first magnetised in-plane by applying a large magnetic field, of the order of 1 Telsa. A constant bias of between ±300μA is then applied between two of the contacts. A spin-imbalance can be detected as the difference in potential (V_2) between the unbiased contact and one of the biased contacts, as described in section 2.2. Applying a transverse field (B_z) causes a precession of the spins leading to a decay of the spin accumulation which follows an approximate Lorentzian line shape given by

$$\Delta V = \frac{\Delta V(0)}{1+\left(\frac{g\mu_B B_z}{\hbar}\tau_s\right)^2} \tag{5.6}$$

where V is the voltage, g is electron g-factor (g=-0.44 used in this thesis), μ_B is the Bohr magneton, B_z is the applied field and τ_s is the spin lifetime. This behaviour is known as the Hanle effect. Hanle curves were obtained over a temperature range of 5-300 K.

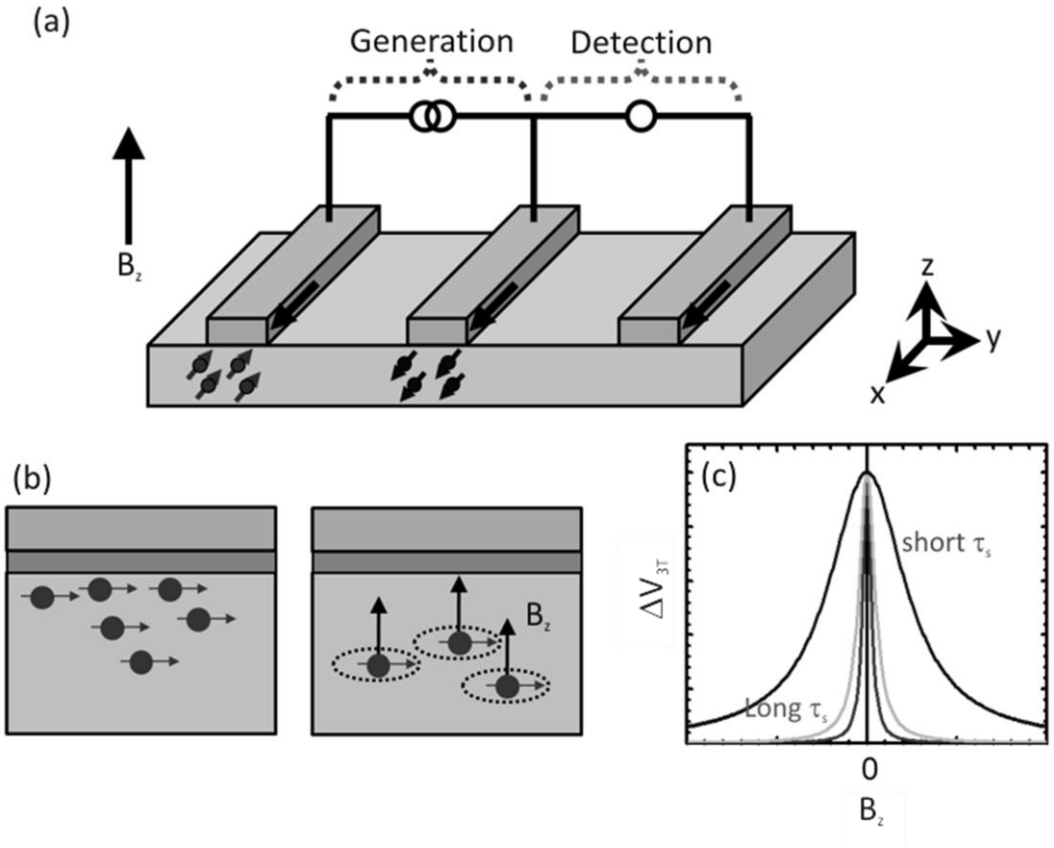

Figure 5.12 (a) Schematic of the 3-terminal Hanle set-up where (b) a field B_z is applied to change electrochemical potential between the two detector contacts and (c) shows three Hanle curves with different spin lifetimes.

Figure 5.12 shows a schematic of the three-terminal set-up used in this study. The figure at the bottom right shows three example Hanle curves which would lead to different spin lifetimes. The wide Lorentzian curve leads to a smaller spin lifetime whilst the narrow curve gives a longer lifetime.

5.4 Interface Characterisation

5.4.1 Transmission electron microscopy (TEM)

Transmission electron microscopy is one of the most powerful techniques for providing structural and chemical information of a sample down to the atomic scale. A conventional set-up for a TEM is shown in figure 5.13 [128].

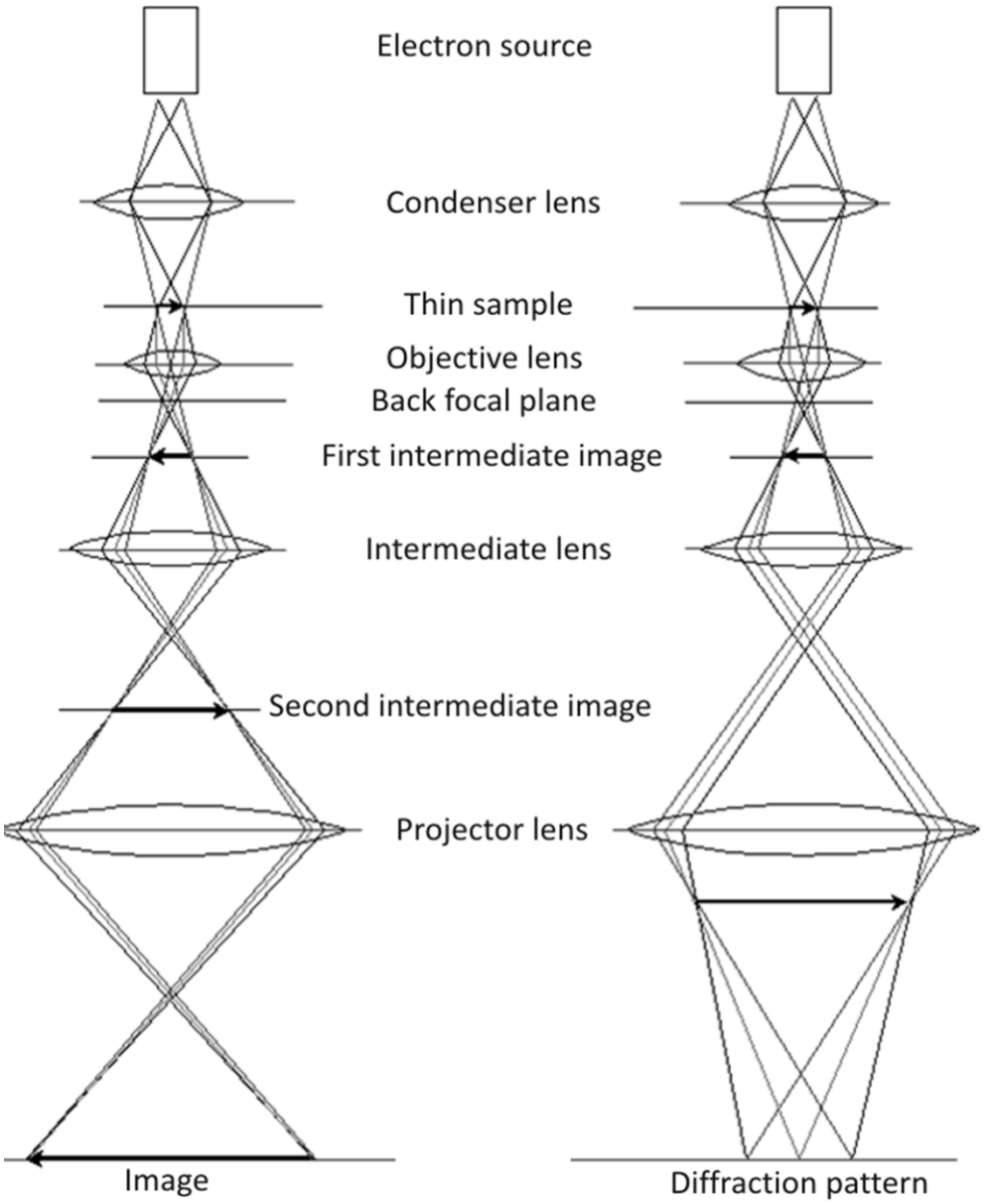

Figure 5.13 Schematic of a conventional TEM showing the image and diffraction pattern formation [128].

In a conventional microscope such as the JEOL JEM-2011 TEM, electrons are emitted from a high voltage LaB_6 filament and accelerated to a high energy, typically 200keV, to produce an approximately monochromatic electron beam. The electron beam is then focussed to a small coherent beam by the condenser lens system, consisting of several electromagnetic lenses and apertures. The condenser lenses are also responsible for varying the spot size and brightness of the beam through manipulation of the strength of the various lenses. The beam is then restricted by a

condenser aperture in order to remove high angle electrons, thus creating a more uniform beam. The electrons then pass through the sample and interact through a variety of mechanisms, shown in the figure 5.14. The scattered elections are focussed by the objective lens to form an intermediate image. This is again focussed by the intermediate lens which has an adjustable strength to allow magnification of the image or diffraction pattern to occur. The image is then magnified again before being focussed onto a fluorescent screen or a charge-coupled device (CCD) camera by the projector lens.

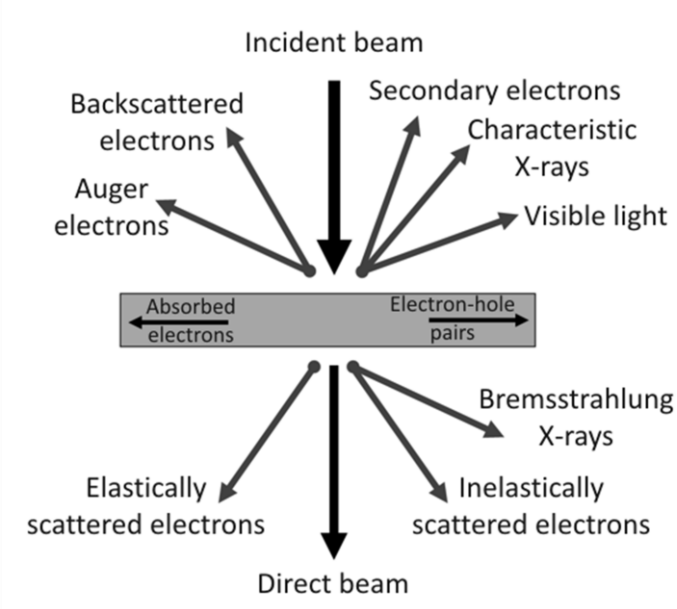

Figure 5.14 Signals generated when an electron beam interacts with a thin specimen [128].

Due to the various interaction mechanisms there are numerous imaging modes available in TEMs with different TEMs specialising in different modes. The most common imaging mode is the bright field imaging obtained by inserting an aperture into the back focal plane of the objective lens, allowing only the main electron beam to pass whilst blocking the scattered electrons. In this case mass-thickness and diffraction are used to create the image contrast.

A dark field image can be obtained in much the same way but the objective aperture is used to block out the main beam and focus instead on the scattered electrons. A diffraction pattern can be obtained through adjusting the magnetic lenses so that the back focal plane, rather than the image plane, is viewed. The insertion of an aperture in the back focal plane allows for the diffraction pattern from a selected

area to be viewed. The diffraction image can provide valuable information about the crystal structure of a sample. High Resolution Transmission Electron Microscopy (HRTEM) is an image mode that uses a large objective aperture to include not only the main beam but also the scattered electron beam. The images are formed by the interference of the diffracted beams with the main beam proving phase contrast. The image quality does, however, get severely reduced through aberrations such as spherical, chromatic and astigmatism. A detailed discussion of all the interactions and contrast mechanism can be found in Williams and Carter [128].

5.4.2 TEM Image simulations

HRTEM image simulations can be a powerful tool when analysing experimental images. HRTEM image simulations were produced using the electron microscopy software JEMS [129]. The simulations were produced using the conventional multi-slice method proposed by Cowley and Moodie [130, 131]. The multislice approximation describes the propagation of the electron wave function through the sample as a series of steps. The specimen is split into N slices of thickness Δz, separated by a distance Δt shown in figure 5.15.

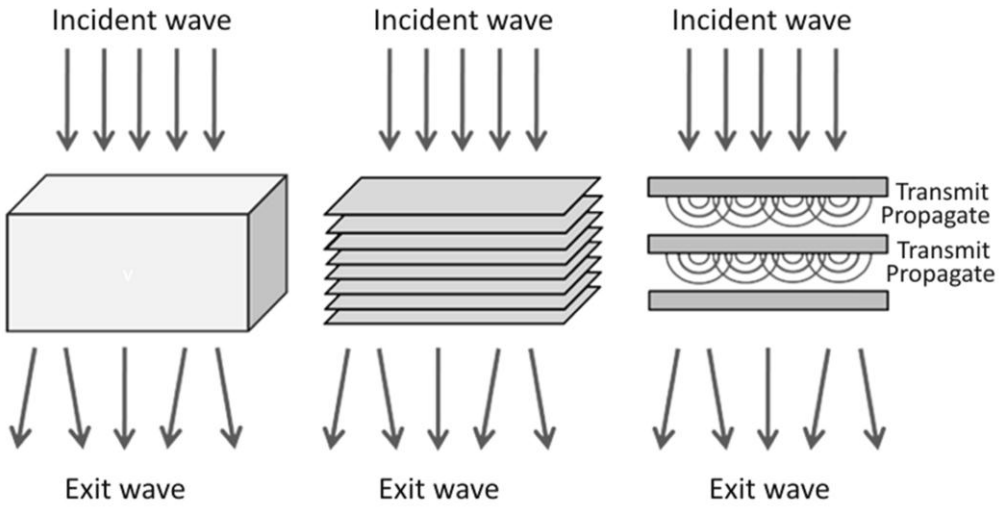

Figure 5.15 The multislice method approximates the specimen into many thin slices with each slice thin enough to cause a small phase shift in the electron wave as it passes through. The electron beam propagates between the slices as small angle outgoing waves [130].

For each slice the projected potential $\varphi(xy)$is calculated from the equation

$$\varphi(xy) = c \cdot \sum_h \sum_k F(hk0) \cdot \exp[2\pi i(hx + ky)] \quad (5.7)$$

where *F* is the Fourier transform of the potential, *c* the unit cell parameter and *h*, *k* are integers over which the Fourier series are summed. The propagation of the electron wave from the exit surface of one slice to the incident surface of another slice is described as Fresnel propagation in vacuum, given by

$$P_F(hk) = \exp\left[2\pi i \Delta z \cdot \frac{\lambda}{2} \cdot \left(\frac{h^2}{a^2} + \frac{k^2}{b^2}\right)\right] \quad (5.8)$$

where λ is the wavelength and *a*, *b* are the unit-cell parameters. The incident wavefunction ψ_0 is calculated and the multislice iterations performed using the equation

$$\psi_N = F(F^{-1}(\psi_{n-1} \cdot P_{F_N}) \cdot q_{PO_N}) \quad (5.9)$$

where the phase object function $q_{PO}(xy)$ is given by

$$q_{PO}(xy) = \exp[-i\sigma\varphi(xy) \cdot \Delta z] \quad (5.10)$$

where σ_{int} is the interaction constant which can be calculated from

$$\sigma_{int} = \frac{2\pi m_0 q}{h^2} \lambda \left(1 + \frac{qE_0}{m_0 c^2}\right) \quad (5.11)$$

where m_o is the electron rest mass, q the charge, E_o the electron energy and c the speed of light. The final exit-wave function ψ_{ex} is obtained when all slices have been taken into account. The focal plane image is then calculated, with the contrast transfer function applied to calculate the HRTEM image.

The parameters used for the simulations were chosen to represent the experimental parameters for the JEOL JEM-2200FS TEM. These were: acceleration voltage 200kV, chromatic aberration (Cc) 1.6mm, spherical aberration (Cs) 0mm, fifth order spherical aberration (C5) 0.5mm, energy spread 0.7eV, objective lens stability 0.5ppm and focal spread 2.98nm. An example of the simulations is shown in figure 5.16 for a GaAs(001) crystal in the [110] projection. The figure shows an example of the a) projected potential, b) Fresnel propagator, c) phase object function, d) contrast

transfer function (CTF), e) atomic positions and f) image simulation calculated using the JEMS software.

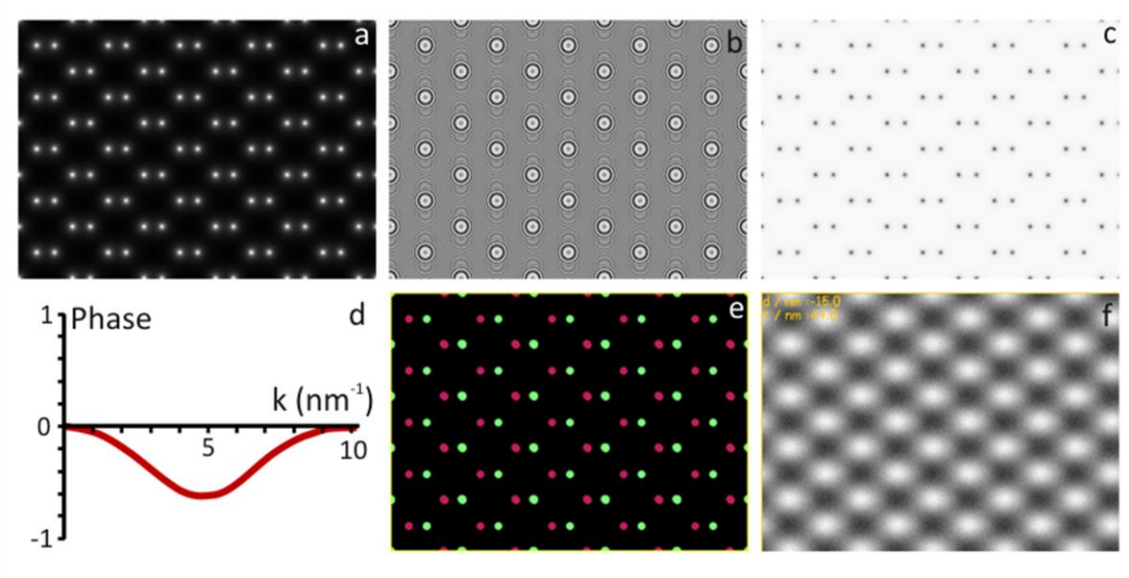

Figure 5.16 Example of the a) projected potential, b) Fresnel propagator, c) phase object function d) contrast transfer function, e) atomic positions and f) image simulation of GaAs(001) in the [110] projection.

One of the advantages of using an aberration corrected microscope is that it allows for sub atomic resolution as the CTF does not cross zero for the resolution range of interest. The CTF shown in figure 5.16d is that obtained for the aberration corrected JEOL JEM-2200FS obtained for a defocus value of -3nm. Changing the defocus value causes a change in the CTF leading to a change in the image simulation. This effect will be shown for the Fe/GaAs(001) interface in section 6.3.1 as well as the effect of the sample thickness.

There are several limitations of the multislice method. One of these is that the specimen structure has to be defined in detail, so the atomic positions and spacings are required. These are often not known, particularly when analysing interfaces. Another problem is the specimen thickness which is not easily obtained from experiment. The defocus value for the image, crucial when performing the simulations, is also not well known. Simulations are therefore usually performed for various values of thickness and defocus and later matched to experimental images.

5.4.3 Scanning transmission electron microscopy (STEM)

Despite the first scanning transmission electron microscope (STEM) being built in the 1930s it wasn't until the 1970s that the machines started to become popular, due largely to technical and engineering difficulties. In order to collect a large enough signal from thin specimens a large current is required from the electron gun whilst keeping the probe size as small as possible. This became possible through the use of field emission guns (FEGs) which can generate current densities of $10^{10}A/m^2$, 6 orders of magnitude greater than that of conventional thermionic emission filaments.

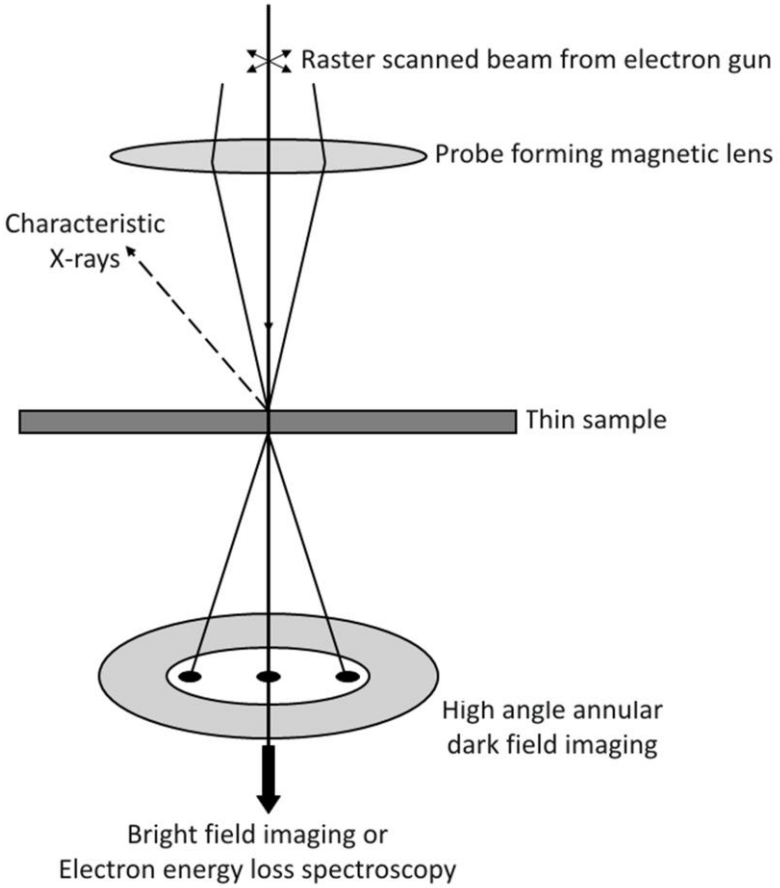

Figure 5.17 Schematic of a STEM showing the key interactions [128].

Using a raster to scan a focussed electron beam allows for additional imaging techniques not available in conventional TEM. One of the greatest advantages of STEM is that it allows for multiple signals to be collected simultaneously which can be used for quantitative analysis. Another advantage is the ability to use high angle annular dark field (HAADF) detectors to acquire the signal from high-angle elastically scattering

electrons, providing atomic number (z-contrast) imaging. Several imaging modes obtained for a Fe/MgO/Si sample are shown in figure 5.18. The z-contrast provided from the HAADF detector is clearly visible and provides a powerful technique for compositional analysis. If the microscope has the appropriate set-up then the bright-field image can be obtained at the same time, and appears very similar to a conventional bright-field TEM images. Energy dispersive X-ray (EDX) mapping is also shown with the layers well defined. It can also be seen that the Fe layer has an increased level of O, as expected.

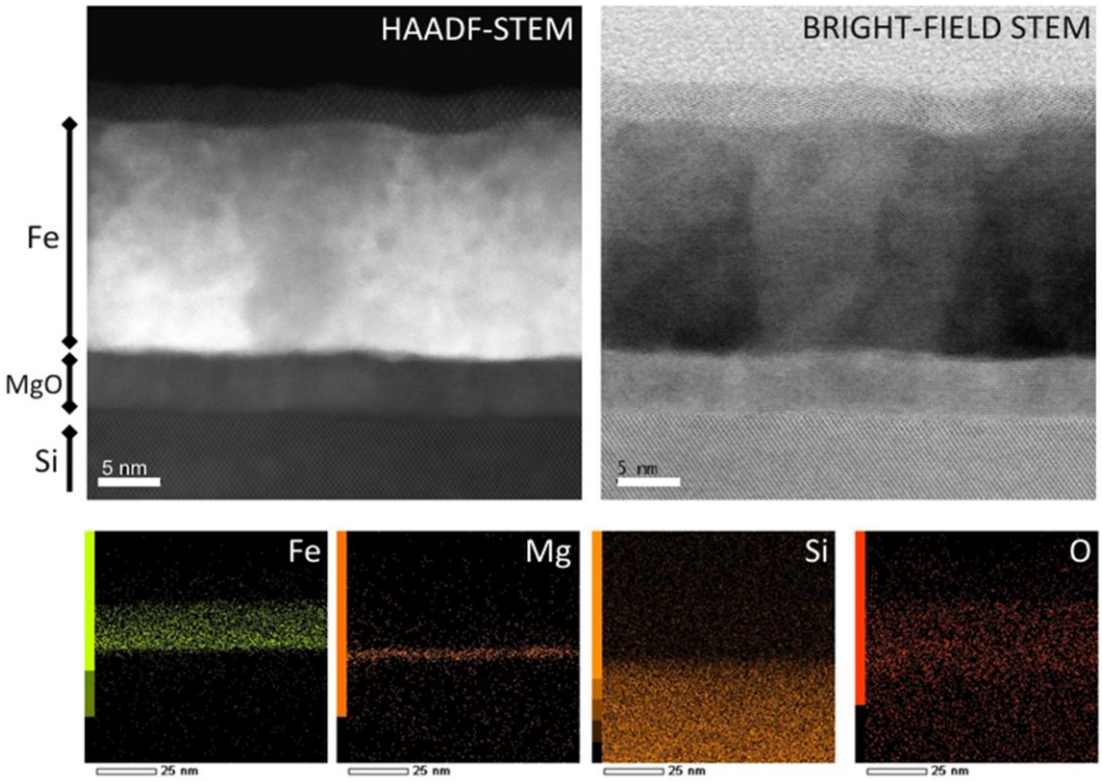

Figure 5.18 HAADF and bright field STEM images of a Fe/MgO/Si sample with EDX mapping.

EDX maps are an extremely useful tool when performing quantitative compositional analysis but the time needed to obtained strong enough signals in conventional STEMs is typically over 30 minutes. As the image needs to be continually corrected for drift and will also suffer significantly from beam damage and contamination, this technique is not as suitable for atomic compositional analysis. HAADF-STEM therefore remains the most useful imaging tool for atomic interface analysis, particularly when trying to determine the composition. The STEM images obtained in this work were performed with the help of Prof. K. Yoshida from Nagoya University.

5.4.4 Aberration corrected microscopy

Electron microscope manufacturers and microscopists are always aiming to achieve the highest resolution. In order to improve the resolving power the inherent aberrations need to be addressed. In conventional TEM the most important aberrations arise from the objective lens, whereas in STEM the aberrations of the probe-forming lens are crucial. There are two main types of aberrations in electron microscopes: geometrical aberrations, such as spherical aberration, and chromatic aberrations which arise from the electron-energy dependence of the refraction properties of magnetic fields. To reduce the effect of chromatic aberrations cold FEGs with an energy spread of ~0.3eV at the full-width half-maximum (FHWM), 3 times smaller than Schottky hot field emission guns, and energy filters (monochromators) can be used. In electron microscopes the electron beam is focussed using electromagnetic lenses which act as converging lenses.

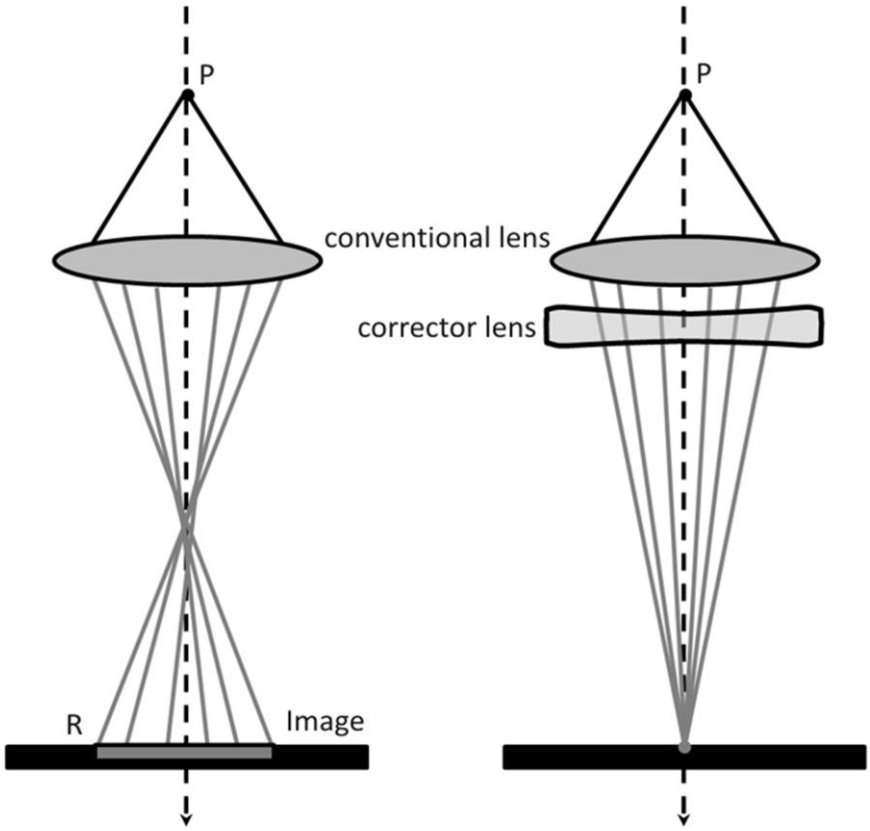

Figure 5.19 Schematic of the spherical aberration of a converging lens. The image of a point P of the specimen is broadened, compensated by combining the converging lens with a diverging lens [132].

An ideal converging lens would image a point in a sample to a corresponding point in an image. In electron microscopes the image is broadened into a point-spread disk due to the spherical aberration. An electron which passes closer to the electromagnet will experience a greater force and be more focussed than an electron passing closer to the optical axis. The first proposal to correct for this aberration was provided by Scherzer in 1947 who suggested using multipole lenses to create a lens with a negative spherical aberration [132]. Multiple lenses are characterised by their rotational symmetry such as dipole, quadrapole, hexapole. There are two main types of aberration corrector: the quadrupole-octopole and the round lens-hexapole corrector [133-136]. In both systems there is usually a system of lenses that act as the corrector, usually the octopoles or hexapoles, whilst the other lens, the quadropoles or round lenses, steer the electron trajectories.

In this work HRTEM and HAADF-STEM images were obtained using a double aberration corrected JEOL JEM-2200FS microscope. This machine has an aberration corrector for both the probe, ensuring the electrons are focussed to a spot less than 1 nm, and also after the beam has passed through the sample, correcting for the spherical aberration. Both aberration correctors are based on the long hexapole/transfer lens system [137]. The off-axial aberrations are corrected for by means of a transfer-lens doublet (D1), which consists of two conventional round lenses.

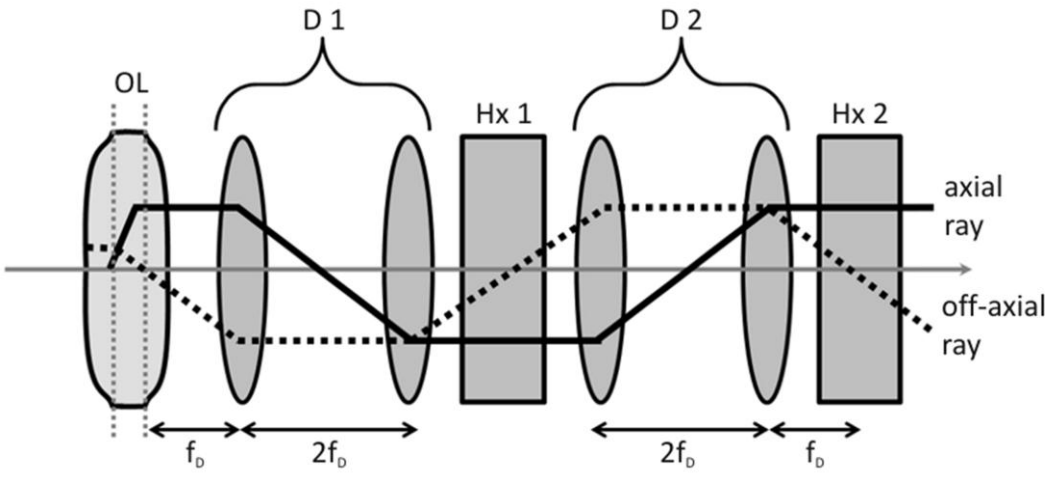

Figure 5.20 Schematic of the long hexapole/transfer lens system employed in the JEOL JEM-2200FS microscope to correct the spherical aberration [137].

A hexapole lens (Hx 1) is used to correct for the spherical aberration, with a second hexapole lens (Hx 2) used to correct for the non-rotationally symmetric second-order aberrations which are induced by Hx 1. A second transfer-lens doublet is used to correct the off-axial aberrations between the two hexapole lenses. It should be noted that although this set-up corrects for the third-order spherical aberration a fifth-order aberration remains. It is important that this aberration is kept to a minimum through correct alignment of the microscope.

The aberration coefficients are determined using an extended version of the diffractograms-tableau method proposed by Zemlin *et al.* [138]. This method calculates the coefficients by analysing the diffractograms of an amorphous sample obtained at different beam-tilt angles. The lens currents required to compensate for the aberrations are calculated using software developed by Corrected Electron Optical Systems (CEOS). Subsequently the current is applied to the appropriate lens or stigmator and a new diffractograms-tableau calculated.

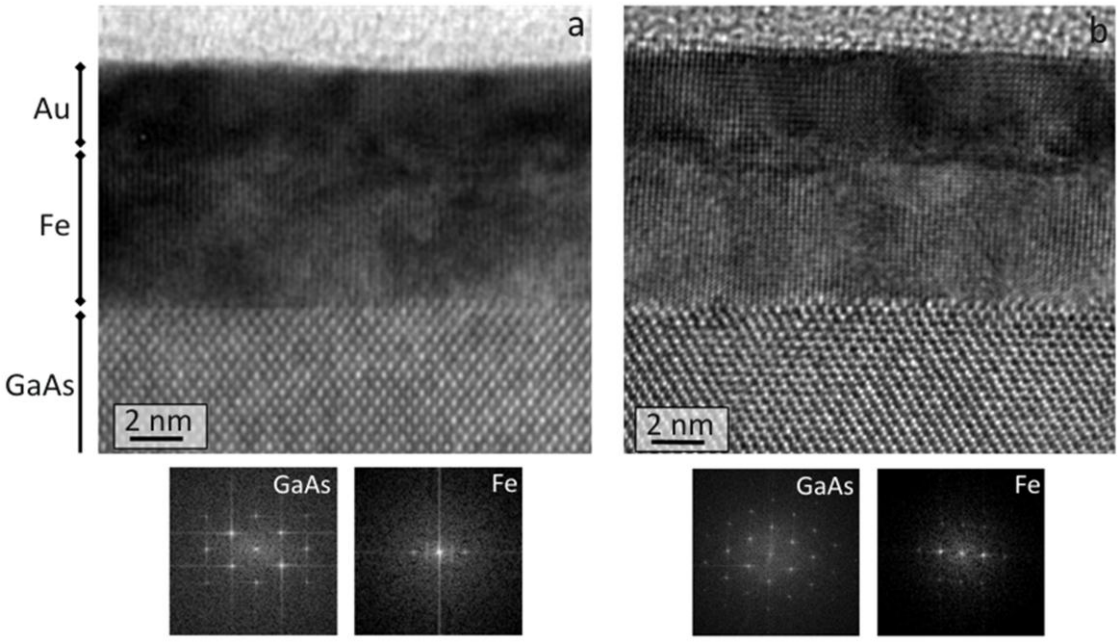

Figure 5.21 TEM images of a Au/Fe/GaAs sample from a) an uncorrected and b) aberration corrected microscope.

When appropriately low values for the aberrations are obtained the lens settings can be stored to assist with future alignment. Figure 5.21 shows typical TEM images obtained from a) an uncorrected JEOL JEM-2011 and b) the aberration corrected FS2200 microscope of a Au/Fe/GaAs(001) sample. It can be seen from the figure that

the aberration corrected machine provides significantly better resolution, with the horizontal lattice planes of the Fe and Au layers not visible on the uncorrected image. The improvement is more evident when analysing the digital diffractograms, with significantly more diffraction spots visible. It is also clear that the interface structure for the film is not as abrupt as they appear when analysing the uncorrected images.

Chapter 6. Interface Structure

The interface atomic structure in epitaxial Fe/GaAs(001) films is critical in determining the resulting Schottky barrier properties. Recently the advent of high resolution Cs corrected TEM and HAADF-STEM systems has allowed the interface structure at the atomic scale to be imaged. These images together with image simulations allow for the identification of individual atoms in terms of their species and location. Once these structures are known ab-initio calculations can be used to determine the transport properties and spin injection efficiencies as well as seeking to determine the strength and position of interface resonance states.

6.1 Fe/GaAs(001) interface

6.1.1 Theoretical structures

There are various theoretical structures that have been predicted for the Fe/GaAs(001) interface, summarized by Erwin *et al.* in 2002 [139]. Density functional theory (DFT) was used to explore the nucleation, growth and interface structures in Fe/GaAs(001) films. This study and subsequent work focuses on three different interface structures: the abrupt, partially one-layer mixed and fully two-layer mixed interfaces [47, 139]. These calculations suggest that Fe has preferential bonding to As rather than Ga atoms. The abrupt interface is therefore the most energetically

favourable for an As terminated surface with the formation energy (per unit cell) ~0.29eV lower than the partially mixed interface and ~1eV lower than the fully mixed interface. If the surface is Ga terminated the preferential Fe-As bonding leads to some mixing. Partial mixing is 0.36eV more energetically favourable than the abrupt interface and 0.86eV lower than a fully mixed interface [47, 139]. There are several other interface structures that have been predicted but these are expected to form after high temperature post-deposition annealing or for films prepared with high growth temperatures for Fe [48, 140]. One of the most discussed is the Fe_3Ga interface as this is predicted to cause an enhancement in minority-spin injection. This could even lead to a reversal in the sign of spin-polarised electrons [140]. These phases are, however, not predicted to occur until annealing at temperatures above 450°C or for growth temperatures of Fe above 175°C. As the temperatures required to create the Fe_3Ga and other phases are much higher than those used in this study and other key studies [43-46] they will not be discussed in detail.

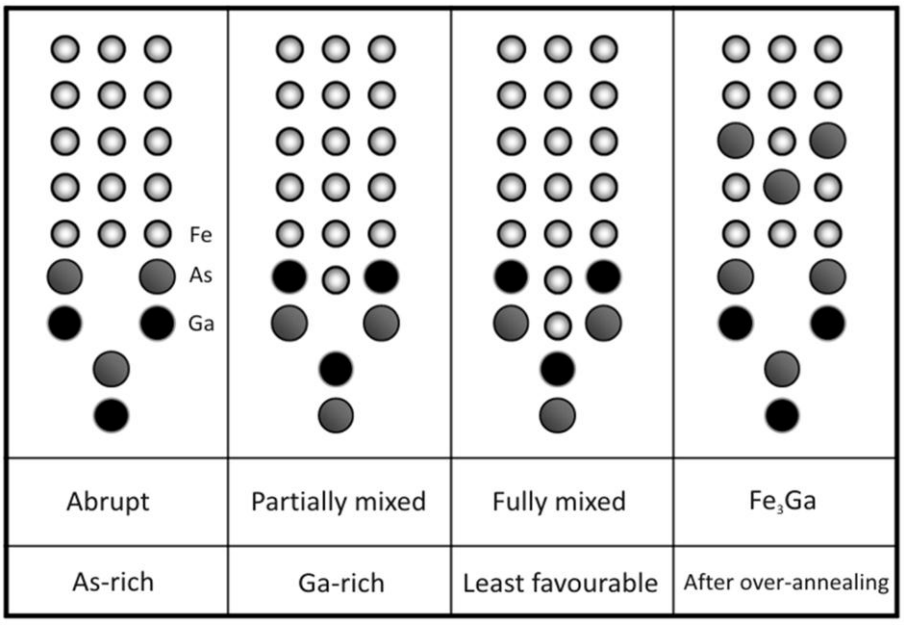

Figure 6.1 Theoretical structures of the Fe/GaAs(001) interface [47, 139, 140].

A summary of the key interface structures can be seen in figure 6.1. One of the main differences between the interface structures is that they lead to different Schottky barrier heights. Calculations for the abrupt interface suggest that the barrier height is ~0.9eV. If partial mixing occurs the barrier height is reduced to ~0.6eV if the surface is As-terminated, and ~0.7eV if the surface is Ga terminated [47]. Although no

calculations have been performed on the barrier height for the fully mixed interface it is expected to lead a further reduction in the barrier height. It should be noted that in most experimental studies the GaAs layer is treated to ensure it is uniform, with an As-terminated surface usually created to help limit the diffusion of Ga atoms into the Fe layer [47]. The absolute value of the barrier height can have a significant effect on the spin-polarised injection efficiency as a lower barrier leads to a higher contribution to the current from thermionic emission as electrons require less energy to overcome the barrier. As tunnelling is required for efficient injection a low barrier height can lead to a reduction in the injection efficiency. As well as having an effect on the Schottky barrier height the atomic interface structure also has a significant effect on the formation of interface resonance states (IRS). The location and strength of IRS is extremely sensitive to the atomic interface structure and the interatomic spacings. There are, however, currently no calculations that have been performed on the partially mixed or fully mixed structures so the effect of the interface structure on the location and strength of IRS is not known.

6.1.2 Observed structures

There have been two major previous observations of the Fe/GaAs(001) interface using HAADF-STEM. The first was performed by Zega *et al.* in 2006 [45] who reported a partially mixed interface for an As-terminated surface. This structure is quite unexpected as an As terminated surface is predicted to give rise to an abrupt interface as it has a formation energy ~0.29eV lower than the partially mixed structure. It should be noted that the images analysed in this report were filtered using conventional mask techniques in a digital micrograph. Great care is needed when applying masks to HAADF-STEM images as filtering can create periodic peaks in the intensity. As the unfiltered images are not accessible it is unclear if the images were significantly altered during the mask process. Confirmation of this structure has not been reported by this or any other group.

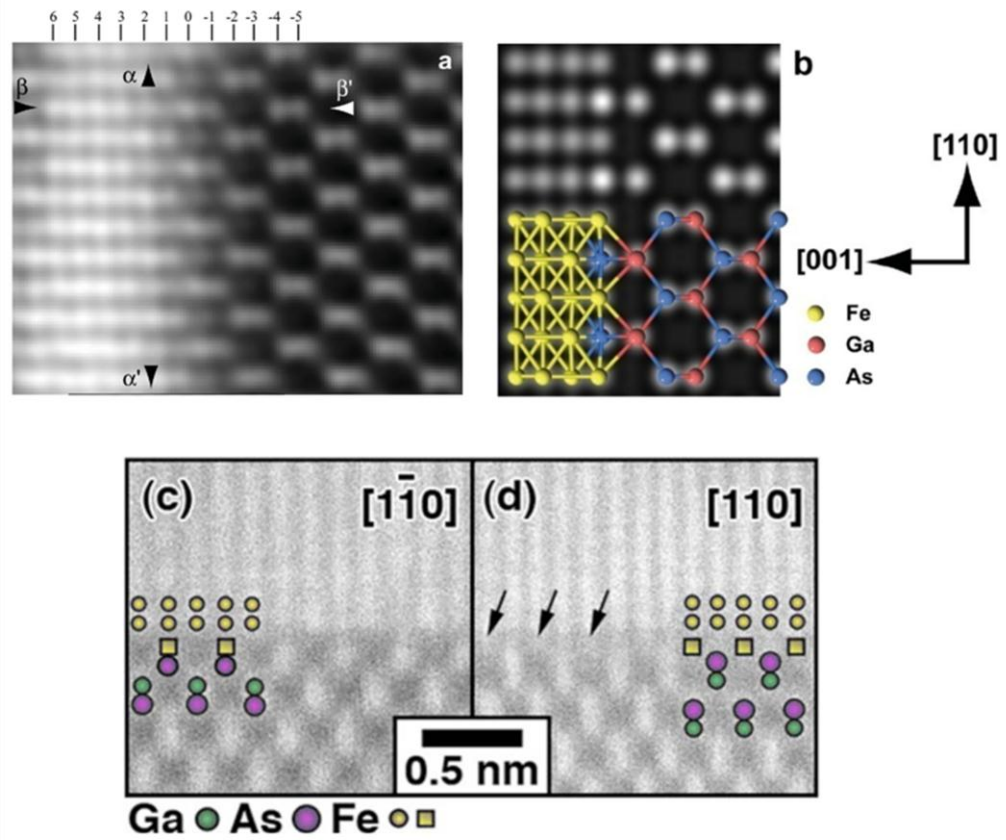

Figure 6.2 Figure showing the two previous experimental reports with a,b) the HAADF-stem image from Zega *et al.* [45] and c,d) those from Le Beau *et al.*[46].

The second report was by Le Beau *et al.* [46] in 2008. In this study a different type of structure, consisting of a single partially occupied plane was inserted between the Fe film and GaAs layer as shown in figure 6.2. This structure was suggested by observing along two different orientations. It should be noted that the images are quite noisy and no simulations were used to help analyse the interface structure. This structure has never been predicted or studied theoretically so little is known of the effect of vacancies. It is also yet to be verified experimentally by another group.

It is not clear why the interface structures observed from the two studies differ but one possible reason could be the GaAs(001) surface reconstruction used before depositing the Fe layer. In most studies the GaAs layer is treated with an As-terminated surface usually created to help limit the diffusion of Ga atoms into the Fe layer [47]. There are many different As-rich GaAs(001) surface reconstructions that can be formed, discussed in detail in a review by Wastlbauer and Bland [117], with different groups tending to use different reconstructions. The most common

reconstructions used are the (1x1), (2x4) and (4x4) but it should be noted that there are several variations of the (2x4) and (4x4) reconstructions. A (2x4) reconstruction is created by annealing a GaAs(001) substrate to between 500°C and 600°C in an As-rich environment, usually achieved by applying an As-flux of $3x10^{-5}$ Pa. The conditions to create a (4x4) surface are similar to those for (2x4) but the sample is slowly cooled under the As-flux from approximately 500°C to 200°C in steps of 20°C/hour. A (1x1) reconstruction is created by annealing under UHV conditions to approximately 600°C or higher temperatures if an As-flux is applied. A detailed review of how to create the surface reconstructions can be found in the surface science report by Ohtake [141].

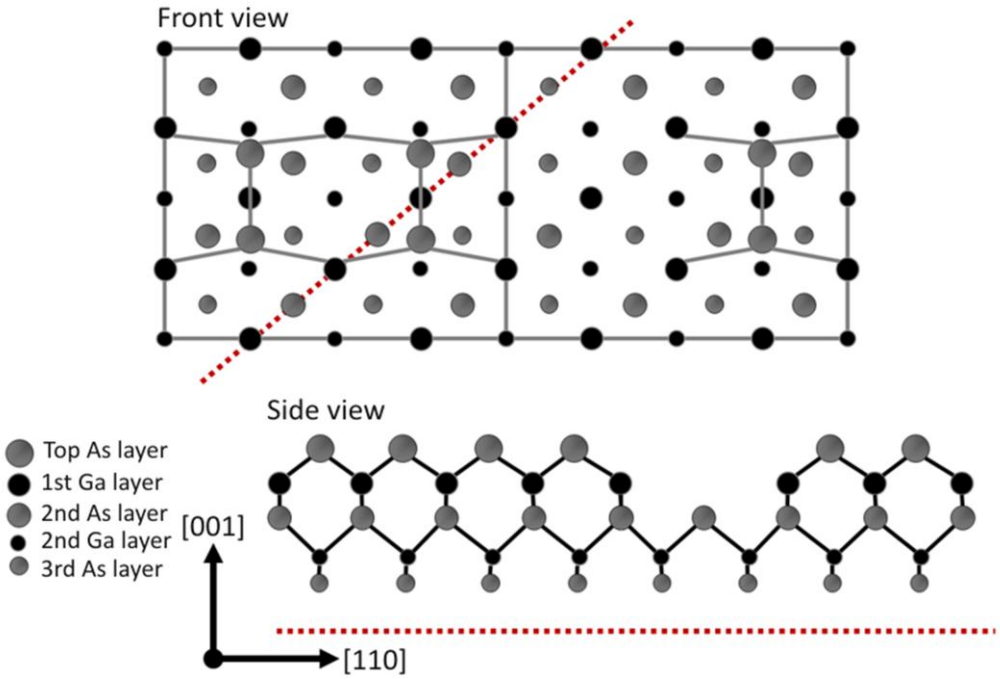

Figure 6.3 Schematic of the GaAs β(2x4) surface reconstruction [141].

In the report by Zega *et al.* [45] the Fe layer was grown onto a GaAs(001) substrate with a (2x4) surface reconstruction. Although there are different types of (2x4) surface reconstruction the general structure is similar to that shown in figure 6.3 [141]. It can be seen that the surface is As-terminated, to limit the diffusion of Ga, but the surface contains both trenches and surface As-dimers. The effect of this surface reconstruction on the subsequent growth of thin Fe films is not known.

In the study performed by Le Beau *et al.* [46] the Fe was-deposited onto a GaAs(001) substrate with a (4x4) surface reconstruction, with a structure similar to

that shown in figure 6.4 [141]. It can be seen that the surface is again As-terminated but the surface now contains trenches and different types of dimers. The (4x4) surface reconstruction contains both As-As and As-Ga dimers. The effect of this surface reconstruction on the interface structure is not known but as this reconstruction contains fewer trenches than the (2x4) reconstruction, it is more As-rich. This suggests that the level of Ga diffusion for the (4x4) reconstruction will be lower than that for the (1x1) and (2x4) and could lead to higher quality interfaces. Detailed knowledge of the effect of the interface structure is, however, not known.

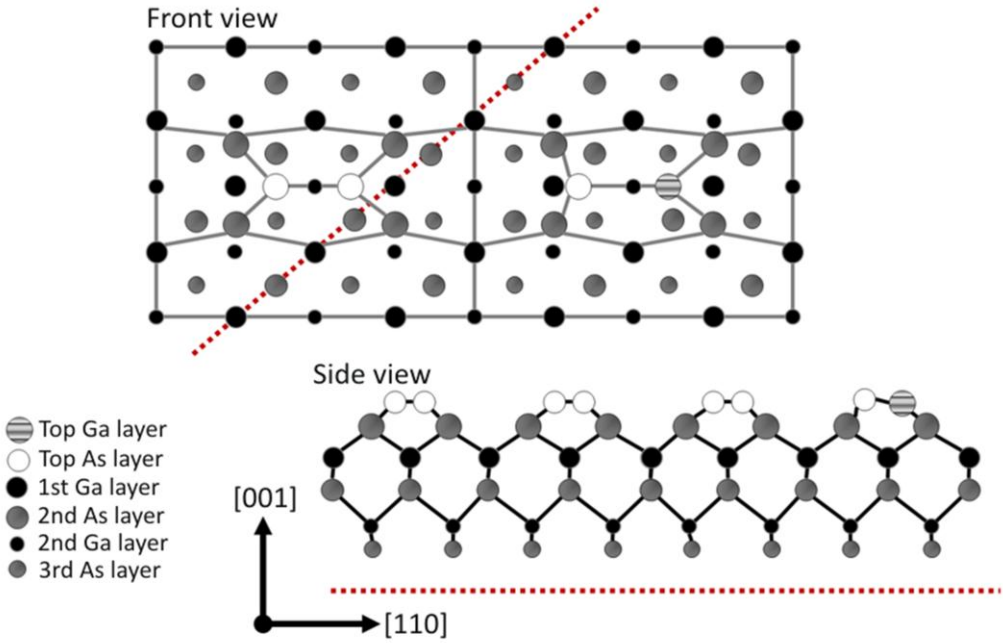

Figure 6.4 Schematic of the GaAs c(4x4) surface reconstruction [141].

From these reports it is clear that there is little understanding of the atomic interface structure of Fe/GaAs(001) films. The interatomic spacings of the observed interfaces are also yet to be reported. These are of great importance as they are essential in order to perform calculations to determine the strength and position of IRS. It should be noted that the studies by Zega *et al.* [45] and Le Beau *et al.* [46] did not discuss the relationship between the atomic interface structure and the transport properties. This is crucial if these systems are to be used in future devices.

6.2 Film growth

6.2.1 MBE deposition

Details of the sample growth were provided in section 5.1.1. Figure 6.5a shows the complex GaAs surface reconstruction after annealing the substrate at 500°C, before the Fe deposition. As the surface was annealed in an As-rich environment, created by desorbing the As-cap, and heated to a temperature of 580°C the surface is expected to be As-rich.

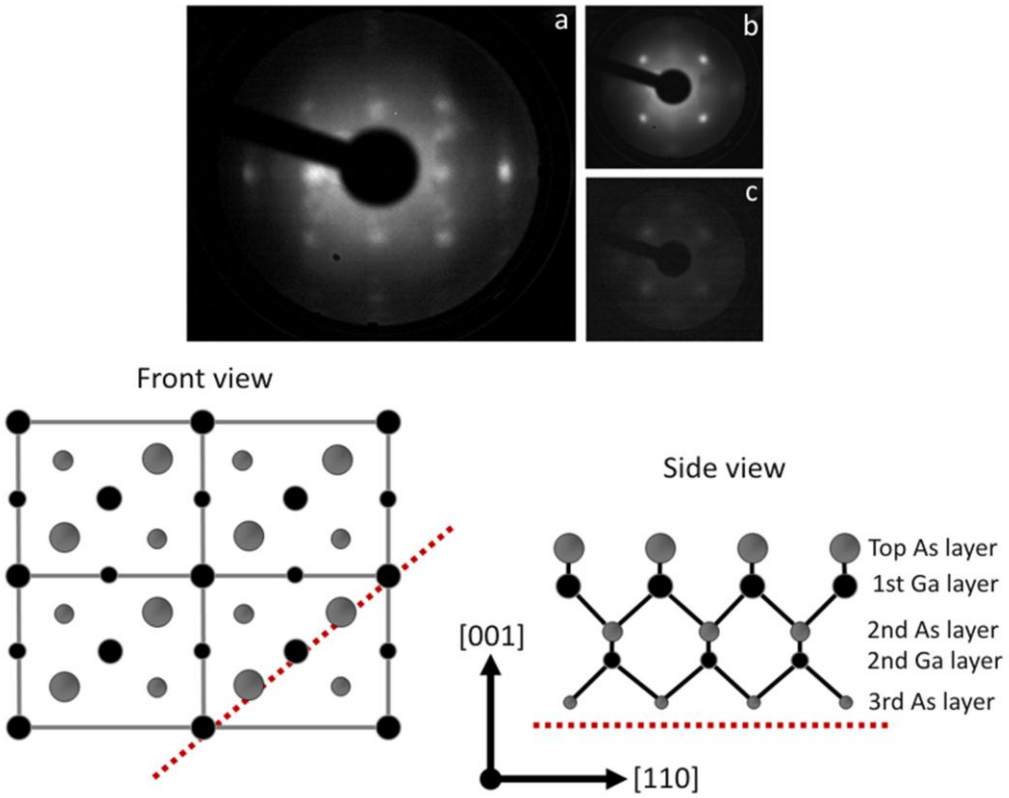

Figure 6.5 LEED image showing a) the GaAs surface reconstruction, b) epitaxial Fe and c) Au growth. The bottom schematics show the ideal GaAs(001) (1x1) surface reconstruction [141].

The LEED pattern suggests that an As-terminated (1x1) surface has been created, observed previously by other groups e.g. [142]. A schematic of the ideal GaAs(001) (1x1) surface reconstruction is shown in figure 6.5. It can be seen that the surface is predicted to be As-rich, therefore favouring the formation of an abrupt interface. Figure 6.5b shows the LEED pattern obtained after depositing a 5nm thick Fe film, with the epitaxial growth relationship Fe(100)<001>||GaAs(100)<001>, at room temperature. The position and intensity of the spots shows that the film was grown

epitaxially onto the As-rich n^+GaAs(001) layer. A thin 3nm Au capping layer was-deposited to prevent oxidation. Figure 6.5c shows the LEED pattern obtained after deposition. The loss of the LEED spots shows the Au was not grown epitaxially as expected due to the large lattice mismatch of ~29%.

6.2.2 Semiconductor doping profile

Simulations were performed to explore the shape of the conduction band for the samples studied using the method discussed in section 5.1.2. At the Fe/GaAs(001) interface a 12nm thin layer of highly n^+doped GaAs, with a free carrier density on the order of 1×10^{19} cm^{-3}, was-deposited onto a moderately n^-doped GaAs layer with a free carrier density of the order of 1×10^{16} cm^{-3}. In order to perform the calculations the Schottky barrier height needs to be specified. As this is difficult to obtain experimentally as discussed in section 7.2.1, calculations were performed for different values of the barrier height, shown in figure 6.6.

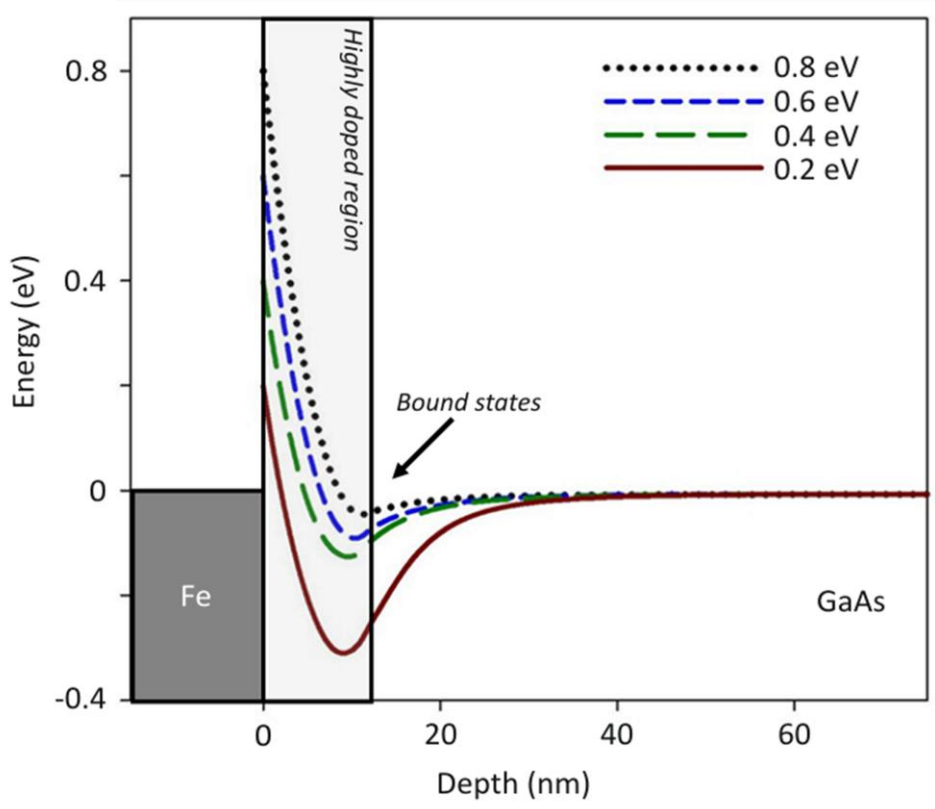

Figure 6.6 Band structure calculations showing the shape of the conduction band for various values of the Schottky barrier heights.

It can be seen from the figure that the doping profile does not give rise to a pronounced band bending to the level seen in other reports [84, 118]. The amount of bending is, however, dependent upon the Schottky barrier height. As the barrier height is reduced the bending is enhanced and the possibility of bound states increased. Although the value of the Schottky barrier height varies between experiments, the values generally fall in the range of 0.2-0.8eV [143, 144]. It is very difficult to determine experimentally the barrier height in these systems but calculations suggest that an abrupt interface has a height of approximately 0.8eV. If mixing occurs this is predicted to reduce the barrier height to approximately 0.5eV [47]. Both of these values are large enough to suggest that no pronounced band-bending occurs.

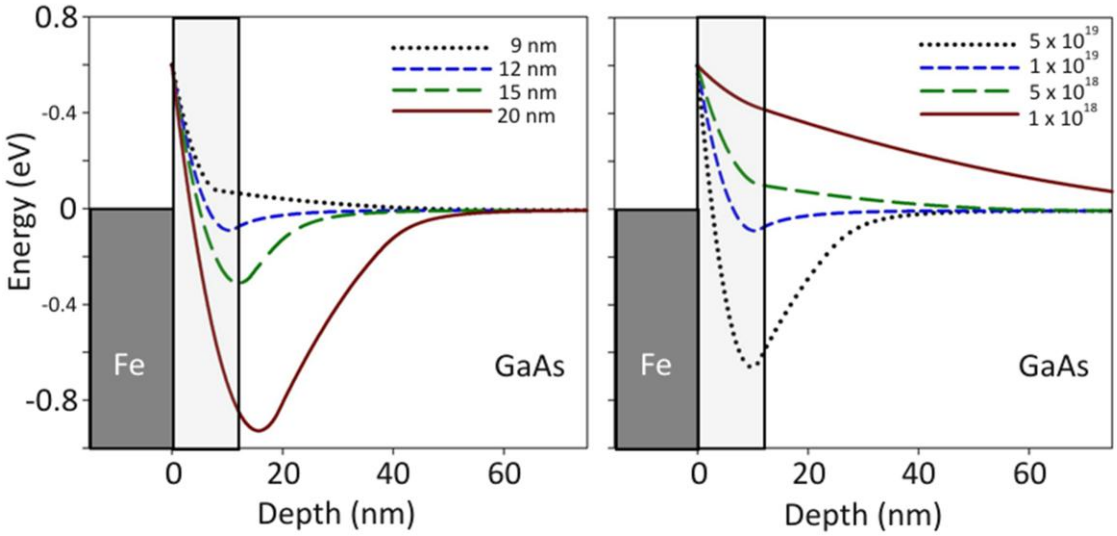

Figure 6.7 Band structure calculations showing the shape of the conduction band for different thicknesses ($n=1x10^{19}cm^{-3}$) or different doping densities (width = 12nm) for a barrier height of 0.6eV.

If the barrier height is assumed to be 0.6eV, the effect of the width of the highly doped region and the doping density can have a significant effect on the shape of the conduction band, shown in figure 6.7. The effect of the width of the highly doped region is shown for a doping density of $1x10^{19}$ cm^{-3}, the value used in this study. For a width of 12nm only slight bending occurs and no bound states are created. This is also the case if the width is reduced to 9nm. If the width is too low, below approximately 8 nm, then the reduced number of carriers leads to an increase in the depletion region width, exceeding the width of the highly doped region. This causes the tunnelling

current to be negligibly small across the barrier. If the barrier width is greater than 12nm then the level of band bending begins to increase significantly. This has also been shown by Hu *et al.* [118] and is particularly relevant to the experiments performed by Lou *et al.* [44] as the doping profile used in their study had a width of almost 30nm. With such pronounced bending, bound states form in the semiconductor. The tunnelling DOS in forward bias can then be dominated by the DOS in the quantum-well like structure in the conduction band, which is partially filled with electrons. The effect of the doping density is shown in figure 6.7 for a highly doped region width of 12nm. If the doping density is too low then a large depletion width forms due to the reduced number of free carriers. This causes the tunnelling current to be negligibly small across the barrier. As the doping density increases the width of the barrier decreases, with no pronounced bending visible when the doping density is $1x10^{19}cm^{-3}$. If the density is increased to $5x10^{19}$ cm^{-3} then a quantum-well like structure forms creating bound states.

In the structures used in this work the doping profile was carefully selected to form a sufficiently thin barrier of approximately 12nm, thus allowing tunnelling to be the dominant transport mechanism. The doping profile also eliminates the possibility of tunnelling from bound states as the shape of the conduction band does not create a quantum-well like structure as long as the barrier height is sufficiently large, above ~0.3eV.

6.2.3 Magnetic properties

The magnetic properties are important to confirm that the sample has not oxidised or become damaged. They also allow for the easy and hard anisotropy axes to be determined which are used in the electrical measurements. The hysteresis loops obtained using a conventional MOKE magnetometer along the [110] and [1-10] directions can be seen in figure 6.8.

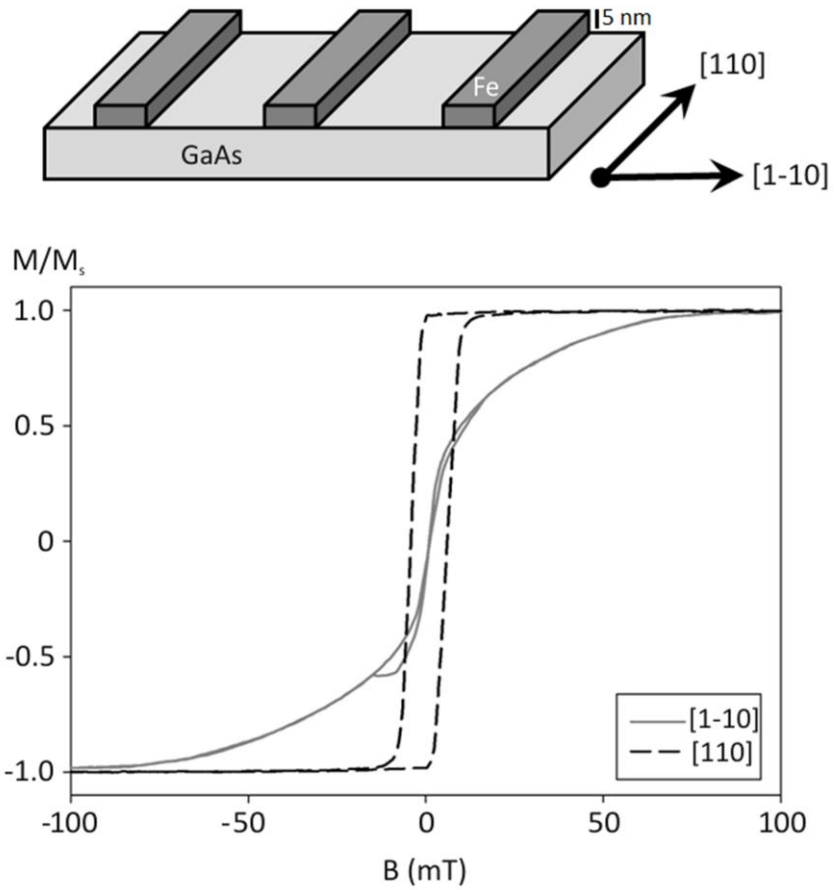

Figure 6.8 Hysteresis loop for the easy [110] and hard [1-10] axes of the Fe/GaAs(001) film, with these directions shown in relation to the device configuration.

It can be seen from the loops that the films have a strong magnetocrystalline anisotropy with the easy axis orientated along the [110] Fe direction, equivalent to the [110] direction of GaAs, and the hard axis along the [1-10] Fe direction, equivalent to the [1-10] direction of GaAs. This uniaxial anisotropy has been reported by several groups [145-147] and arises from stress anisotropy. During the first 2-3 monolayers of Fe growth the substrate surface reconstruction is disassembled and a new interface consisting of Fe, Ga and As atoms formed [148]. This introduces a compressive surface stress on the order of -3.5GPa [146]. As the film thickness increases up to 11nm the stress is dominated by a tensile component. This tensile stress arises from the diffusion of As and Ga into the Fe layer, leaving behind vacancies or substituted Fe atoms. The smaller volume gives rise to a tensile strength which is confined to a thin layer at the interface, giving rise to a strong uniaxial anisotropy. As the film thickness increases there is a competition between the interface induced uniaxial anisotropy and the bulk cubic anisotropy. If the film thickness is increased beyond ~11nm then

the stress will again become dominated by the misfit of ~1.36%, leading to a compressive strain on the order of -2.8GPa [146, 149]. For thicker films the magnetic anisotropy becomes cubic, shown in figure 6.9. This anisotropy was utilised when fabricating the contacts to ensure that the long side lies along the easy [110] direction and the short edge along the [1-10] direction.

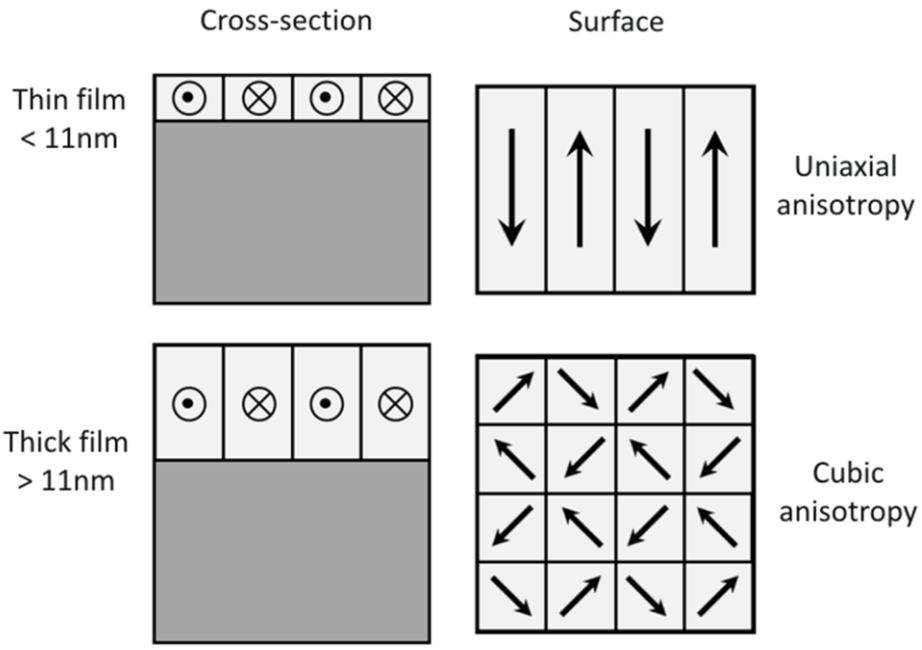

Figure 6.9 Schematic of the evolution of magnetic anisotropy with film thickness.

It can be seen from figure 6.8 that the magnetisation along the easy axis is dominated by domain nucleation. A low field is required to nucleate a domain with the strong exchange coupling allowing domains to propagate easily through the material. The magnetisation curve is highly square but there is some rounding that suggests that a small amount of domain rotation occurs at the initial magnetisation reversal process. The magnetisation curve obtained along the hard axis has no squareness and shows complex domain behaviour. This is likely to be dominated by domain wall pinning. The field required to saturate the magnetisation along the hard axis is ~8 times that required for the easy axis.

After the devices were fabricated a magnetic field was applied along the [110] direction to magnetise the Fe contacts along their easy axis. When a small field of approximately ±20mT was applied in the direction perpendicular to both [110] and [1-10] axes, the magnetocrystalline anisotropy and the shape demagnetising effect

ensure that there is no significant change in the contact magnetisation. However, a large demagnetising field can form, particularly at the corners of the contact. As the field required to nucleate a domain is very small, the strong demagnetising field will cause the Fe contact at the edges to break up into domains. This causes a reduction in the spin injection efficiency as the magnetisation will no longer be orientated along the same direction. The demagnetising field also has an effect on the Hanle measurements. In the Hanle measurements a transverse field (B_z) was applied to cause a precession of the spins. A Lorentzian function was fitted to describe the behaviour of the voltage change in the presence of the applied field, discussed in section 5.3.2. The demagnetizing field has an effect on the spin precession and subsequently on the shape of the Lorentzian function, used to extract the spin lifetimes. The effect of other fields on the shape of the Hanle curve was discussed by Dash *et al.* in reference to the inhomogeneous fields that arise due to surface roughness [150]. They showed that local magnetostatic fields affect the spin precession of electrons in the semiconductor in such a way that it leads to a broadening of the Hanle curves and subsequently a reduction in the calculated spin lifetimes, shown in figure 6.10.

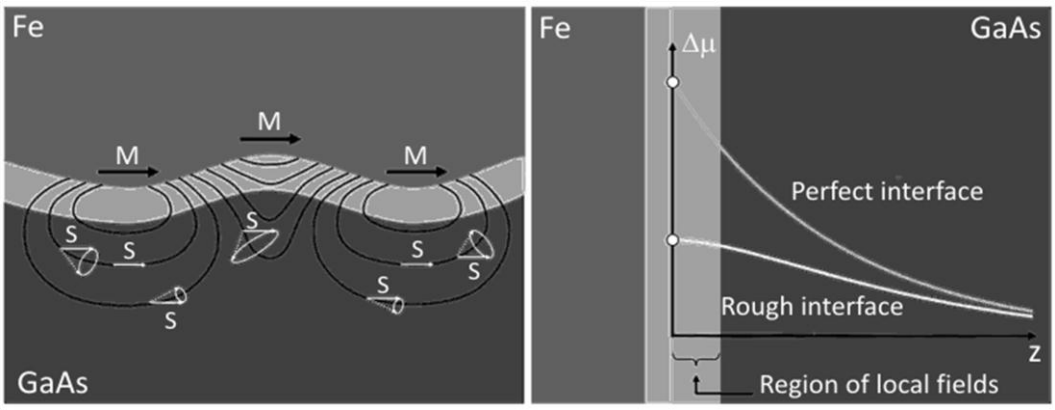

Figure 6.10 Illustration of the effect of local interface magnetic fields on the spin precession GaAs [150].

It can be seen from the figure that the magnitude of the spin accumulation is significantly reduced close to the Fe contact due to the additional fields. The demagnetizing field will have a similar effect on the spin precession to that arising from the interface roughness. There will also be a contribution to the Hanle lineshapes from the different orientations of Fe domains, formed to minimize the demagnetizing

field at the edge of the contact. An Fe domain orientated at an angle to the [110] direction will cause a reduction in the spin accumulation amplitude and also a shift in the Hanle peak, shown by Awo-Affouda *et al.* [151]. Each of these effects will cause a reduction in the extracted spin lifetimes which need to be considered when analysing the Hanle curves.

6.3 TEM analysis

6.3.1 Image simulations

Image simulations were produced using the electron microscopy software JEMS [129] employing the method discussed in section 5.4.2. Figure 6.11 shows the difference between the image simulations of the various predicted and observed interface structures [45-47, 139].

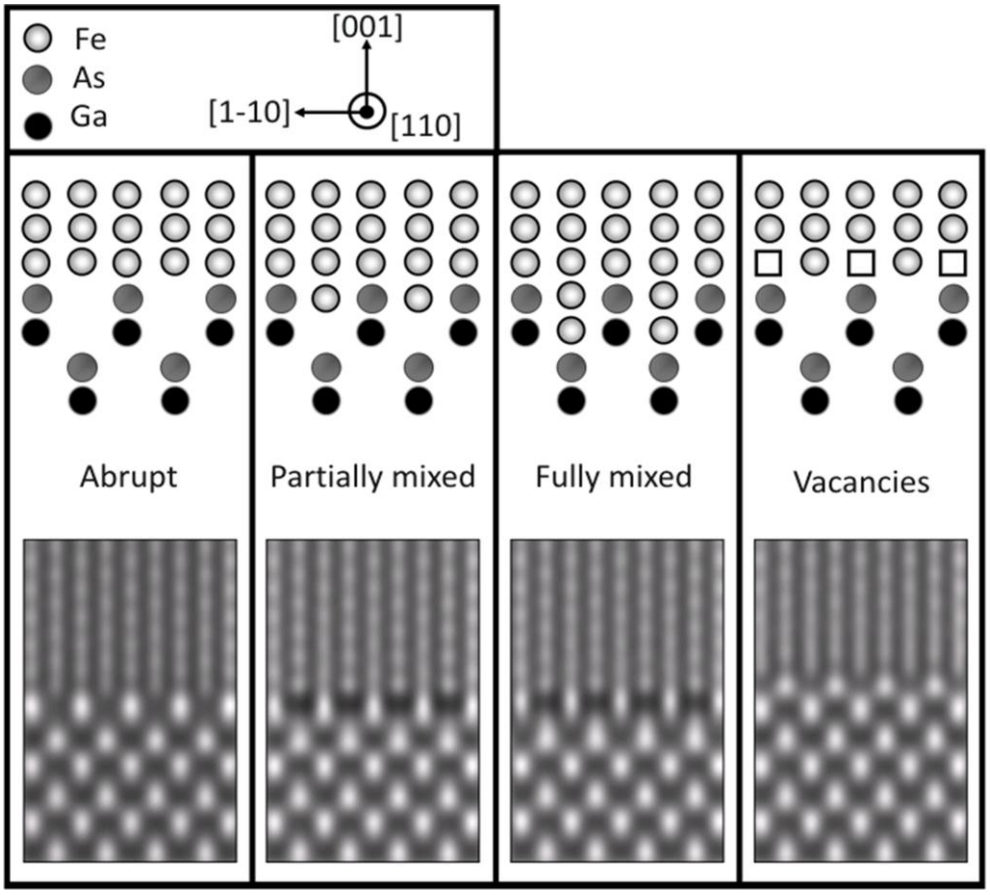

Figure 6.11 Proposed structures of the Fe/GaAs interface (top) with image simulations (bottom).

It can be seen from the figure that the there is a slight increase in the intensity at the interface for the abrupt interface for these thickness and defocus values. The introduction of a mixed layer causes a periodic reduction in the interface intensity. Both the partially mixed and fully mixed structures give similar image simulations so the level of mixing cannot be determined in Fe/GaAs(001) films. The structures can, however, be distinguished from the abrupt interface. If vacancies are introduced, giving the structure observed by Le Beau *et al.* [46], then an additional layer appears in the image simulations produced for theses values of thickness and defocus. This means that the simulations can be used to distinguish between an interface which is abrupt, contains mixing or contains vacancies. One of the main advantages of using image simulations is that they allow for large areas of the sample to be studied. As large areas of the sample are not accessible using HAADF-STEM but more easily analysed using TEM, image simulations provide a powerful technique for analysing the atomic interface structure of large areas of a sample. As discussed in section 5.4.2 the exact values of the sample thickness and defocus are not known. Simulations are therefore performed for various values of thickness and defocus and later matched to experimental images. Figure 6.12 shows a typical simulation for the abrupt interface for different thicknesses and values of defocus. These types of simulations were performed for each of the structures shown in figure 6.11 with great care taken when comparing the simulations with experimental images.

It can be seen from figure 6.12 that changing the sample thickness or the defocus level has a significant effect on the simulated images. As the thickness increases the contrast between the Fe and GaAs becomes greater. This can be seen when moving from the first column, thickness of 7.2nm, to the last column, thickness of 26.4nm. As mentioned in section 5.4.2 changing the defocus of the sample alters the contrast transfer function (CTF) leading to a different simulated image. This is clearly seen in the figure with the image simulations showing the abrupt interface both under-focus (negative defocus) and over-focus (positive defocus).

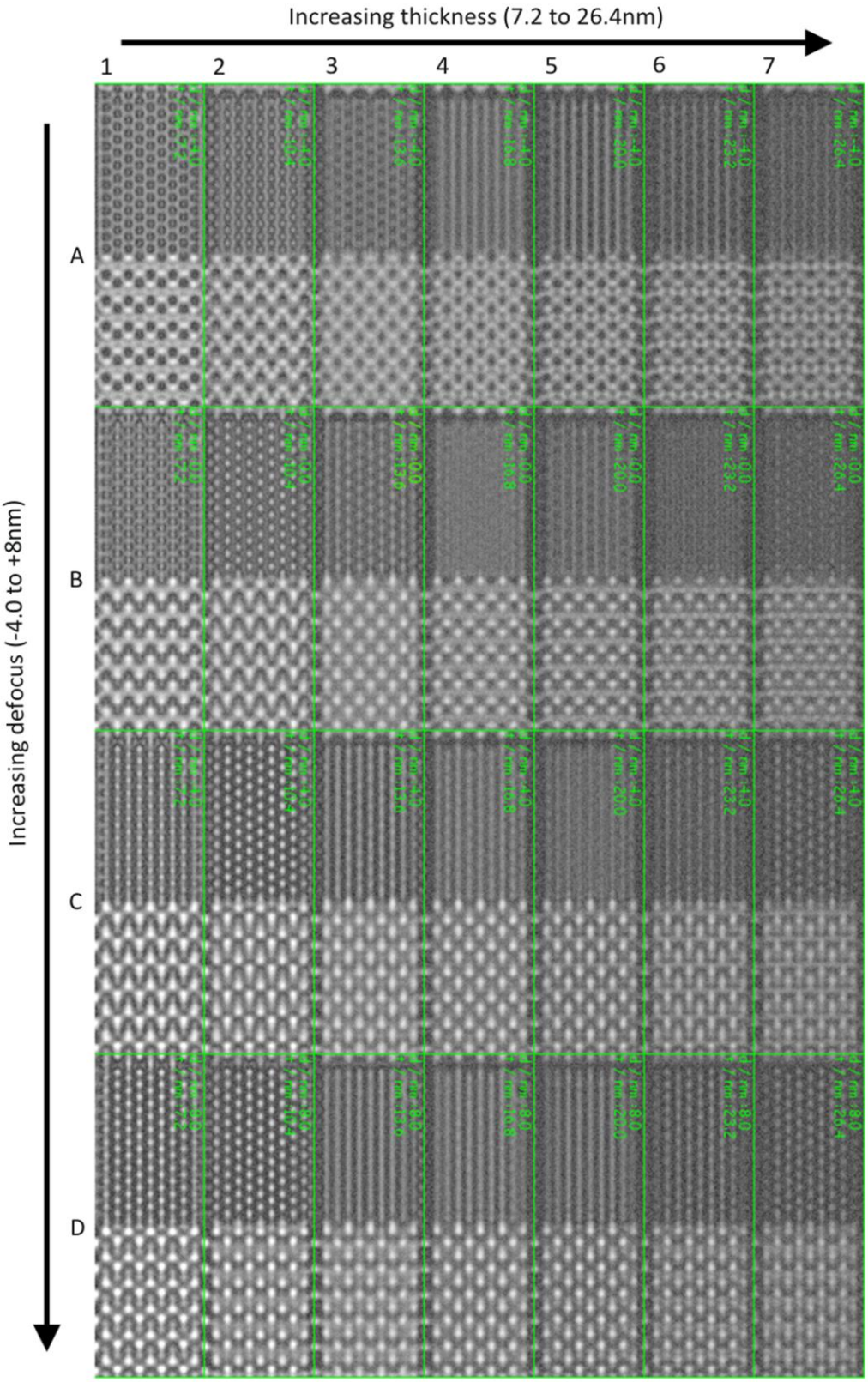

Figure 6.12 Image simulation of the abrupt interface for different thicknesses and values of defocus.

Row A is taken at a defocus value of -4nm, B in-focus, C over-focussed by +4nm and D over-focussed by +8nm. It can be seen when comparing rows A and C that the bright spots become dark and the dark bright as they are equally under/over-focussed. When working with conventional TEMs, images are often taken at the Scherzer defocus to improve the contrast. In aberration corrected microscopes the images can be taken close to in-focus due to the shape of the CTF. As mentioned, these types of simulations were performed for each of the structures shown in figure 6.11 with great care taken when comparing the simulations with experimental images.

6.3.2 Effect of annealing on the interface atomic structure

There have been numerous reports on the effect of annealing on the Schottky barrier height [143, 152] and transport properties of Fe/GaAs(001) films but TEM observations of unannealed and annealed samples have rarely been presented. Zega *et al.* [45] reported on an apparent increase in the interface abruptness for Fe/AlGaAs(001) samples but the atomic structure was not analysed [45].

Figure 6.13 shows TEM images for the sample reported in section 6.2 for both the as-deposited and annealed case, with the samples prepared using the techniques described in section 5.1.3. The as-deposited sample was imaged using a double aberration corrected JEOL JEM-2200FS TEM. The sample was then removed from the microscope and annealed in a N_2 rich environment for 10 minutes at 200°C in an annealing furnace. The sample was heated from room temperature up to 200°C in 5 minutes. The sample was then left in a N_2 rich environment to cool back down to <40°C. The annealed sample was then placed back into the microscope and re-imaged during the same day. It can be seen from figure 6.13 that annealing has a significant effect on the interface. The as-deposited film has a fairly rough interface with mixing occurring across 5-6 atomic planes. After low temperature annealing (200°C) the interface sharpness increases greatly with almost no apparent mixing. The mixing is now restricted to approximately 1-2 atomic layers. In order to ensure the areas imaged were representative of the sample, many areas were viewed over several hundred nanometres. Not all of the areas were thin enough for high resolution

imaging but the films appeared very uniform showing similar structures. This improvement in the interface structure also agrees with the previous report by Zega *et al.* [45] but this is the first time the effect has been presented using an aberration corrected microscope. This allows for the atomic interface structure to be explored.

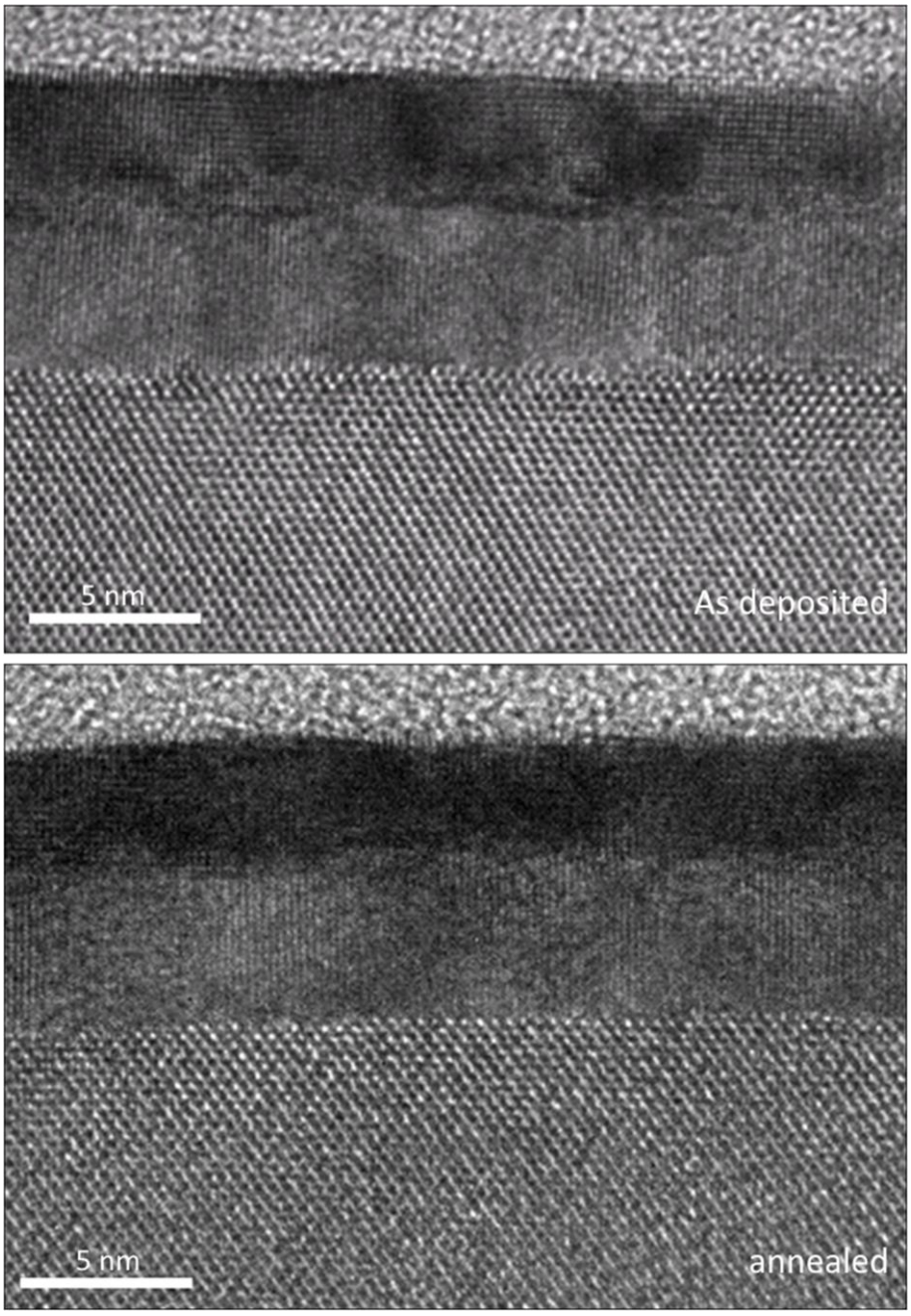

Figure 6.13 TEM images showing a) as-deposited and b) annealed Fe/GaAs film.

To explore the atomic interface structure the images were matched to simulations produced for each of the proposed structures, discussed in the previous section. Figure 6.14 shows HRTEM images for the as-deposited and annealed films

obtained in the JEOL JEM-2200FS TEM along with insets of image simulations calculated using the JEMS software. Each of the different interfaces were simulated for various values of thickness and defocus. The most suitable simulations were overlaid onto the HRTEM images to provide the best match. It can be seen from the figure that the as-deposited films are in excellent agreement with simulations for structures a-abrupt and b-mixed depending on the area analysed. Although the level of mixing cannot be determined, as the simulated images for the partially mixed and fully mixed are too similar to distinguish, this is the first time that different interface structures have been observed in the same film. This is also the first report of the abrupt Fe/GaAs(001) interface [153].

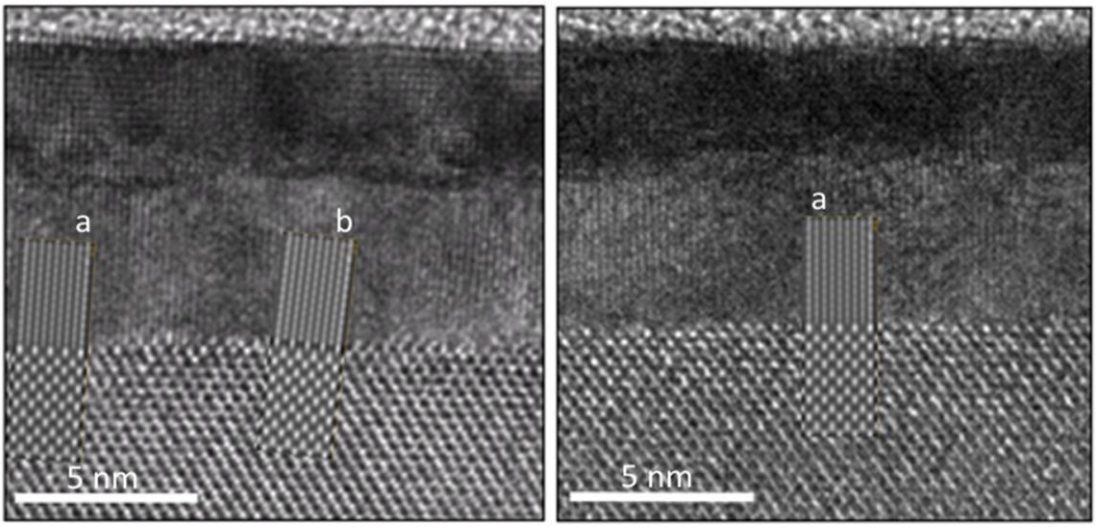

Figure 6.14 TEM images showing (left) the as-deposited and (right) post-annealed Fe/GaAs films with image simulations for a) the abrupt and b) the partially mixed structures.

From the areas imaged the as-deposited film consisted of approximately 75% the abrupt interface and 25% a mixed interface. The abrupt regions were typically 15-25nm in size whilst the mixed regions only ~5nm. It should be noted that many of the areas imaged, approximately 30%, could not be matched due to the sample thickness and contamination. After low temperature annealing the interface appears much sharper with the level of mixing reduced to just 1-2 atomic planes. Many areas were found to have excellent matching with simulations for the a-abrupt interface but there were significantly less areas that could be found that matched with the mixed interfaces. From the areas imaged the annealed film consisted of approximately 90%

abrupt and 10% mixed interfaces. This result shows that a low temperature anneal reduces the amount of mixing in Fe/GaAs(001) films.

The presence of different interface structures in the films will have a significant effect on the injection of spin-polarised electrons. As discussed in section 6.1.1 calculations suggest that the Schottky barrier height for the abrupt interface is ~0.9eV and the partially mixed interface ~0.6eV. Multiple interface structures in the same film therefore gives rise to an inhomogeneous Schottky barrier, shown in figure 6.15. As the level of mixing could not be determined, the proportion of partial mixing to full mixing is not known. The theoretical values for the Schottky barrier height for a fully mixed interface is also not known but it is expected to be below 0.6eV. Figure 6.15 shows the Schottky barriers for the as-deposited and annealed films assuming that they consisted of the partially mixed and abrupt interfaces in the proportions observed in the TEM, with the barrier heights calculated using the method of Demchenko *et al* .[47].

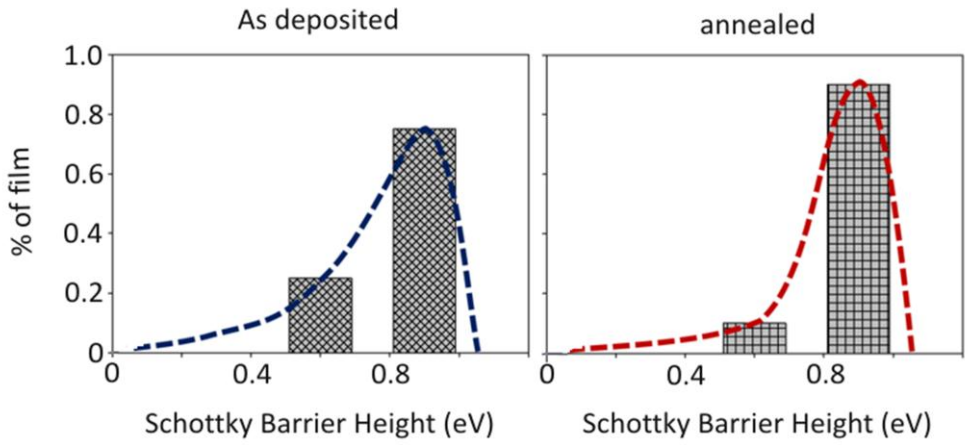

Figure 6.15 Schottky barrier distributions for the as-deposited and annealed films.

The histograms show the two barrier heights but the strain that is inside the films will cause some areas of the interface to have slightly different interatomic spacings. As the Schottky barrier height is extremely sensitive to the spacings, strain will cause either an increase or decrease in the barrier height. There is an inherent strain due to the lattice mismatch of ~1.4% but there will also be strain induced at the site of an atomic step, discussed in the next section. The films will therefore have a distribution of Schottky barrier heights with the approximate shapes shown in figure

6.15. By assuming lognormal distributions, it can be seen that the as-deposited sample will have a larger tail, with more regions where the barrier height is small, below 0.5eV, whereas the annealed film has a sharp peak around 0.9eV as it predominantly consists of an abrupt interface. Performing a low temperature anneal changes the shape of the Schottky barrier distribution. In the report by Zega *et al.* an improvement of the spin injection efficiency in Fe/GaAs spin-LED structures from 18-26% was observed [45]. Although this behaviour was attributed to an improvement in the interface structure, the mechanism to explain this phenomenon was not discussed. A change in the Schottky barrier distribution helps to explain this phenomenon as the distribution has a significant effect on the transport across the interface for several reasons. As the mixed interface has a lower barrier height [47] these regions will have a lower effective resistance and therefore a greater flow of current. These regions could act as pin-hole type areas where transport will be focused. As less energy is needed to overcome the lower barrier height, there will be a greater contribution to the transport from thermionic emission. As tunnelling is required to inject efficiently spins this will cause a reduction in the spin injection efficiency. As annealing will cause a reduction in the level of mixing, reducing the width of the barrier distribution, the number of areas where pin-hole type transport could occur will be reduced. This will cause an increase in the injection efficiency [153]. This also explains the observation of an increase in the Schottky barrier height from 0.2eV to 0.8eV after low temperature annealing [143, 144].

As well as increasing the injection efficiency by reducing pin-hole type transport and spin flip scattering from the regions with mixing, the transport will also be affected by interface resonance states (IRS). There are currently no calculation of IRS for the partially mixed interface but if strong IRS peaks are present then the transport across the interface could be dominated by these interface states. The transport could also be dominated by IRS that arise from the abrupt interface depending on the strength and location. IRS will also cause bias dependent behaviour for the transport so should be detectable experimentally. It is crucial to determine the interatomic spacings for the abrupt and partially mixed interfaces to explore the presence of any IRS and the possible effects on the transport across the barrier.

It should be noted that there are various difficulties when matching simulations to HRTEM images as the exact experimental imaging conditions are unknown. It is therefore crucial to use another technique, particularly HAADF-STEM imaging, to confirm the results.

6.4 HAADF-STEM analysis

6.4.1 Interface structure

The main advantage of HAADF-STEM is that it eliminates the need for image simulations due to z-contrast imaging. HAADF-STEM was used to image the same sample as that in section 6.3 to confirm the presence of the abrupt interface and also of different interface structures. High quality epitaxial films are clearly visible in the HAADF-STEM image shown in figure 6.16 obtained after low temperature annealing.

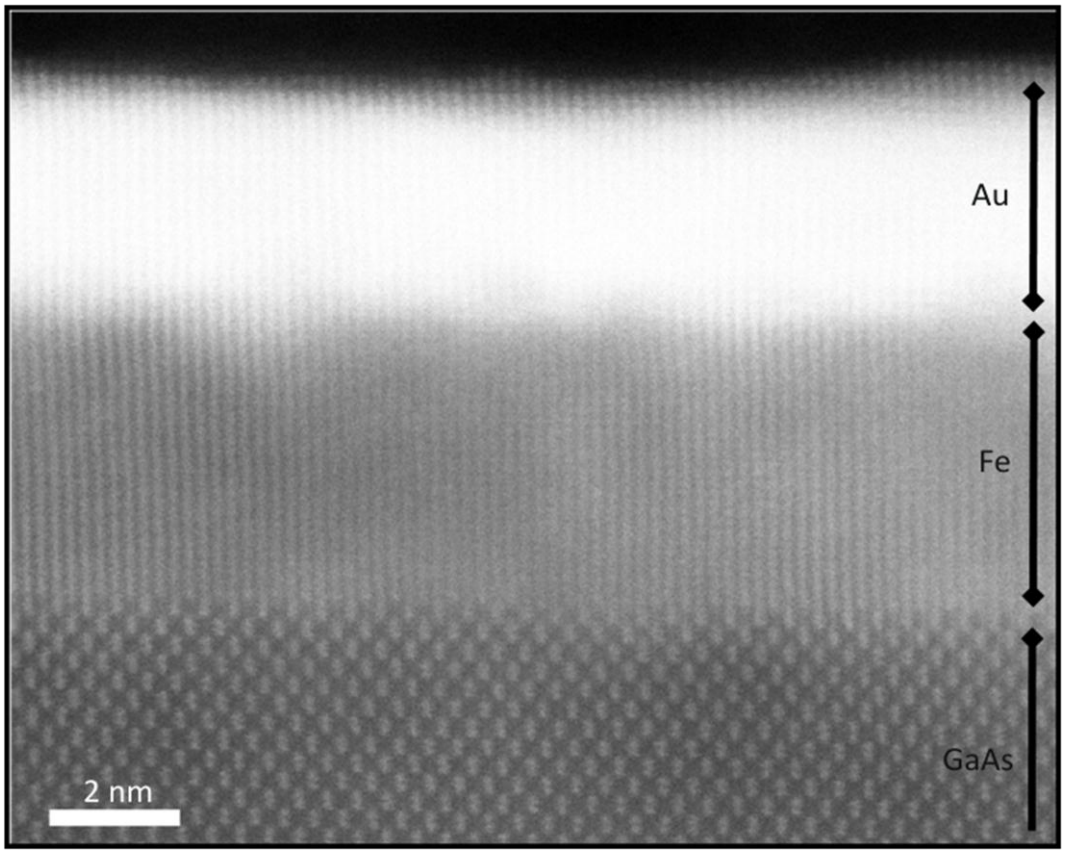

Figure 6.16 HAADF-STEM images taken along $[110]_{GaAs}$ of Au/Fe/GaAs(001) film.

It is important to note that the images are not filtered. TEM and STEM images are often filtered by applying masks onto the FFT to re-create the image after removing areas of the FFT that cause noise. These techniques can, however, introduce spurious periodicities into the image that can lead to incorrect analysis. Filtering techniques were used in both previous reports on the Fe/GaAs(001) interface by Zega *et al.* [45] and Le Beau *et al.* [46].

Higher magnification images were used to determine the atomic interface structure. It can be seen from figure 6.17 that the interface consists of two distinct structures. The majority of the interface in this film is abrupt (structure I), as expected for As-terminated surfaces. This structure has been confirmed experimentally for the first time. It can also be seen that there exists a region of the film where a partially mixed structure (structure II) is present. An advantage of HAADF-STEM over TEM is that the level of mixing can now be determined. Intensity profiles were used to determine the chemical composition of the structures. The intensity profiles obtained across the interface (indicated by the red arrows) for structures I and II are shown in figure 6.17. Mixing between the two As atoms is clearly visible in structure II. Quantitative analysis of the peak intensity shows that a $Z^{1.5}$-Z^{2} dependency. This suggests that Fe is responsible for the partial mixing, as predicted theoretically [47, 139]. It should be mentioned, however, that a random shift in the Fe at the interface could also produce a similar result. This will be addressed in the next section.

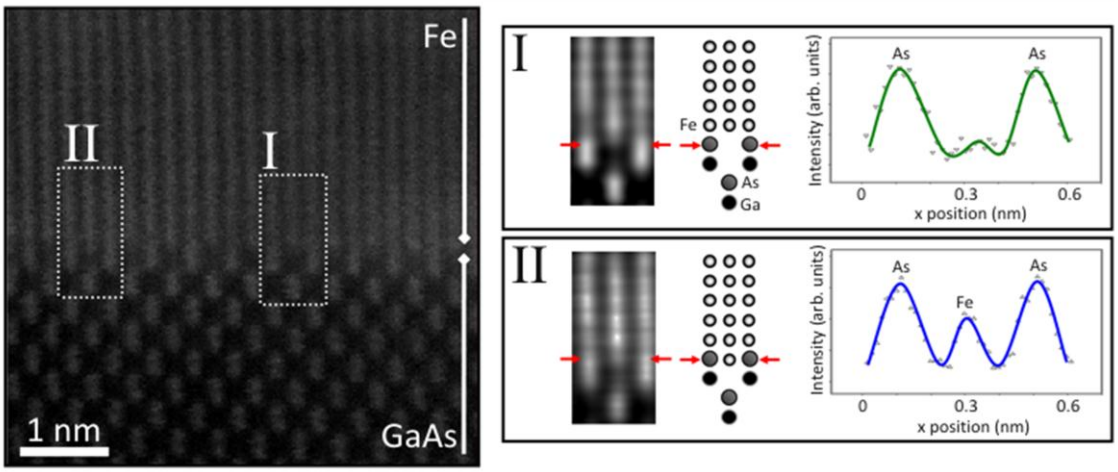

Figure 6.17 HAADF-STEM images taken along $[110]_{GaAs}$ of Fe/GaAs(001) interface with Intensity profiles for I) the abrupt and II) mixed interfaces.

This observation of a partially mixed interface is somewhat unexpected as theoretical studies suggest that this is energetically unfavourable, with the partially mixed interface having a formation energy ~0.29eV greater than the abrupt interface [47]. This is, however, the same structure as that reported by Zega *et al.* [45] in whose work mixing was observed throughout the film. It should be noted that several areas of the film were explored over approximately 50nm with almost 95% of the regions imaged showing an abrupt interface. In approximately 5% of the film partial mixing was observed. This is similar to the levels suggested using image simulations to analyse HRTEM images. Mixing was observed at the site of an atomic step in the GaAs layer, shown in figure 6.18. This suggests that strain could provide the additional energy required to form the partially mixed interface. As discussed in section 6.2.2 the films have an inherent tensile stress due to the diffusion of As and Ga into the Fe layer [146]. This stress could provide the additional energy required. At the site of an atomic step the additional stresses involved could lead to the partial mixing observed in figure 6.16. The intensity profiles across various areas of the image were used to assist in determining the proposed structure.

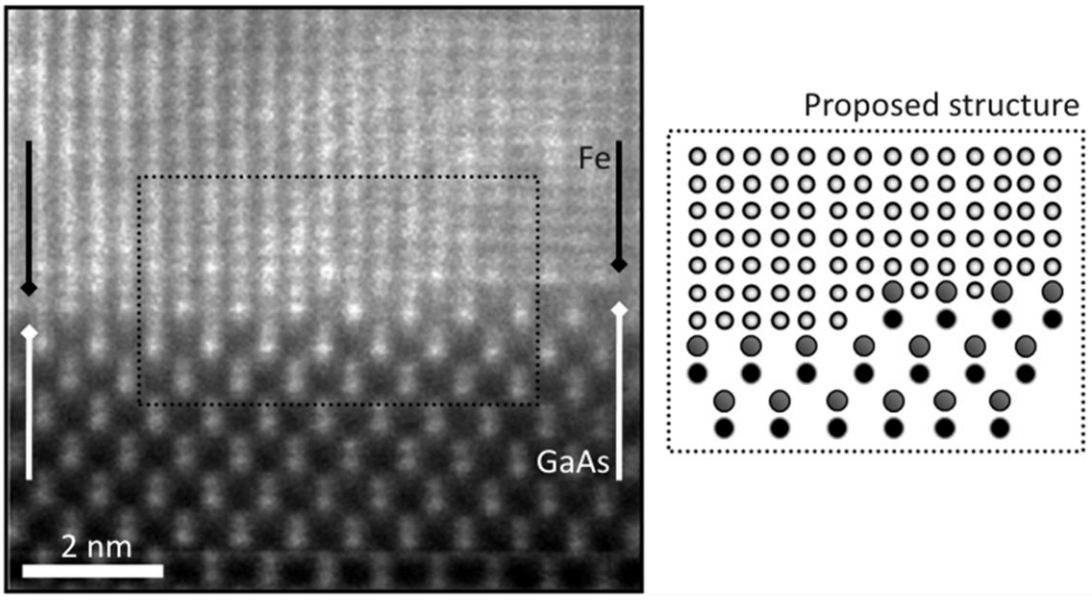

Figure 6.18 HAADF-STEM images showing an atomic step with the proposed interface structure.

This observation of different types of interfaces confirms the results obtained through analysing the HRTEM images. Image simulations were used to show that different interface structures were present in the films. The TEM data showed that annealing the films reduced the level of mixing, creating an abrupt interface. HAADF-STEM images confirm that the annealed films have a predominantly abrupt interface (~95%). The images also show that despite the low temperature anneal, small regions of the film still have some partial mixing (~5%). Multiple interface structures and strain lead to a distribution of Schottky barrier heights. Annealing reduces the level of mixing therefore changing the shape of the barrier distribution. This causes an improvement in the spin injection efficiency, observed in previous reports [45], and also the increase in barrier height reported previously [143, 144].

6.4.2 Atomic interface structure

In order to ensure that the structures observed experimentally are energetically stable, ab initio calculations were performed to calculate the total energy. These were performed by Dr. Honda from the University of Tsukuba and Prof. Inoue from Nagoya University.

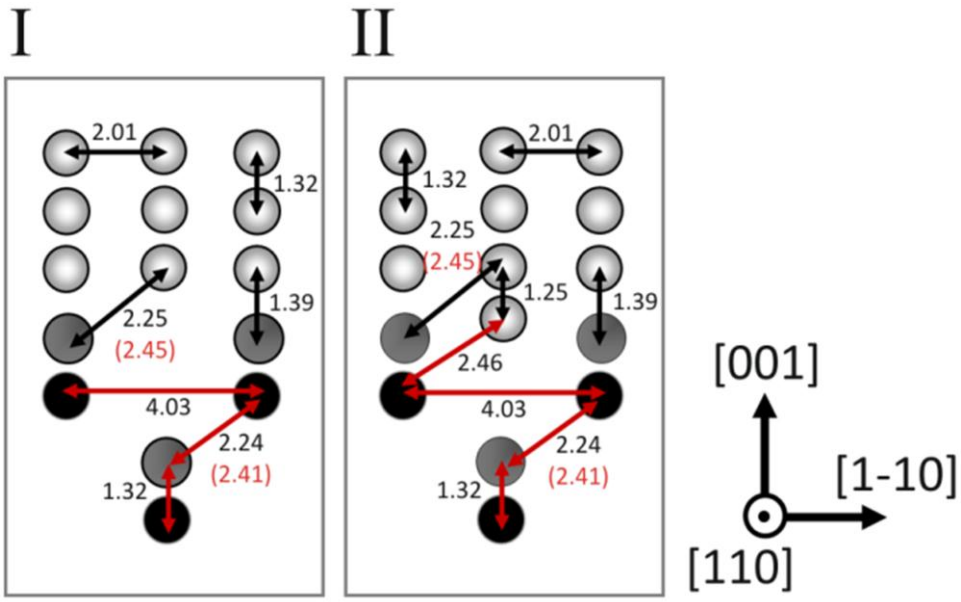

Figure 6.19 Interatomic spacings (in angstroms) for the I) abrupt and II) partially mixed interfaces. The values in brackets are only used in calculations whilst the others are the same as the experimentally values.

A supercell was created consisting of eight layers of Fe and thirty one layers of GaAs (sixteen As and fifteen Ga layers) using the interatomic spacings measured from the experimental images. Calculations were performed which allowed whole atoms within the supercell to relax. It was found that the overall relaxed structure is the same as that observed for both I-abrupt and II-partially mixed structures observed in experimental images. However, the calculated interatomic spacing did not agree perfectly with experimental values, with two spacings varying by approximately 8%. The spacings shown in figure 6.19 are those determined by considering the theoretical results, with only two of the spacings differing slightly from the initial experimental values (shown in brackets).

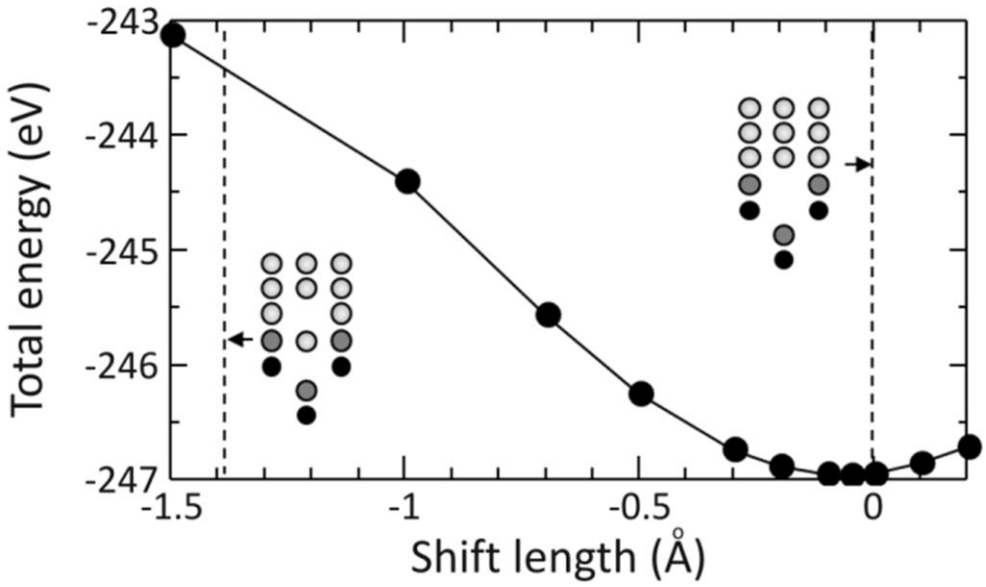

Figure 6.20 Total energy induced by the shift in the Fe atom position at the Fe/As interface. "0" represents the abrupt interface and "-1.39Å" shows the half-mixed interface.

In order to establish if the observed partially mixed structures arise from mixing of Fe and not from a shift of the interface Fe position, calculations were performed on the total energy of structures with different Fe locations. It can be seen from figure 6.20 that as the Fe is shifted towards the As layer the energy of the system increases. This result excludes the possibility of a random shift of the Fe at the interface, which could produce a similar image as the mixed interface. The abrupt interface is therefore energetically favourable and structure II is likely to arise due to interface mixing and not from a shifting of the interface Fe atom.

6.5 Interface states

Ab initio calculations were performed for the observed structures to explore the possible formation of interface resonance states (IRS). These were also performed by Dr. Honda from the University of Tsukuba and Prof. Inoue from Nagoya University. Calculated results of the local density of states (DOS) at the Γ-point, which is the most crucial for tunnelling of electrons via the Schottky barrier, are shown in figure 6.21. The local DOS (LDOS) of the As atom of the abrupt interface are shown in figure 6.21a. The LDOS of the As and Ga atoms at the partially mixed interface are shown in figures 6.21b and 6.21c, respectively. The LDOS are decomposed into s and p (p_x, p_y, and p_z) orbitals.

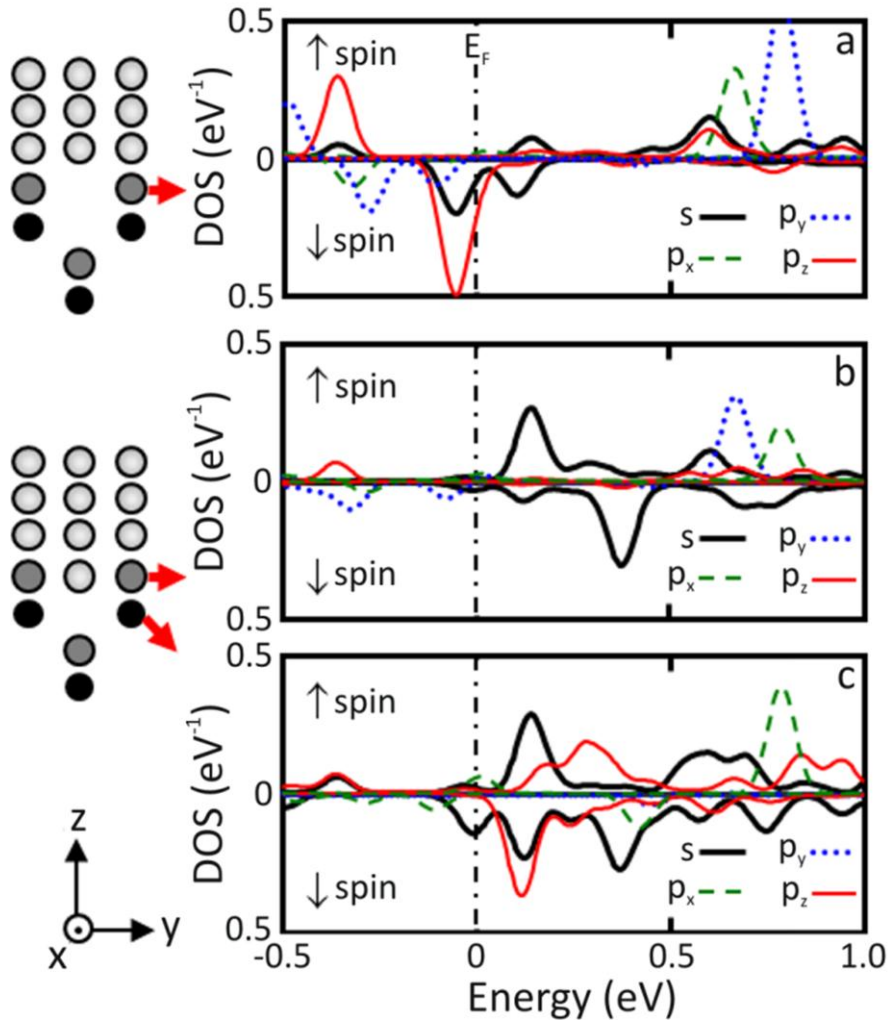

Figure 6.21 Calculated results of the Local DOS at the Γ-point for a) the As atom at the abrupt interface and of the b) As and c) Ga atoms at the partially mixed interface.

It can be seen in figure 6.21 that several peaks of the local DOS appear between the Fermi energy and bottom of the conduction band. The peak positions of the minority (↓) spin state of s and p_z components are important for the tunnelling because of symmetry matching at the interface. The peak position for the abrupt interface is at 0.09eV, and for the partially mixed interface at 0, 0.12, 0.27, and 0.43eV. The intensity of the LDOS is much larger for the partially mixed interface than for the abrupt interface. It is also noted that theoretical results have shown that the interface resonant states 0.05eV below E_F contribute the polarisation inversion under bias voltage [81]. Therefore, it may be concluded that tunnelling through interface states is more significant for the partially mixed interface than for the abrupt interface even in the low bias regime.

The results suggest that minority carrier injection may be enhanced in regions where partial mixing occurs. This means that not only are the areas of partial mixing likely to reduce the injection efficiency due to the shape of the Schottky barrier distribution, but these regions can also lead to a spin-polarised inversion from IRS. Additional calculations are required to explore the effect of the IRS on the spin injection across the interface further.

6.6 Schottky barrier distribution in Fe/GaAs(001) films

HRTEM and HAADF-STEM techniques have been used to show that multiple interface structures exist in Fe/GaAs(001) films. The films explored in this study consist of a predominantly abrupt interface, expected for As-terminated surfaces, but some areas of partially mixing were found. The presence of different interface structures gives rise to a Schottky barrier distribution. A low temperature anneal of 200°C for 10 minutes was found to reduce the level of mixing from ~30% to ~5%, subsequently changing the shape of the barrier distribution. The shape of the distribution plays a crucial role in the spin injection efficiency as the regions with partial mixing have a lower resistance, allowing a greater flow of current. This effect is enhanced by IRS as calculations suggest that minority carrier injection could occur in regions with partial mixing. As low temperature annealing reduces the level of mixing this should cause an

increase in both the effective barrier height and the spin injection efficiency. Both of these effects have been observed experimentally [45, 143, 144]. The reason that the interface structure observed in this study differs from previous studies is most likely due to the different surface reconstruction used. The effect of the surface reconstruction on the atomic interface structure is not known and needs to be explored further.

Chapter 7. Transport Properties

Electron microscopy techniques show that the Fe/GaAs(001) films consist of an abrupt interface, with partial mixing found in some small regions. Correlating the interface structure to the transport properties is crucial in these systems. This can be achieved by measurements of the magnetotransport properties of three-terminal devices using both optical and electrical techniques.

7.1 Optical measurements

7.1.1 Resonant spin amplification

As well as injecting spin-polarised electrons into GaAs electrically using Fe contacts, spins can also be excited using optical methods. It was using an all-optical set-up that Kikkawa *et al.* showed that electron spin lifetimes could be enhanced in a n^-doped GaAs 2DEG [154]. The same group demonstrated a resonant spin amplification in n^-GaAs leading to spin lifetimes of over 100ns [18]. This technique of resonance spin amplification was used to explore electron spin lifetimes in the GaAs(001) 2DEG channel of the film shown in the last chapter. The optical measurements shown in this chapter were obtained with the help of Dr. Matsuzaka and Mr Kobayashi at the RIEC at Tohoku University. A tuneable pulsed-laser with an energy linewidth of 10meV was generated using a mode-locked Ti:Sapphire laser.

Linearly-polarised light was focused onto the sample (the GaAs channel of the same Fe/GaAs(001) sample) with a spot size of approximately 1.5µm. The laser provides 50ps pump and probe pulses with 1mW and 100µW powers respectively. A conventional Voigt geometry was employed to measure the Larmor precession of the spins excited from a circularly polarised pump pulse [154]. The net electron spin causes a rotation of the linear polarisation of the probe pulse, proportional to the electron magnetic moment due to the Kerr effect. Applying an in-plane magnetic field causes the Kerr rotation signal to oscillate with a frequency proportional to both Δt and the electron g-factor. If Δt is tuned so that it is the same as the precession frequency the spin excitation is always in phase. This leads to resonant spin amplification, shown in figure 7.1 using a time delay of 50ns at a temperature of 10K.

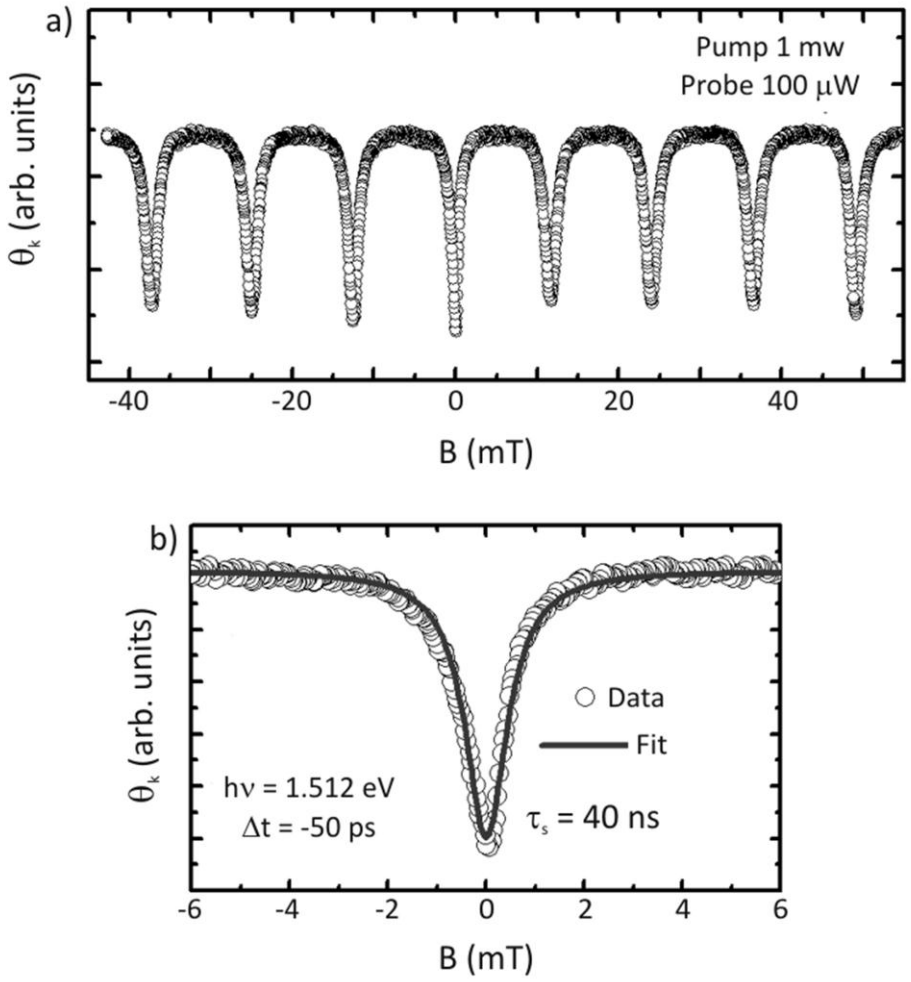

Figure 7.1 a) Resonant spin amplification signals taken at Δt=50ps at 10K for multiple oscillations and b) the central oscillation.

The time-resolved Faraday rotation describes the magnetisation *M* by the exponential decay

$$M = \mathrm{A}\exp\left(-\Delta t/T_2^*\right)\cos(g\mu_B B\Delta t/\hbar) \qquad (7.1)$$

where *A* is the amplitude of rotation, *B* the applied field, T_2^* the spin dephasing time and μ_B the Bohr magneton. This can be summed over all oscillations, with equation (7.1) modified such that Δt is replaced by $\Delta t + nt_{rep}$ where *n* is the number of oscillations and t_{rep} is the pulse repetition interval. For *n*=0, the central peak around B = 0mT, the spin lifetime is estimated to be (40±2)ns at 10K. This value is similar to those reported previously and shows that moderately doped n^-GaAs provides an environment where spin-polarised electrons can exist for several nanoseconds. This is a key requirement for the development of semiconductor spintronic devices [18].

7.1.2 Spin accumulation

Transport properties of three-terminal devices, fabricated using the techniques discussed in section 5.1, were obtained using conventional Hanle and scanning Kerr microscopy techniques described in section 5.3. Three 100µm × 10µm Fe contacts were created using Ar ion milling with a 340µm × 110µm GaAs mesa structure defined by wet etching. An insulating layer was-deposited to ensure the current travels along the Fe contact only. The devices were annealed at 200°C for 10 minutes in a Nitrogen atmosphere, the same annealing conditions used for the (S)TEM samples. Ti/Au Ohmic contacts were deposited using e-beam evaporation to create large electrical contact pads.

In order to confirm the injection of spin-polarised carriers across the Schottky barrier, a constant current was passed between two of the contacts, shown in figure 7.2. The subsequent spin accumulation created next to the central contact was detected using the Kerr effect described in section 5.3. Before passing the current between the contacts a large field (B_x) of ±2.2T was applied to magnetise the Fe along the (110) direction. Linearly-polarised light from the laser was scanned along the (1-

10) direction. Scanning between the central and end contact (not used to pass the current) allows the diffusion of spin-polarised carriers to be measured. Scanning between the two contacts used to pass the current detects the contributions to the transport from both diffusion and drift.

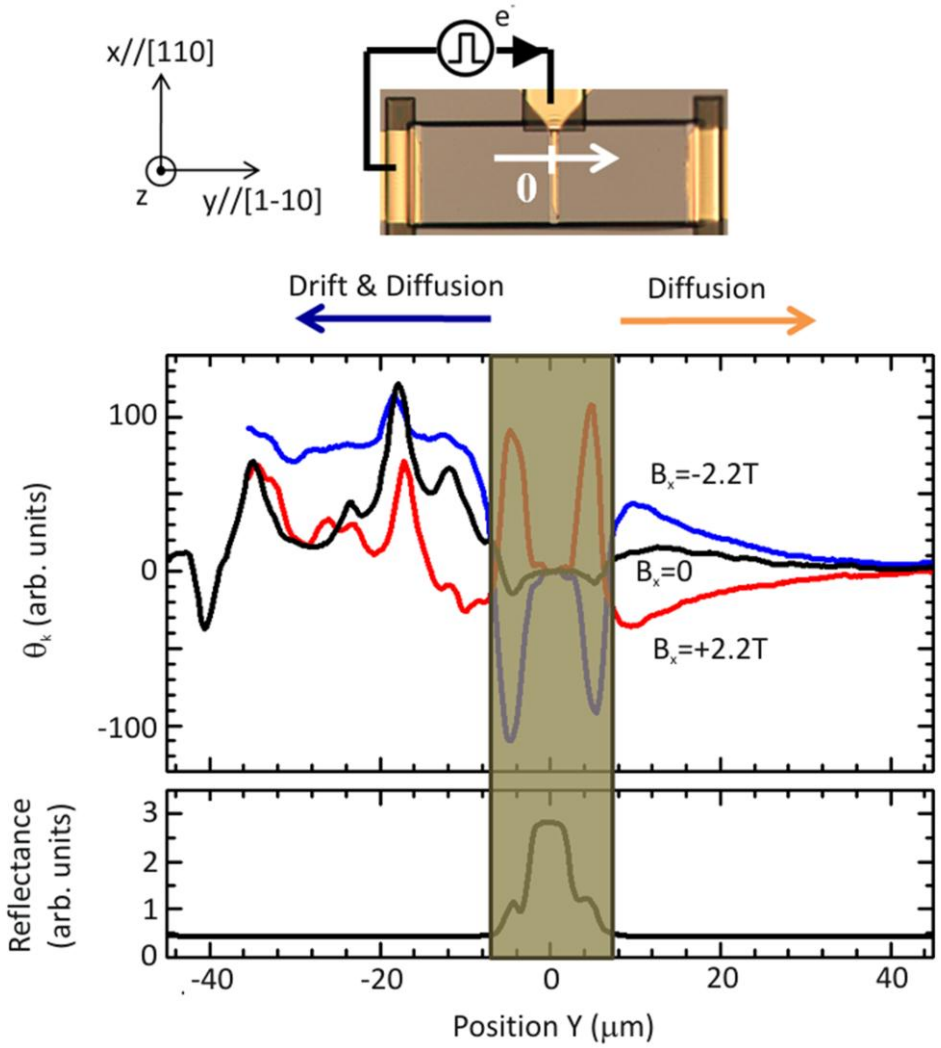

Figure 7.2 Kerr rotation signal at 10K as a function of position for V_{bias}= -0.3V, corresponding to a current density of 25A/cm^2. Y=0 defined as the mid-point of the peak in the reflectance signal.

Figure 7.2 shows the signals obtained for both the Kerr rotation and reflectance at 10K. The reflectance signal shows clearly the position of the Fe contact, represented by the shaded region. Focusing first on the signal arising from diffusion, the effect of the initial field B_x can be seen clearly. If the contact is not initialized (B_x=0) the Fe contact contains many domains, as discussed in section 2.1, so only a very small net spin accumulation was detected. When the contact was magnetised along (110) direction clear signals arising from spin accumulation can be seen. The spin accumulation follows a characteristic exponential decay up to a distance of

approximately 50µm. From the figure it can be seen that the signal starts to decay above Y > 12µm. This is most likely due to the shape of the Fe contact. Using Argon ion milling to etch away the Fe film, leaving the contacts, does not create a perfectly abrupt contact edge. From the reflectance signal it can be seen that the contacts have ~5µm roughness at the edges. The shape of the edge leads to a reduced signal with a few microns of the contact and also the strange shape of the reflectance signal observed near Y = 5µm. It can also be seen that the signal arising from drift and diffusion does not follow an exponential decay and also appears very noisy. It should be noted that the large peak in the signal that occurs around -20µm from the contact appears in all three signals.

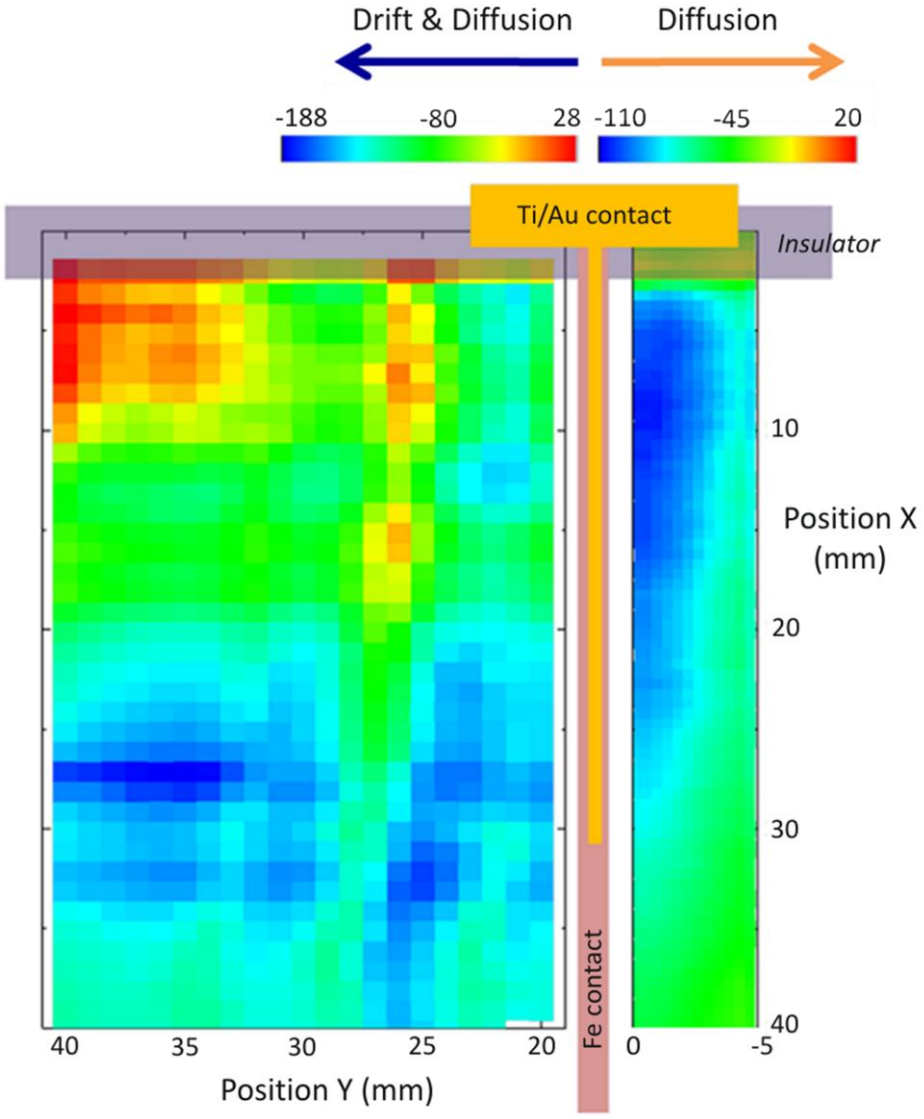

Figure 7.3 Scanning Kerr microscopy signal obtained as a function of position from the edge of the central contact (Y=0). The measurement was taken at 10K for a bias voltage of -0.3V, corresponding to a current of -500µA, after applying an initial field of -2.2T.

In order to explore the origin of the peaks in the drift signal a scan was performed using a piezoelectric-stage to detect the Kerr rotation signal as a function of position from the edge of (X-direction) and along the (Y direction) GaAs channel, shown in figure 7.3. It can be seen from the figure that the signal arising due to diffusion is largest where the current density is the greatest, close to the Ti/Au contact. The signal strength then decreases with the expected exponential decay along the GaAs channel (Y direction). The current flow through drift and diffusion appears very non-uniform. This is probably due to defects in GaAs which cause the current flow to be inhomogeneous. This would explain the reproducible noise peaks observed in figure 7.2 for this sample. In order to explore this phenomenon further the signal was obtained for different bias voltages, shown in figure 7.4

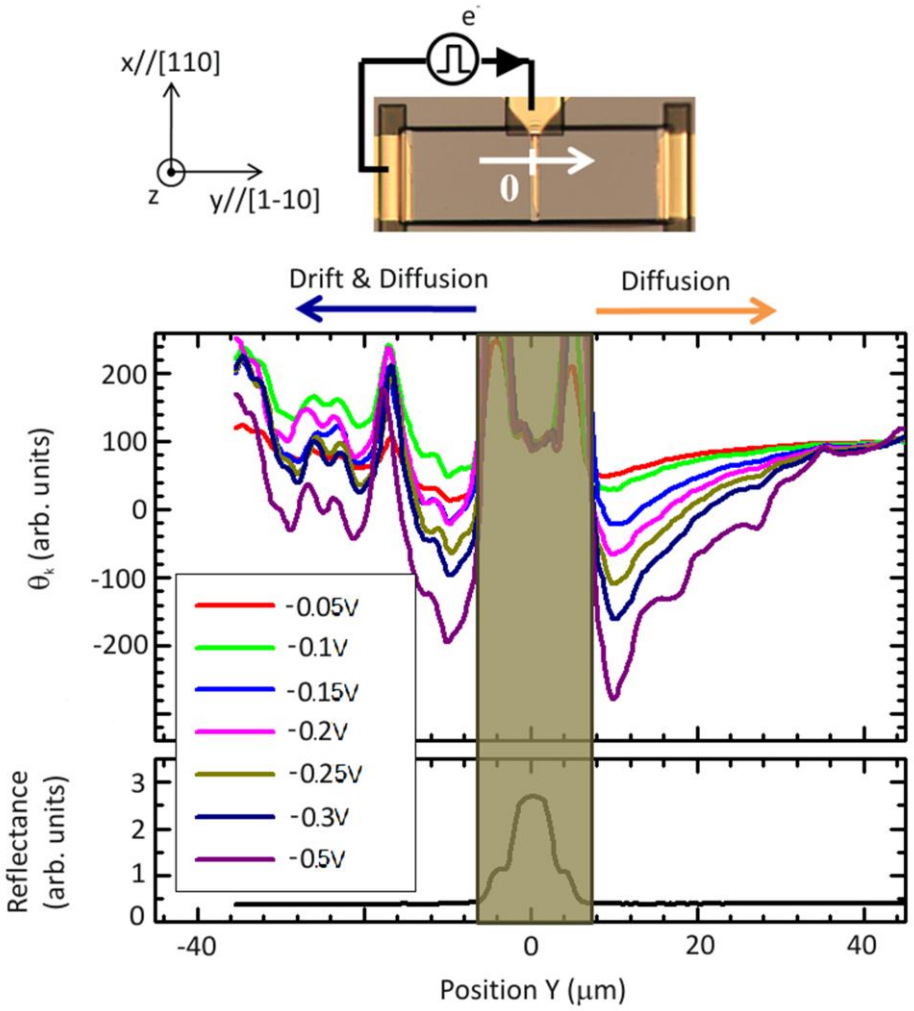

Figure 7.4 Kerr rotation signal as a function of position and bias from V_{bias}= -0.05V up to 0.5V. The data was obtained at 10K with Y=0 defined as the mid-point of the peak in the reflectance with a field of +2.2T used to initialized the contacts.

It can be seen from the figure that the locations of the peaks do not change with bias voltage, only the magnitude which increases with the applied bias. This again suggests that the effect is due to physical defects in the GaAs channel. One experiment that could be done in the future to help determine the origin of peaks in the drift and diffusion side would be to switch from using the left and central contacts to pass the current to using the central and right contacts. One could also run in the experiment in reverse bias to see if the phenomenon is again observed. These experiments were not performed during this study due time and equipment restrictions.

7.1.3 Local Hanle curves

To confirm that the signals detected are due to spin accumulations, local Hanle measurements were made. The contacts were first magnetized along the x-direction then a small field (B_y) was applied along the y-direction. The field B_y causes a change in the z-component of the spins, detected using the Kerr effect. A small field leads to an increase in the Kerr rotation as the z-component of the spin is increased but the application of a large field causes a reduction in the z-component as the spins align along the y-direction. The shape of the local Hanle curves obtained for the same device measured in the previous section can be seen in figure 7.5, measured 15µm from the edge of the central contact.

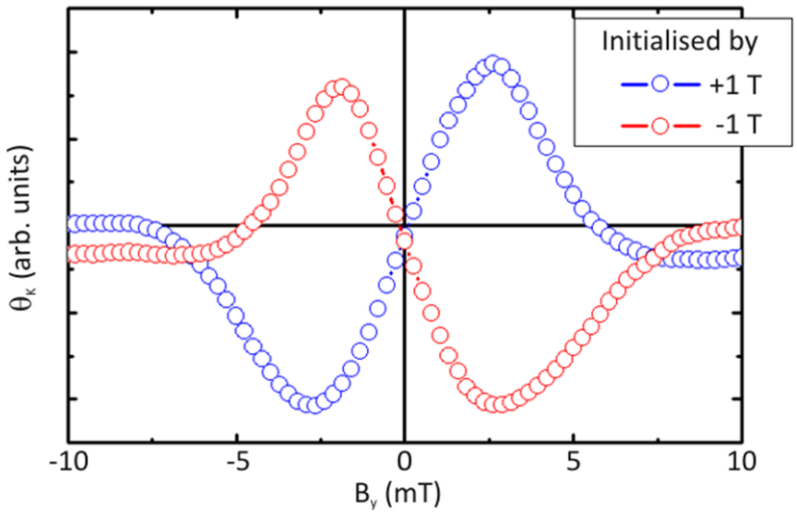

Figure 7.5 Local Hanle curves 15µm from the central contact using an initialisation field of ±1T.

In this figure the effect of magnetizing the contacting along the ± x- direction can be seen, with a clear sign change visible in the Kerr rotation signal. This signal was measured 15µm from the edge of the injector contact (Y=30 µm) with a bias of -1V, corresponding to a current density of 80A/cm^2, applied at 10K.

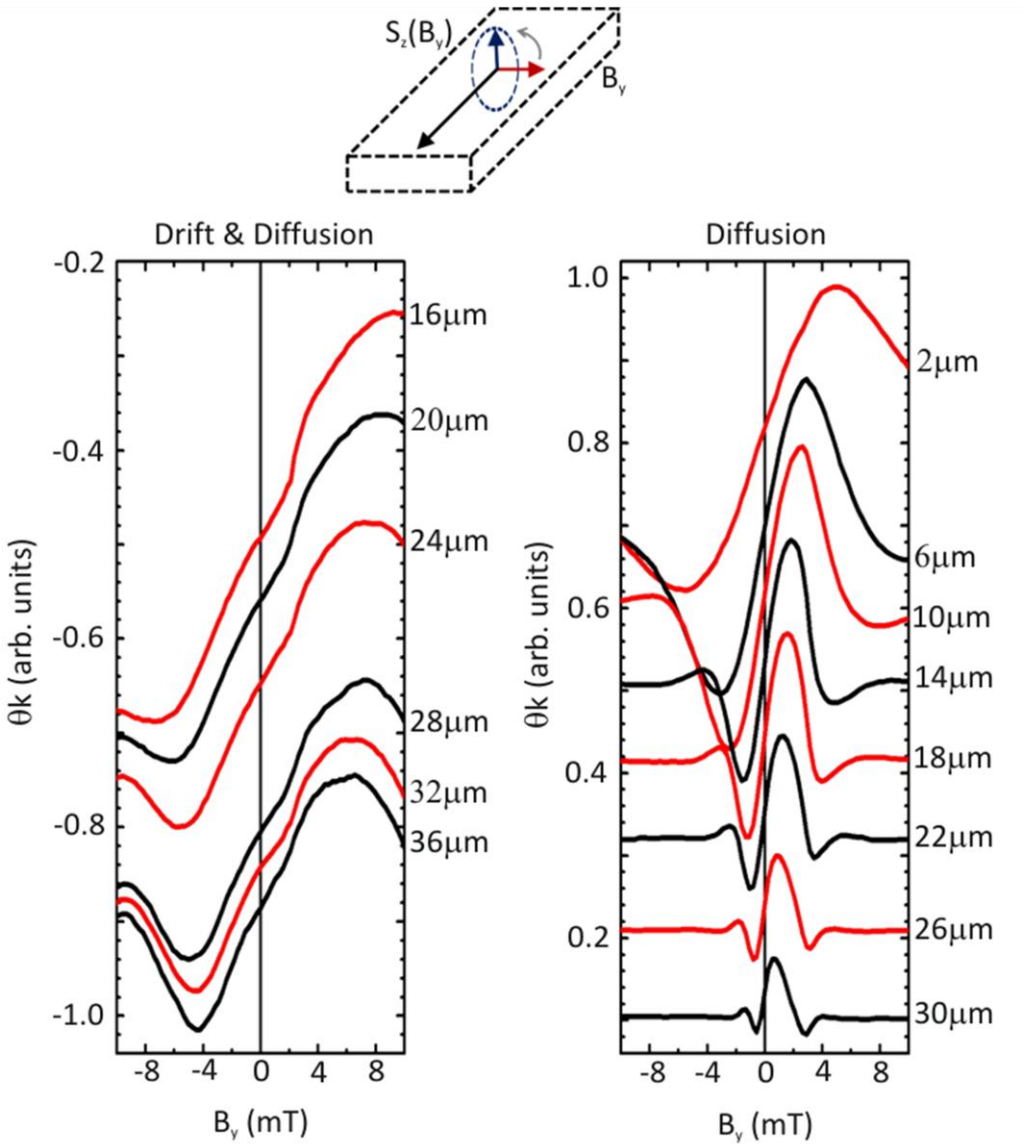

Figure 7.6 Local Hanle curves obtained at 10K at a distance of 36µm from the injector.

Figure 7.6 shows local Hanle curves taken as a function of position along the GaAs channel, measured from the edge of the central contact, at 10K with a bias of -1V applied. The curves were obtained up to a distance of 36µm from the central contact. It can be seen from the figure that signals were obtained from the both left and right of the injector contact. The signal from the right arises from diffusion

whereas that from the left has contributions from both drift and diffusion. The signals from the drift and diffusion side appear quite less smooth which may be due to the same effect causing the peaks in figure 7.2, attributed to an inhomogeneous current flow due to defects. The signals arising from diffusion appear very smooth with the amplitude decreasing the further away from the contact the measurement was made. The signal also appears more asymmetric as the distance from the contact increases. This effect has been observed previously and is due to the spin-Hall effect [155]. As the spin current travels along the GaAs channel it experiences asymmetric scattering through side jump and skew scattering mechanisms [156]. These mechanisms cause the two, up- and down-, spin currents to be scattered in opposite directions. As the two spin currents themselves flow in opposite directions the spins are scattering to the same edge of the GaAs channel. The further away from the central contact the measurement was taken the greater the amount of scattering that had occurred. This lead to the asymmetry in the local Hanle curves observed.

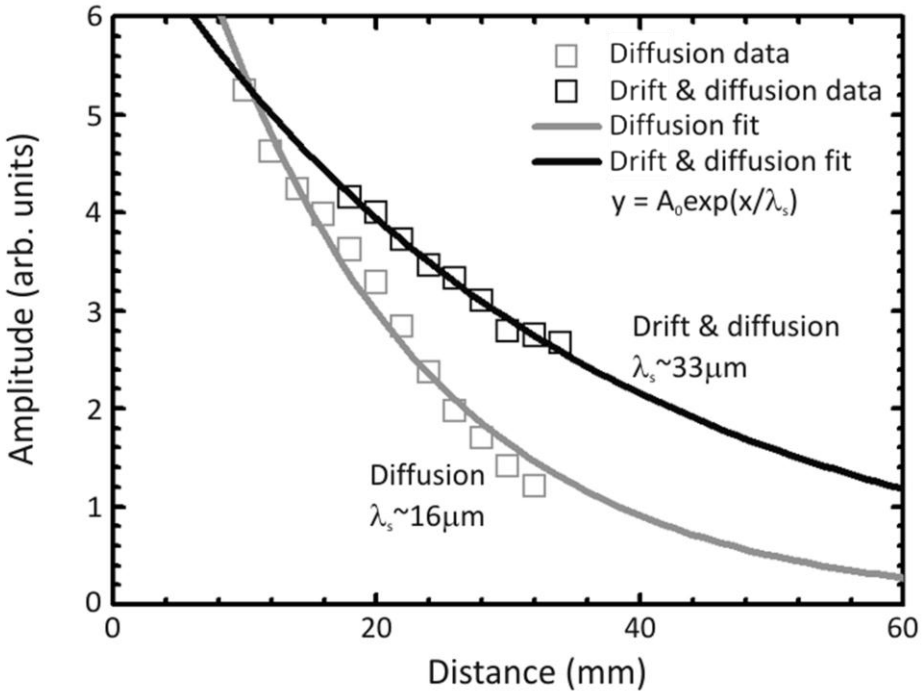

Figure 7.7 Spin diffusion length obtained from the decay of the local Hanle curve amplitude. V_{bias}=-1V, corresponding to a current density of 80A/cm2, measured at 10K.

In order to determine the spin diffusion length, the amplitude of the local Hanle peaks was plotted as a function of distance from the central contact. Figure 7.7 shows the exponential decay of the signal strength as a function of position. From the curves,

the spin diffusion length was estimated to be (16±1)µm and the drift-diffusion length to be (33±1)µm. The spin diffusion length of ~16µm means that the spin accumulation will completely decay before reaching the outermost contact, situated over 100µm away. This is crucial as the electrical measurements require the spins to decay so the electrochemical potential difference underneath the contacts could be measured.

7.2 Electrical properties

7.2.1 Current-voltage curves

As the injection of spin-polarised carriers has been confirmed using optical techniques, electrical measurements were explored to characterise the devices further. As discussed in chapter 3, there are several transport mechanisms that can occur across the Fe/GaAs interface, with tunnelling expected to dominate in such highly doped semiconductors. As discussed in section 3.2.2 the exact contribution to the transport from each of the mechanisms is not known. Furthermore, in the last chapter it was shown that although the films consist of a predominantly abrupt interface, there are regions where partial mixing occurs. This leads to a distribution of Schottky barrier properties.

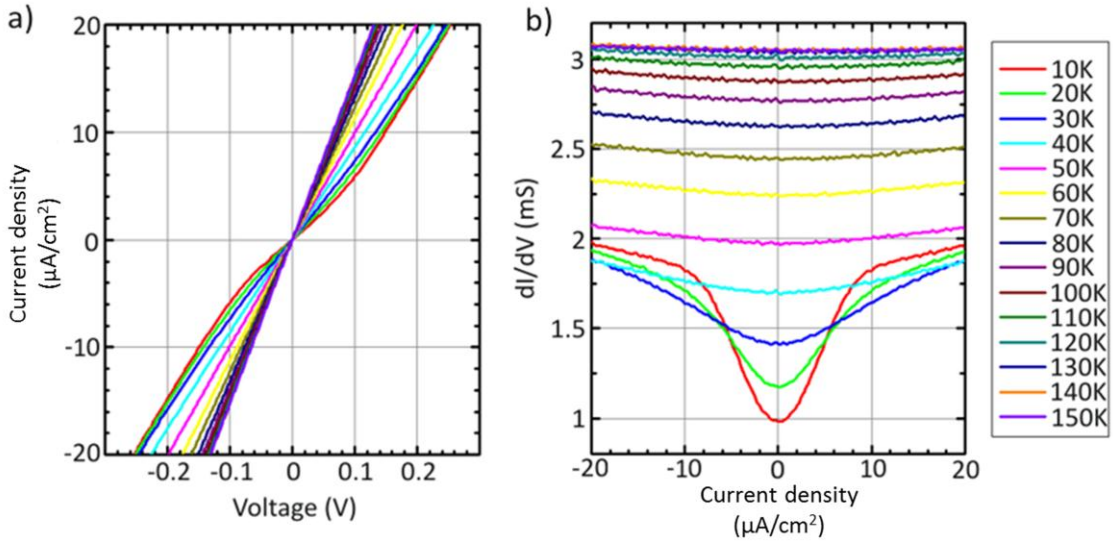

Figure 7.8 Current-voltage curves and conductance curves obtained from 10-150K.

As the conventional models used to analyse Schottky barriers do not take this into account, the Schottky barrier properties cannot accurately be predicted from the current-voltage (*I*-*V*) curves. If the BDR model, discussed in section 3.2.2 (equations 3.13a-d), is used an asymmetric Schottky barrier with potentials 0.33±0.5eV and 0.08±0.2eV is estimated with a barrier thickness of 16Å. This model assumes that single-step tunneling, so no transport through interface states, is the only transport mechanism. This barrier is similar to those measured in previous reports [143, 144] but it should be noted that this model does not take into account image force lowering or the effects discussed above.

It can also be seen from the conductance curves that a zero-bias anomaly exists, suggesting that tunnelling is the dominant transport mechanism, as expected. It should also be noted that the symmetry of the I-V curves is due to the measurements set-up as 2 contacts are used, one forward bias and one reverse biased.

7.2.2 Hanle curves

It was shown in section 7.13 that the spin accumulation created in the GaAs channel decays long before reaching the detector contact, as shown in figure 5.10 of chapter 5. The conventional Hanle set-up discussed in section 5.3 can therefore be used to explore the spin transport in the devices. Figure 7.9 shows the Hanle peaks obtained at 30K for both forward (+300μA) and reverse bias (-300μA). It can be seen from the figure that a quadratic fit is subtracted from the signal before fitting the Lorentzian function. The origin of the quadratic behaviour is from magnetoresistance and Hall effects in the semiconducting channel. This was confirmed through the measurement of a control sample. A test sample of the same dimensions was fabricated using a non-magnetic Ti/Au Schottky contact. The measurements showed no peaks, as expected due to the non-magnetic contacts, but a quadratic dependence of the voltage confirming that this arises from the semiconductor channel.

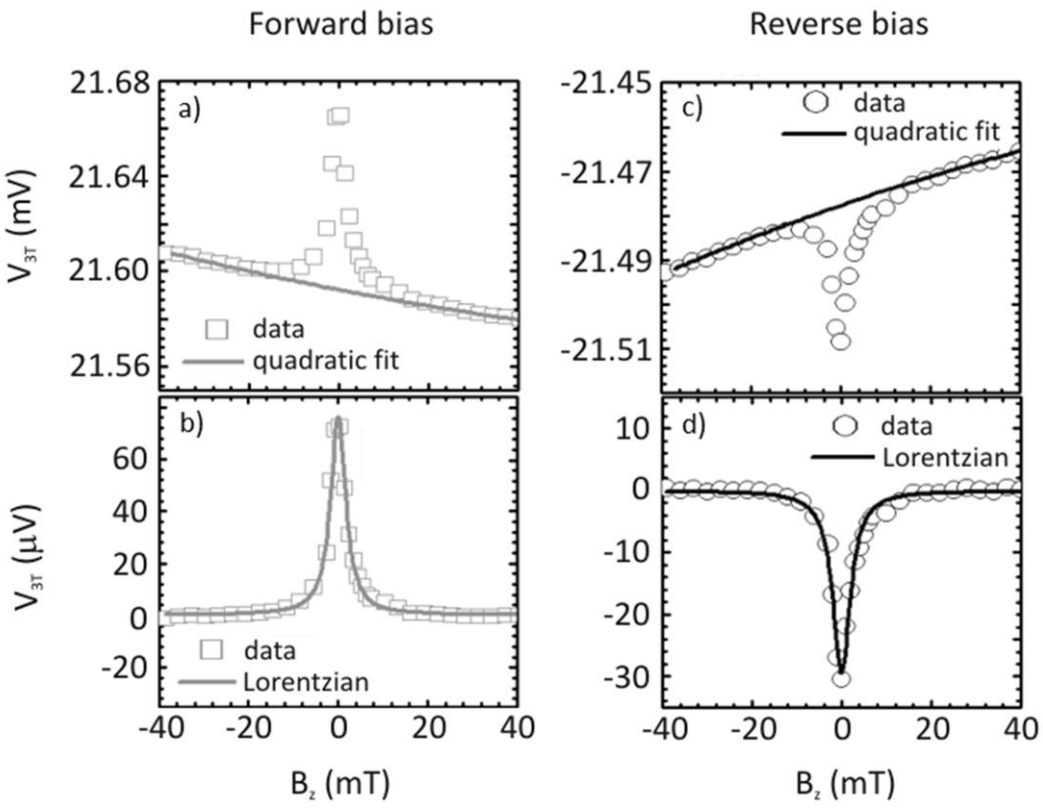

Figure 7.9 (a & c) Raw and (b & d) corrected Hanle curves for (a & b) forward and (c & d) reverse bias (±300μA) obtained at 30K.

From fitting equation 5.1 the spin lifetimes inside the semiconductor were calculated to be (13±1)ns for forward bias and (11±1)ns for reverse bias. The difference in the spin lifetimes is due to the shape of the Hanle curves. It can be seen from figure 7.9 that there is a much larger signal observed for forward bias than reverse. The temperatures at which this asymmetry occurs suggests that this is due to dynamic nuclear polarisation, discussed in section 4.3.4, often observed at temperatures below 60K. To explore further this possibility and to understand the transport properties, Hanle curves were measured from 5K up to room temperature.

Figure 7.10 shows Hanle curves measured at a selection of temperatures from 10K to 110K for both forward and reverse bias (±300μA). It can be seen that the Hanle effect is almost undetectable at 110K and could no longer be seen after 120K. This is a similar temperature as measured by other groups but is well below room temperature, required for the development of future devices. It should also be noted that the signals appear much larger in amplitude for forward bias than reverse bias but

only for values below approximately 60K as can be seen from figure 7.11. This suggests that dynamic nuclear polarisation could be contributing to the difference in signal. Another possibility is that the decay of the spin signal through the depletion region at the interface is temperature dependent and different for spin-up and spin-down carriers. In section 3.3.2 the model proposed by Smith and Ruden [82] was introduced which describes a difference in the spin decay rates as electrons tunnel through the barrier. If a bias dependence is introduced then this helps to explain the polarisation inversion. If a temperature dependent scattering rate is introduced then this could also reproduce the observed signal asymmetry.

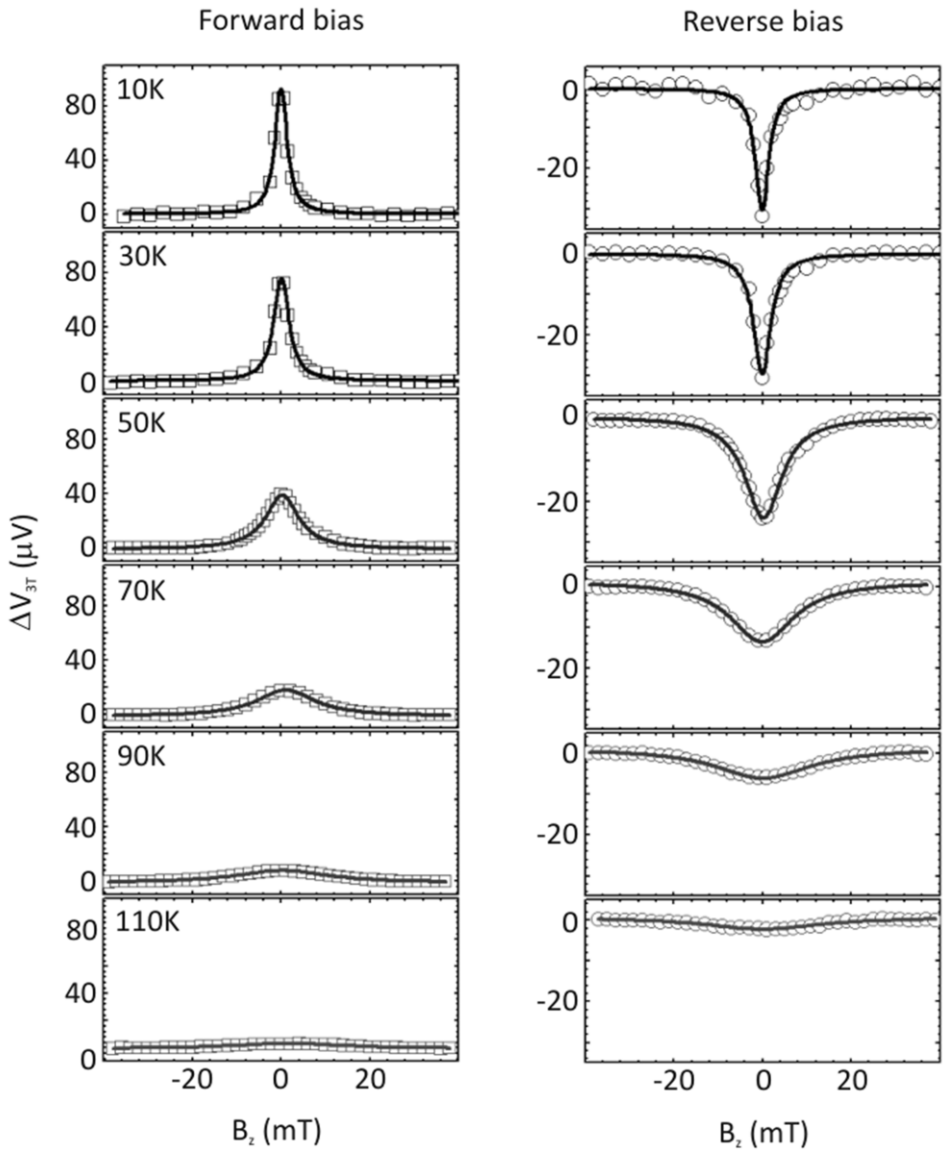

Figure 7.10 Hanle curves obtained from 10-110K for forward and reverse bias (±300μA) for Fe/GaAs(001).

A summary of the amplitude of the Hanle curves and the extracted spin lifetimes can be seen in figure 7.11. The spin lifetimes were calculated to be approximately (6±1)ns at 50K and up to (15±1)ns at 10K. The signal asymmetry is also clearly seen below 60K. The spin life at 10K can be correlated with the spin diffusion length, measured optically, to ensure that the two different techniques provide similar values. If this electron spin diffusion length in GaAs is assumed to be $10cm^2s^{-1}$ [157] then the spin diffusion length is estimated to be ~4µm. The value measured optically was ~16µm but this was obtained using a current density 5 times greater than that that used in the electrical experiments. It should also be noted that the recent work has shown how the value of $10cm^2s^{-1}$ may not be suitable for this set-up [158]. Taking these considerations into account the two different experimental techniques agree well with each other and show how large spin lifetimes and spin diffusion lengths can be observed in this system.

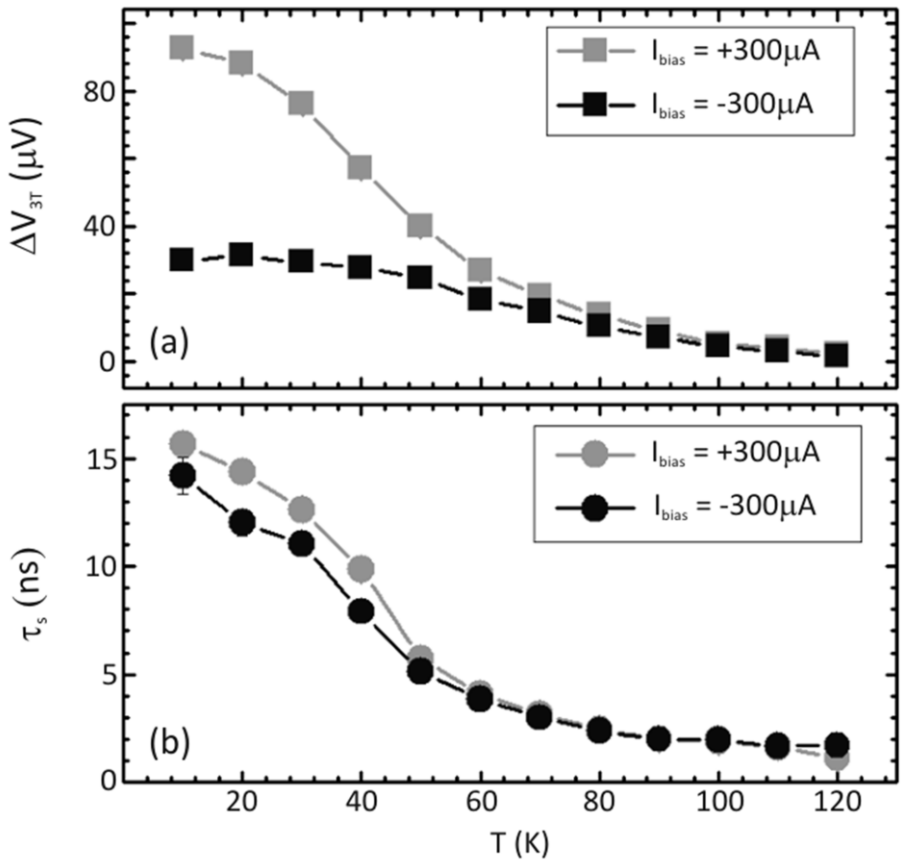

Figure 7.11 (a) Amplitude and (b) spin lifetimes extracted from the Hanle curves from 10-120K.

It can also be seen that the behaviour of both curves starts to change below 20K. This could be due to a number of effects. The first possibility is that this arises from a temperature dependent spin-scattering rate as the electrons tunnel through the barrier. Another possibility arises from the distribution of Schottky barrier heights, mentioned in the last chapter, which arises from the different interface structures. Changing the temperature alters the electron energy distribution. This effects how the electrons will travel across the Schottky barrier distribution. At high temperatures their will exist electrons which travel through thermionic emission over the regions with a low barrier height, where partial mixing occurs, whilst other electrons will tunnel through regions with a higher barrier height. As the temperature is reduced the electrons will no longer have enough energy to travel by thermionic emission across the regions with partial mixing. As the calculations in section 6.5 suggest that interface resonance states (IRS) exist for the partially mixed interface, minority spin injection could occur in these regions thereby reducing the overall amplitude of the Hanle curves. In order to confirm which effect is responsible for the reduction, films with different Schottky barrier distributions need to be created. How to achieve this will be discussed in chapter 9. Further calculations are also required to understand the effect of IRS in these systems.

7.2.3 Bias dependence

As discussed in Chapter 3 one of the greatest problems with Fe/GaAs(001) films is irreproducible device behaviour. Lou et al. showed that devices grown from the same epilayer exhibit a bias dependent polarisation inversion for either forward or reverse bias in a non-reproducible manner [44]. The Hanle curves for different bias voltages can be seen in figure 7.12, and are summarized in figure 7.13. It can be seen from the figures that no change in the sign of the spin polarisation and the associated peak or dip was observed for either forward or reverse bias. The range of biases applied corresponds to an internal voltage range between -0.15 and +0.15 volts. These measurements were all taken at 50K to reduce the effect of dynamic nuclear polarisation, discussed in the last section.

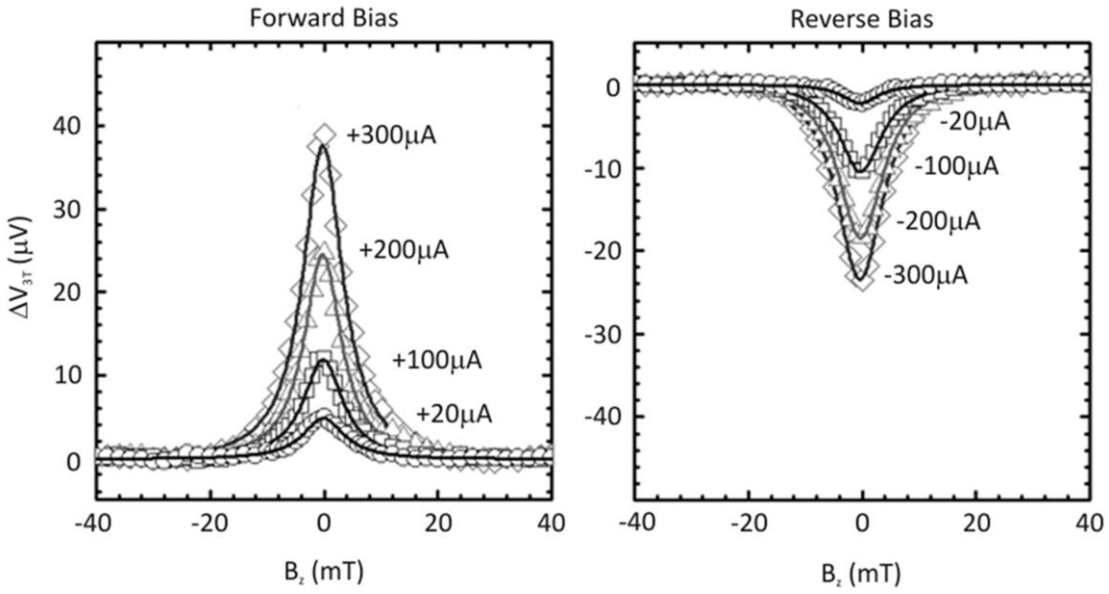

Figure 7.12 Bias dependence of the Hanle curves obtained at 50K.

However, it can be seen from the figures that there is a small difference in the amplitude between forward and reverse bias. The devices do appear very well behaved. As the bias is increased the amplitude increases. The spin lifetimes were found to be almost independent of the bias and measured to be approximately 5-6ns.

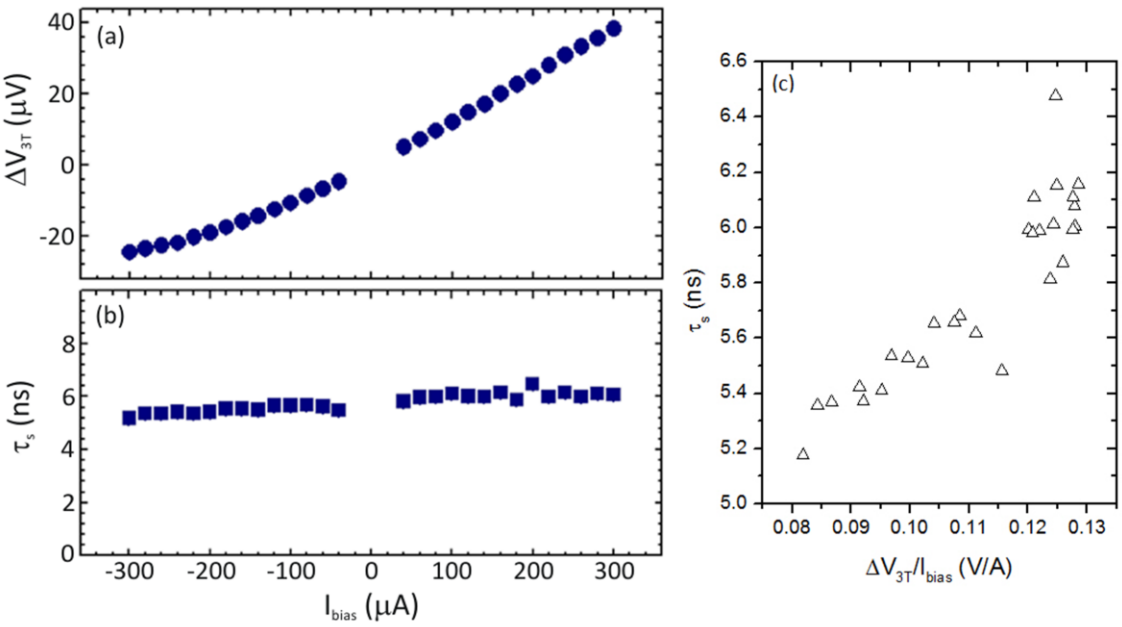

Figure 7.13 (a) Peak amplitude and (b) spin lifetimes extracted from the Hanle curves obtained at 50K for various currents from -300 to +300μA. (c)The spin lifetimes as a function of $\Delta V_{3T}/I_{bias}$.

In order to explore the reproducibility of the device behaviour measured, two other devices were characterised from the Fe/GaAs(001) film. The characteristics of these devices are within error (±10%) of the values obtained for the first device, confirming reproducible behaviour. The lack of polarisation inversion is not surprising in these devices. As discussed in section 6.2 the semiconductor doping profile is not expected to lead to transport from bound states. In section 6.4 the interface structure was presented with calculations suggesting that for the abrupt interface structure observed, minority carrier transport is not expected to be significant as no IRS form in the minority carrier spin sub-band. This is the first time that the atomic interface structure has been correlated to the transport properties in Fe/GaAs(001) devices.

7.3 Spin injection efficiencies

One of the biggest challenges for semiconductor spintronics is efficient electrical spin injection into a semiconductor. This also remains one of the most difficult parameters to characterise experimentally. The main difficulties arise from the fact that even if the spin accumulation can be measured experimentally, which itself is a difficult task, there are various other parameters that are not known such as the detailed electronic structure of the interface, discussed in section 3.3.1, and the polarisation of the ferromagnetic material close to the interface [159]. Even if assumptions are made of these important parameters there is still very little knowledge of the spin-dependent transport through the barrier [82], discussed in section 3.3.2. One of the simplest method for obtaining the spin injection efficiency is through measuring the polarisation of light emitted from a spin-LED structure [160]. Even this method has come under criticism due to the unknowns of the system [161].

One can estimate the injection efficiency from Hanle curves by relating the amplitude of the Hanle signals to the change in the electrochemical potential [162]. The tunnel spin polarisation P_{TSP} is given by

$$P_{TSP} = \frac{2\Delta V}{\Delta V(0)} \qquad (7.1)$$

where ΔV is the amplitude of the Hanle signal and $\Delta V(0)$ is extracted from fitting the Hanle curves (equation 5.6). If this simple model is used then an injection efficiency of ~4% is obtained at 10K for these devices. These are similar to values reported elsewhere [44, 49].

It should be noted that although the efficiencies cannot easily be determined the values for spin lifetimes, diffusion lengths and Hanle signal amplitudes allows a direct comparison of different devices. The results presented in this study show that Fe/GaAs(001) devices with the abrupt interface have long spin lifetimes, large spin diffusion lengths and also strong Hanle curves. This shows that Fe/GaAs(001) remains a strong candidate system for future devices.

Chapter 8. Other Studies

As well as using the intrinsic Schottky barrier to achieve efficient spin-polarised injection across the FM/SC interface, another possible solution to the conductivity mismatch problem is through the use of half-metallic ferromagnets. Creating half-metallic thin films at room temperature remains a major obstacle. The crystallisation processes and subsequent effect on the magnetic properties of polycrystalline Heusler alloy thin films, one of the most promising candidates, is crucial if these systems are to be utilised in future devices.

8.1 Polycrystalline Heusler alloys

8.1.1 Introduction

As well as using the intrinsic Schottky barrier to overcome the problem of the conductivity mismatch there are other possible solutions, discussed in chapter 1. Using half-metallic ferromagnets (HMF), which possess a band-gap δ at the Fermi level (E_F) for one spin population- thus achieving 100% polarisation, as the injector/detector contacts has many advantages. The half-metallicity means that no tunnel barrier is required for spin injection making the device fabrication process simpler [22]. This also eliminates the problems that arise from using a Schottky contact. There are various types of HMF's that have been considered but Heusler alloys have the greatest

potential due to their high Curie temperatures, good lattice matching with major substrates and large δ at E_F for one spin population [163]. Co_2FeSi is of particular interest as it has one of the highest Curie temperatures (>1100K) and the largest magnetic moments (~$6\mu_B$/f.u.) according to the generalised Slater-Pauling curve [164]. Heusler alloy tunnelling magnetoresistance (TMR) junctions have been intensively studied to explore the Heusler electrode polarisations, with potential applications for future memory devices [165-169]. Although half-metallic behaviour has been observed in bulk Heusler alloys, achieving 100% polarisation at room temperature in thin films remains elusive [170].

8.1.2 Sample preparation

An understanding of Heusler alloys thin films, grown using conventional sputtering techniques, is essential if Heusler alloys are to be used in future devices. In this study polycrystalline Co_2FeSi films were fabricated with controlled grain sizes in order to investigate the effect of annealing on both the magnetic and structural properties. Polycrystalline Co_2FeSi films were prepared using a High Target Utilisation Sputtering (HiTUS) sputtering system, shown schematically in figure 8.1 [171]. An Ar plasma was generated by an rf field at $3x10^{-1}$ Pa Ar pressure and steered onto the target with a dc bias ranging from -500 to -990 V, thus controlling the energy of the ions and hence the deposition rate. This results in a different degree of mixing of the elements from the target as well as different initial grain sizes. 20nm thick Co_2FeSi films were grown onto MgO(001) substrates at room temperature and capped with a 2 nm thick Ru layer. The films were systematically annealed at 500˚C in an Ar-rich environment for 3 to 9 h. After each anneal, magnetisation curves were measured using an ADE vibrating sample magnetometer (VSM) at room temperature. Bright field images and diffraction patterns were obtained using a JEOL JEM-2011 transmission electron microscope (TEM). Grain size analysis was performed using a Zeiss particle size analyser for between 300-850 grains per sample to obtain reliable results [172]. Each of the grains was assumed to be cylindrical for the size estimation.

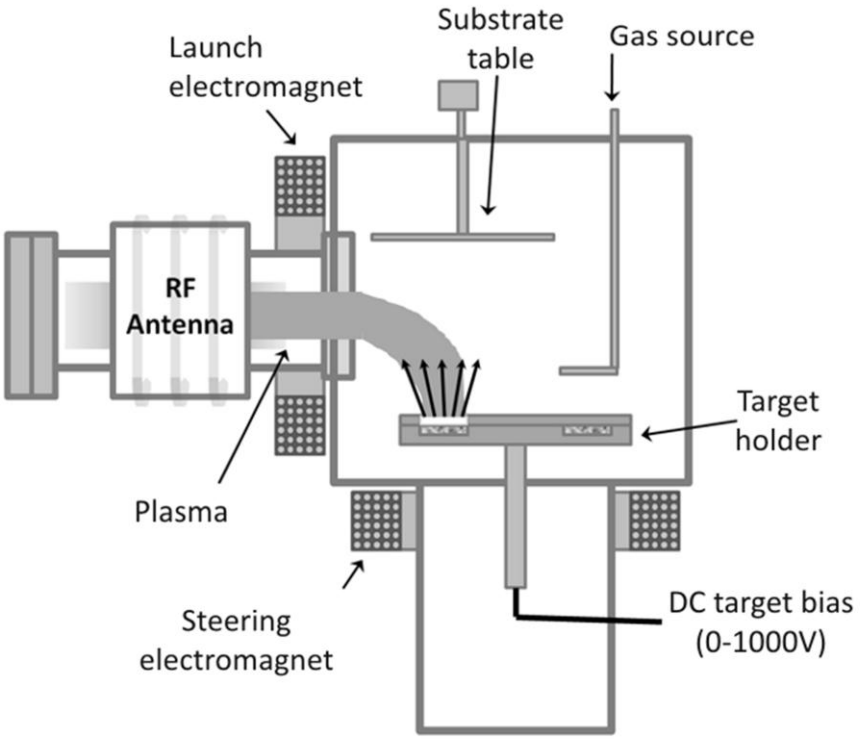

Figure 8.1 Schematic of the HiTUS sputtering system [171].

High resolution (HR) TEM images were obtained using an aberration correction JEOL JEM-2200FS microscope. The crystal structure of nanometre sized regions was evaluated using fast Fourier transformations (FFTs), also known as digital diffractograms. In order to interpret the contrast of the HRTEM images, HRTEM image simulations were produced using the electron microscopy software JEMS [129].

8.1.3 Grain size distribution

Analysis of TEM images show that the as-deposited Co_2FeSi films have an amorphous structure, with the magnetisation curves showing no hysteresis. Annealing the films at 500˚C for 3 hours leads to crystal formation with grains up to several hundred nanometres in diameter forming in the films grown with the largest bias, 990V (see Figure 8.2). The median grain size was dependent upon the growth bias voltage. In all of the films the grain size was found to fit a lognormal distribution.

$$F(D_{\text{grain}})dD_{\text{grain}} = \frac{1}{\sigma D_{\text{grain}}\sqrt{2\pi}} exp\left(-\frac{(lnD_{\text{grain}}-\mu_{\text{grain}})^2}{2\sigma_{SD}^2}\right) dD_{\text{grain}} \quad (8.1a)$$

$$\mu_{\text{grain}} = \frac{\sum Nln(D_{\text{grain}})}{\sum N} \quad (8.1b)$$

$$\sigma_{SD}^2 = \frac{\sum N(lnD_{\text{grain}})^2}{\sum N} - \left(\frac{\sum Nln(D_{\text{grain}})}{\sum N}\right)^2 \quad (8.1c)$$

where μ_{grain} is the log of the median grain diameter, σ_{SD} the log of the standard deviation of lnD_{grain} and D_{grain} is the grain diameter.

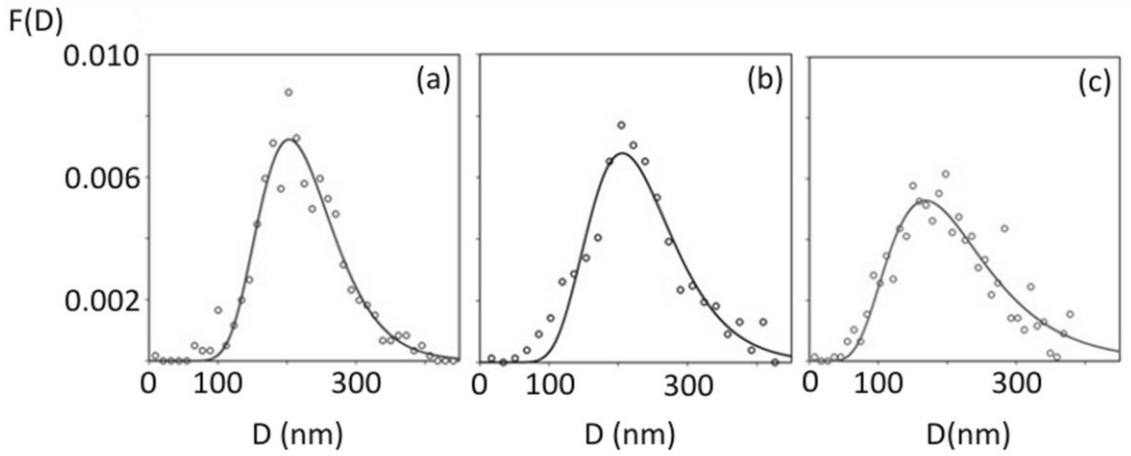

Figure 8.2 Distribution of grain sizes and corresponding lognormal fits for the films grown with a bias voltage of 990V after (a) 3, (b) 6 and (c) 9 hours annealing.

The median grain size and standard deviation for each of the lognormal fits are listed in Table 8.1. It can be seen from the table that the median grain size increases for the first 6 hours of annealing, reaching a maximum of (224±11)nm for the film grown at -990V, but then decreases after 9 hours. For the film grown at -500V the decrease of the grain size is more prominent. This result agrees well with a previous study performed on Co_2MnSi films using the same sputtering system, performed by Hirohata *et al.* [173]. In this report TEM and XRD techniques were used to show that this behaviour arose due to Si segregation. The increase in grain size with bias voltage agrees with the well-established grain evolution for the HiTUS system reported by Vopsaroiu *et al.* in 2005 [171].

Table 8.1. Annealing-time dependence of the grain size distributions for various bias voltages.

Bias voltage [V]	Annealing time [hours]	Median grain size [nm]	σ_{SD} (of lnD_{grain})
-500V	3	49 ± 3	0.29 ± 0.01
	6	64 ± 3	0.44 ± 0.03
	9	36 ± 2	0.70 ± 0.02
-750V	3	57 ± 3	0.36 ± 0.02
	6	59 ± 3	0.32 ± 0.01
	9	43 ± 3	0.32 ± 0.02
-990V	3	218 ± 11	0.26 ± 0.01
	6	224 ± 11	0.29 ± 0.01
	9	200 ± 10	0.41 ± 0.02

As the bias voltage increases the Ar ions become more energetic leading to an increased sputtering rate. Some of the energy will also be transferred to the target atoms, giving them a higher mobility upon reaching the substrate. This leads to different film morphologies and compositional mixtures for different bias voltages.

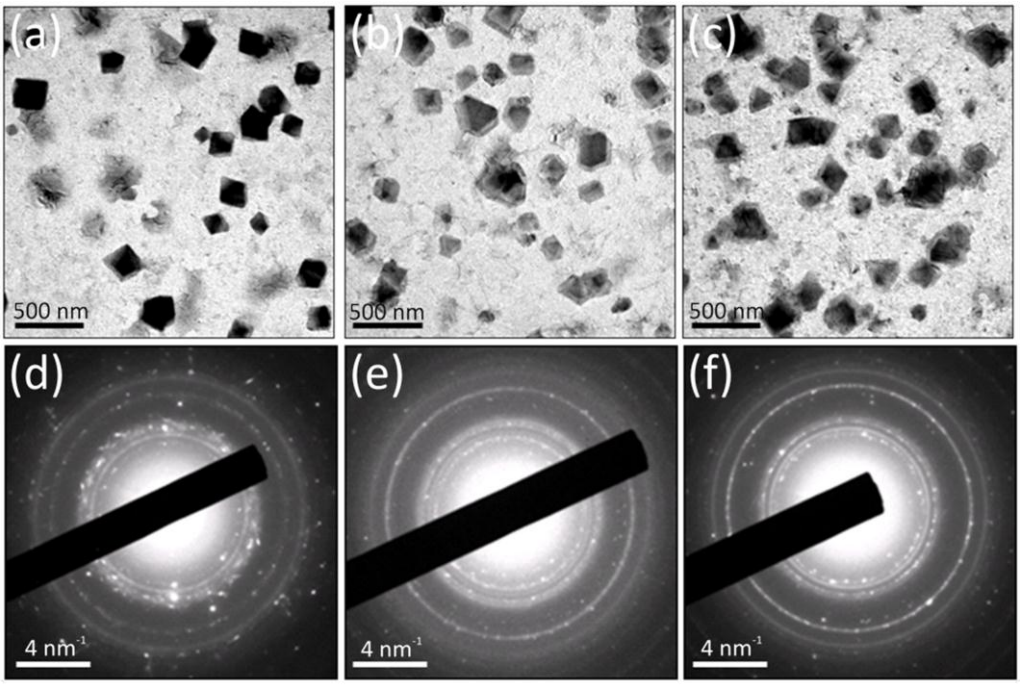

Figure 8.3 Typical TEM images for the film grown with a bias voltage of 990V after (a) 3, (b) 6, (c) 9 hours annealing, with corresponding selected area diffraction SAED patterns (d), (e) and (f).

The diffraction patterns in Figure 8.3 show clearly the crystallisation of the films with annealing time. After 3 hours the diffraction patterns contain rings of discrete spots, suggesting the films consist of well-ordered large grains. After 6 hours annealing the rings appears more continuous as some smaller grains are formed, consistent with the broadening of the grain size distributions (figure 8.1). After 9 hours of annealing the rings appear continuous. This is due to the presence of a large number of small grains which now appear leading to a lower median grain size.

8.1.4 Magnetic properties

Table 8.2 shows the magnetic moments and coercivities for the films as a function of the bias voltage. The magnetic moment was found to follow a similar trend to the grain size. The moment increases for up to 6 hours of annealing but decreases upon further annealing. The films with the smallest initial grain size again showed the most prominent change with the largest moment found in the film grown at -990 V after 6 hours annealing. This is ~75% of the moment derived from the generalized Slater-Pauling curve [164]. This suggests that not only the grains but also the matrix are well ordered.

Table 8.2. Annealing-time dependence of the magnetic moment and coercivity for various bias voltages.

Bias voltage [V]	Annealing time [hours]	Magnetisation [emu/cc]	M_r/M_s	H_c [Oe]
-500V	3	380 ± 60	0.94 ± 0.05	57 ± 4
	6	520 ± 80	0.96 ± 0.04	65 ± 4
	9	360 ± 60	0.93 ± 0.5	65 ± 4
-750V	3	440 ± 40	0.94 ± 0.04	155 ± 5
	6	540 ± 50	0.96 ± 0.04	163 ± 5
	9	560 ± 60	0.95 ± 0.4	166 ± 6
-990V	3	740 ± 40	0.90 ± 0.02	9 ± 2
	6	760 ± 40	0.78 ± 0.02	9 ± 2
	9	700 ± 40	0.80 ± 0.02	9 ± 2

It can be seen from the table that the films grown at -750V do not show a reduction in the moment after 9 hours of annealing and also have a much higher coercivity. It is also seen from table 8.1 that the grain size distribution does not widen with increased annealing time as with the other films. It is possible that the initial film morphology leads to films with an increased level of other structures forming such as $CoSi_2$, Co_2Si, FeSi, etc. Such interface disorder cannot be identified by macroscopic techniques, such as x-ray diffraction, and even from our HRTEM at this stage due to the close atomic number of the constituent atoms. This could lead to reduced levels of Si segregation and also increase the coercivity. It can be seen from table 8.2 that the films grown at -500V and -990V have low coercivities, particularly the film grown at 990V which has a coercivity of only 9Oe. This suggests that the bulk regions of these films are highly ordered. As the films grown at -990V have a lower squareness than the other films this suggests that a multi-step reversal is occurring as different grains reverse. The low coercivity suggests that the grains are quite strongly exchange coupled and also that domain walls are nucleated at low fields and propagate easily through the grains. For the films grown at -500V the median grain size is almost 150nm smaller than those for the films grown at -990V and the quality of the ordering is not as high, shown by the reduced magnetisation. These changes in the microstructure mean that a larger field is required to nucleate a domain wall. The high squareness shows that domain walls can still easily propagate through the grains and also that the grains are strongly exchange coupled. For the films grown at -750V the coercivity is much larger, over 100Oe greater than those of the other films, so a much greater field is required for a domain wall to be nucleated. The difference in the activation volumes for the films lies in the fact that the grains have a different level of ordering. This gives rise to a different saturation magnetisation and may also cause different anisotropies. The effect of the bias voltage on the physical grain volume and activation volume for similar Co_2FeSi Heusler alloy thin films was reported by Sagar *et al.* [174].

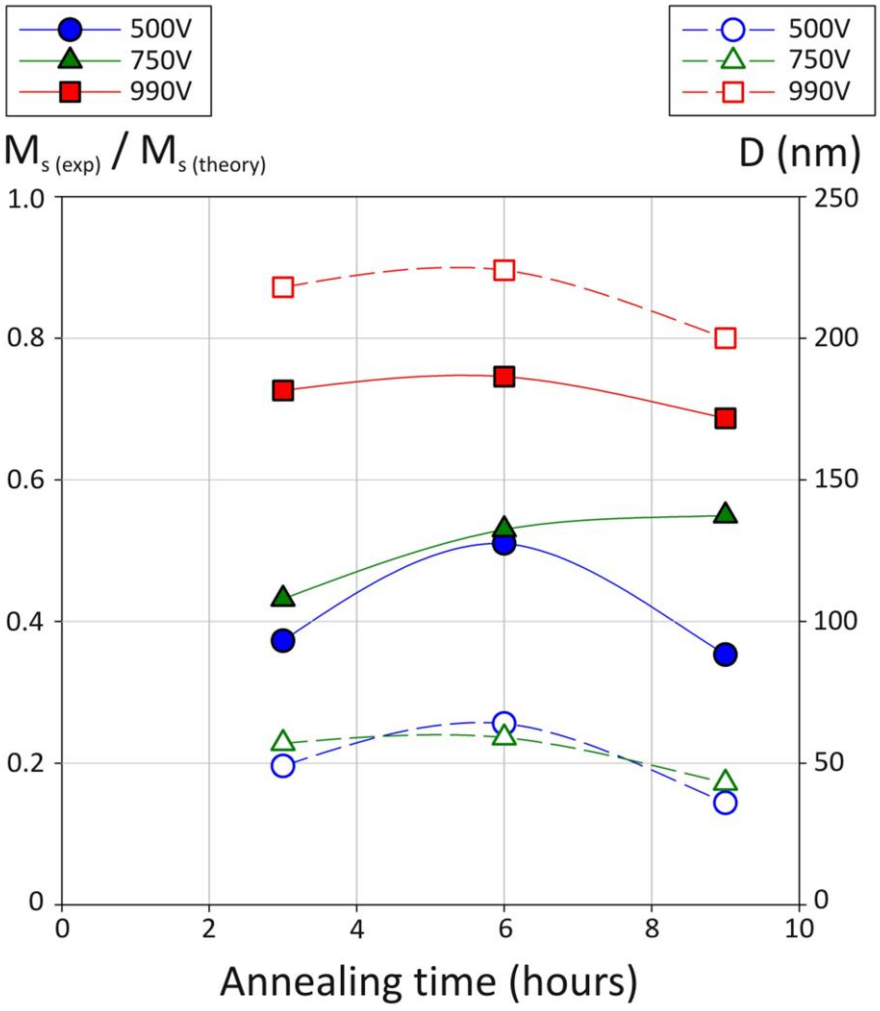

Figure 8.4 Annealing-time dependence of the magnetisation (solid symbols) and median grain size (open symbols) of Co_2FeSi films grown at steering bias of -500 (circles), -750 (squares) and -990 V (triangles).

Figure 8.4 shows a comparison between the median grain size and magnetic moment with respect to annealing time. It can be seen from the figure that there is excellent agreement for the films grown at 500 and 990V. The figure suggests that the initial creation of large grains is undertaken within the first few hours of annealing. Further annealing causes small changes in the grain size but leads to a significant increase in the magnetic moment. This suggests that there is also crystallographic restructuring and atomic ordering of the grains and/or matrix occurring. Further annealing causes a reduction in the grain size as Si starts to segregate [173], thus leading to a reduced magnetic moment.

8.1.5 Structural analysis

Analysis of the as-deposited films using HRTEM (figure 8.5) showed that they consist of a mixture of nano-crystalline and amorphous regions. It can be seen that as the bias voltage increases the number of spots in the diffractograms increases, showing the increase in nanocrystalline order. Energy dispersive X-ray spectroscopy (EDX) showed that the film composition was invariant with the bias voltage. Quantitative EDX is very difficult to perform, particularly in TEM samples due to multiple scattering. Although the composition of the films could therefore not be determined easily, a change in the composition of the films could be observed.

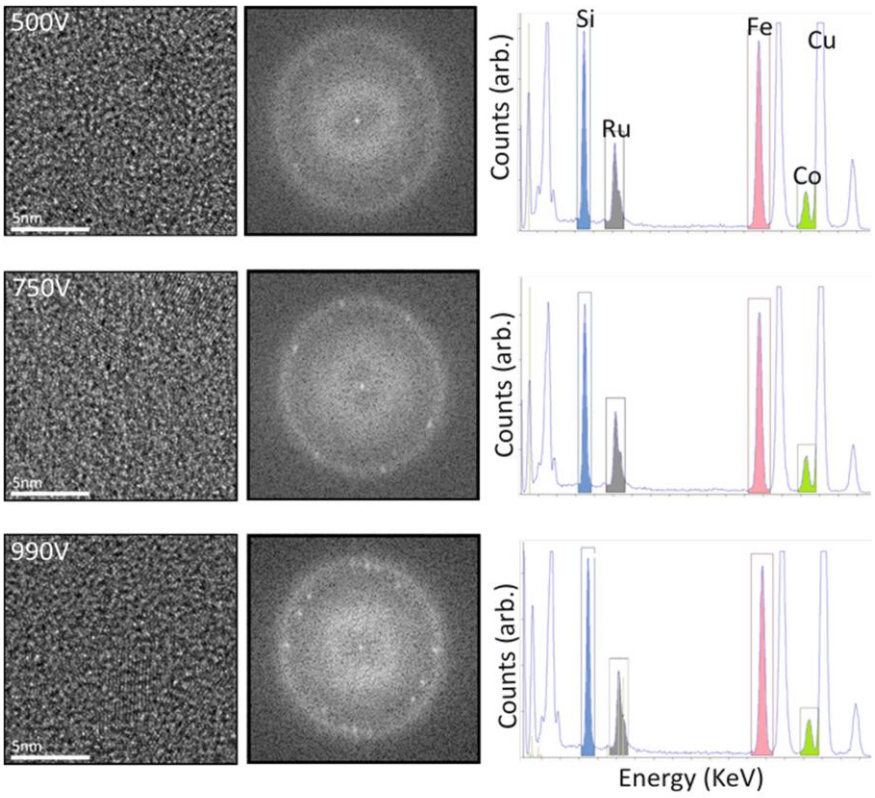

Figure 8.5 HRTEM and diffractograms of Co_2FeSi films grown at -500, -750 and -990V with corresponding EDX data showing no change in composition.

Figure 8.5 shows several peaks highlighted for Si, Ru, Fe, Co and the large Cu peak arising from the TEM grid. If the samples had different compositions then the ratio of the number of counts for the different elements would be altered. As the samples all have the same intensity relationship for the Si, Ru, Fe and Co peaks it is assumed that no compositional change occurs between the samples grown at different bias voltages.

The structure of the largest grains was determined by analysing the grains produced after 6 hours of annealing for the film grown with the largest bias voltage. The grains were found to be well ordered with well-defined cubic structures. Although some grains were found to lie in [100] and [11-1] orientations, approximately 80% of the grains were orientated along the [112] zone axis. Figure 8.6 shows a typical TEM image of one the grains analysed along with the corresponding selected area diffraction (SAED) pattern.

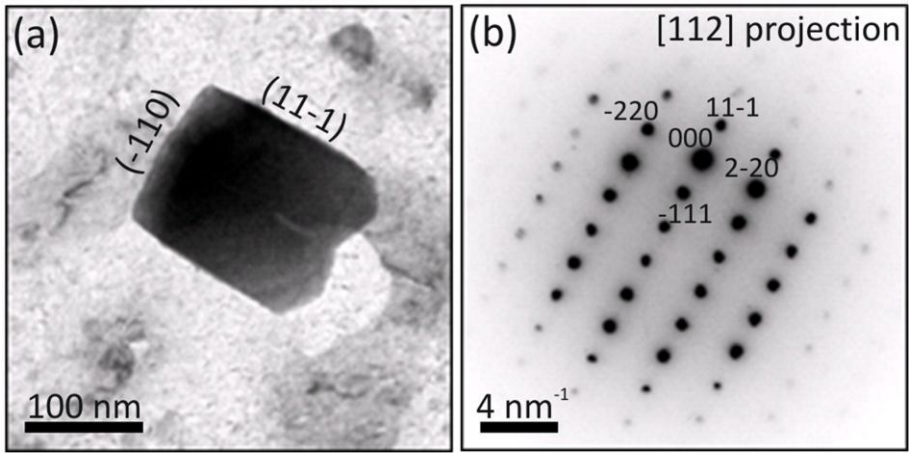

Figure 8.6 (a) TEM image and (b) SAED pattern of a grain from the film grown at -990V.

HRTEM images were also obtained to explore the film ordering. Figure 8.7(a) shows a HRTEM image of a grain in the [112] orientation. This orientation was confirmed through analysis of the optical diffraction pattern shown in figure 8.7(b).

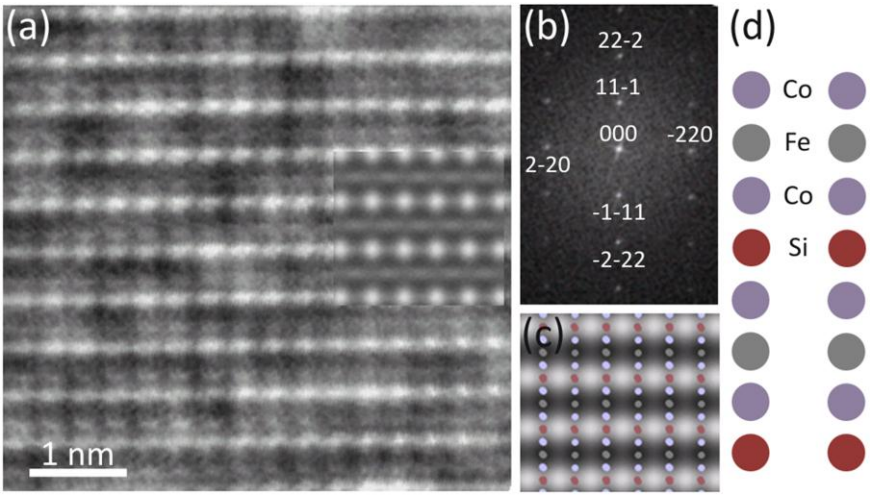

Figure 8.7 (a) HRTEM image obtained for typical grain with image simulation. (b) Optical diffraction pattern showing [112] spot pattern. (c) Image simulation showing the position of the atomic columns. (d) Schematic of $L2_1$ ordered Co_2FeSi in the [112] projection.

Image simulations were produced to study the atomic structure of the grains. In the simulations the grains were $L2_1$ ordered, orientated along the [112] zone axis. The simulation can be seen as an inset into figure 8.6(a) with excellent matching found. This [112] orientation leads to an interesting structure of the films. The grains consist of rows of atoms of the same elements as shown in figures 8.7(c) and (d). The layered structure follows the sequence of $(Co, Fe, Co, Si)_n$, layer-by-layer lattice formation. The position of the atomic columns in relation to the simulation can be seen in figure 8.7(d). This suggests an $L2_1$ crystallisation process in the layer-by-layer mode. This process may induce preferential orientation of crystalline planes for stable and uniform lattice formation which may be useful for junction fabrication.

8.2 Heusler alloy crystallisation

8.2.1 Experimental set-up

In order to develop Heusler alloys for use in devices knowledge of the crystallisation process is required. There have been several studies performed on large single crystal Heusler alloys thin films but there is little understanding of polycrystalline sputtered films, particularly the crystallisation processes [175]. This is of great importance as one of the major challenges for Heusler alloys is that annealing at high temperatures, typically above 400°C, is required to achieve a high degree of $L2_1$ ordering. Although some Heusler alloys maintain a high degree of spin-polarisation in the B2 phase, high temperatures are still required to achieve a high degree of B2 ordering. As multilayer devices cannot be annealed at such high temperatures due to interdiffusion between layers, the ability to generate high ordering at low annealing temperatures would be a major breakthrough, particularly if this ordering could be created in polycrystalline films.

To explore the crystallisation process of polycrystalline Co_2FeSi films, 20nm thick films were sputtered with a bias voltage of -990V as this gives the largest median grain size. The films were sputtered onto CuC and SiN TEM grids, capped with a 5 nm thick

Ru layer. The films were annealed in-situ in a JEOL JEM-2200FS microscope using a Gatan TEM heating holder from room temperature up to 600°C. Videos were recorded using Camtasia studio software, with conventional images obtained using the software digital micrograph. Both the TEM and diffraction patterns could be recorded but not simultaneously due to the different experimental conditions required.

8.2.2 In-situ results

A preliminary experiment was performed to determine the temperature required for the crystallisation to occur. This was found to be (230±10)°C, although it should be noted that the temperature of the sample cannot be determined experimentally. The value for the temperature was obtained by comparing the current applied to the heating stage with the manufacturers manual, with Gatan performing the calibration before shipment. This low annealing temperature would be very useful in device fabrication. The first experiment performed was to hold the temperature at 230°C and observe both the TEM and diffraction patterns to see how the films crystallise.

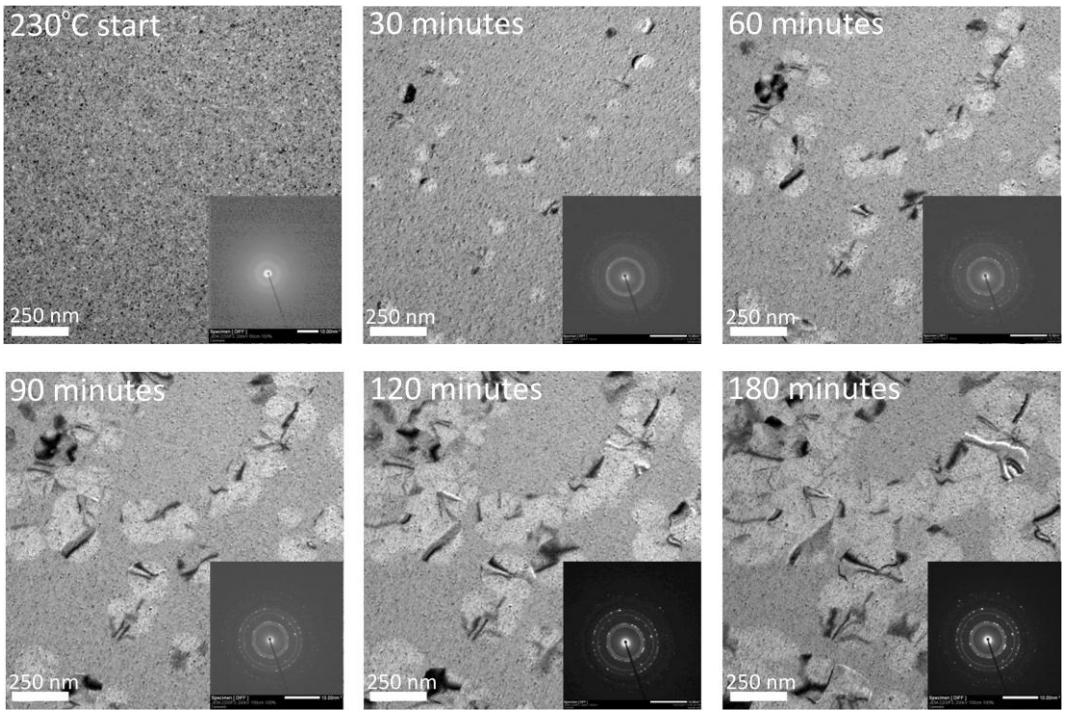

Figure 8.8 TEM images with diffraction patterns for Co_2FeSi films annealed at 230°C for up to 3 hours.

It can be seen from figure 8.8 that the films first appear amorphous and only after approximately 30 minutes annealing do small grains start to form, ~20nm in size. Further annealing mainly leads to growth of the initial grains with no new grain nucleation appearing to occur after 30 minutes. The diffraction pattern obtained after 90 minutes shows a spotty ring structure, showing the formation of ordered grains. Further annealing up to 3 hours causes large well ordered grains to form. Analysis of the diffraction pattern obtained after 3 hours annealing (figure 8.9) shows an excellent match with that expected for $L2_1$ ordered Co_2FeSi. The diffraction pattern rings were generated using JEMS for an ideal $L2_1$ ordered Co_2FeSi film. The amount of disordered material in structures such as B2 or A2 cannot be determined. Further study is needed to determine the level of order in this film but the use of a low temperature anneal to create well ordered polycrystalline films has many potential industrial applications.

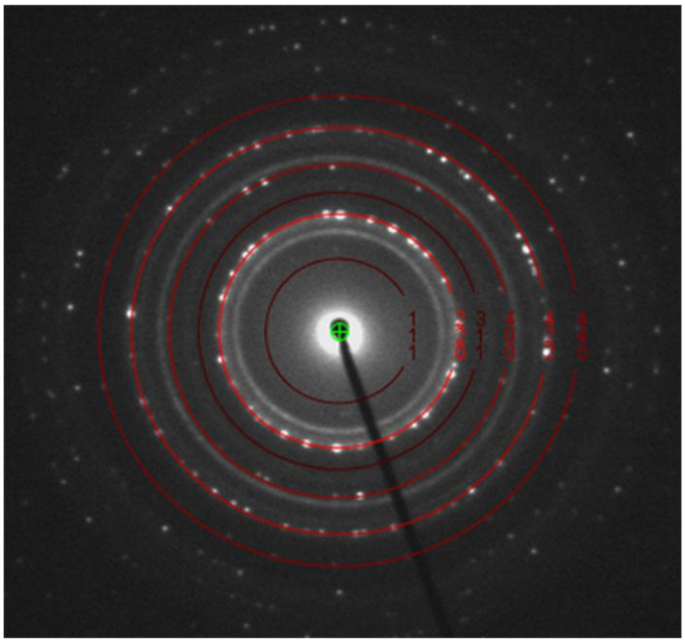

Figure 8.9 Diffraction pattern of Co_2FeSi film after 3 hours annealing at 230°C with the red rings showing the predicted rings for $L2_1$ ordered Co_2FeSi calculated using JEMS.

As well as using a low temperature anneal to create the grains it has been shown in section 8.1 that a high temperature anneal can be used to create very large ordered grains. To explore the effect of high temperature annealing the samples, grown on both SiN and CuC grids, were annealed from 300°C to 550°C over a 3 hour period. It can be seen from the increase in contrast in figure 8.10 that an increase in order occurs. At temperatures above 500°C the grains begin to become striped, suggesting

further restructuring may be occurring. However, the presence of stripes indicates that there remains significant stress in the grains that is not removed by annealing at this temperature and further research is clearly needed. The crystallisation process is still unclear, however, this experiment has shown that in-situ annealing can help to understand and develop polycrystalline Heusler alloy films with an appropriate microstructure for applications.

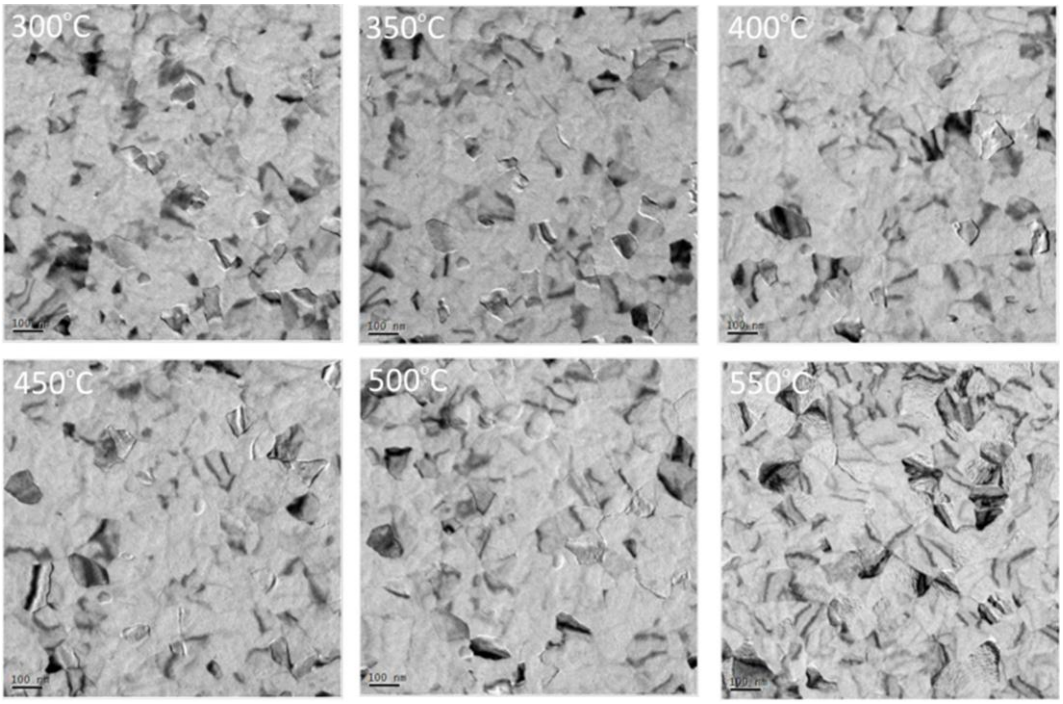

Figure 8.10 TEM images for Co_2FeSi films annealed from 300°C to 550°C over 3 hours.

Although there are numerous advantages for Heusler alloys, if they are to be used to inject spin-polarised electrons efficiently into a semiconductor, with close to 100% spin-polarisation, control of their microstructure is required. This is yet to be achieved and there is still a great deal of work required if Heusler alloys are to be utilized in future semiconductor spintronic devices.

This work was presented as an invited talk at the MMM conference at the 55th annual MMM conference in Scottsdale Arizona in November 2011.

Chapter 9. Conclusions and Future Work

9.1 Conclusions

In this work it was shown that Fe/GaAs(001) films grown using UHV MBE consist of different interface structures. Low temperature annealing was shown to reduce the level of mixing in the films from ~30% to ~5-10%. The interface structures were confirmed using HAADF-STEM imaging with the majority of the films having an abrupt interface with some regions showing partial mixing. Multiple interface structures gives rise to a distribution of Schottky barrier heights which has a significant effect on the transport properties. Ab initio calculations show that for the abrupt interface no significant minority carrier injection will occur. The magnetotransport properties of three-terminal devices confirm that this is the case. Calculations of the partially mixed interface suggest that minority carrier injection through interface resonance states could be significant. The magnetotransport properties of devices confirm that electrical spin injection could be achieved with the spin diffusion length calculated to be (16±1)μm at 10K, with spin lifetimes of over (15±1)ns at 10K [176].

From these reports it can be concluded that it is possible to fabricate well-behaved reproducible devices from Fe/GaAs(001) films, something which has so far been a major obstacle. In order to achieve efficient reproducible behaviour an abrupt interface is required as partial mixing gives rise to minority carrier interface resonance states. Although low temperature annealing reduces the level of mixing, thereby changing the shape of the Schottky barrier distribution, previous interface

observations [45, 46] suggest that the conditions of the Fe deposition play a key role in the interface structure. Greater knowledge of how to control the interface is required in this system.

Hence these results raise the possibility that Fe/GaAs(001) devices could be utilised in future spintronic devices. One of the greatest obstacles still remains the signal strength and operation temperature. Although spin injection could be achieved the temperature which it could be detected was only 120K due to the three-terminal configuration. In order to develop this system further a greater understanding is needed of the decay of the spin-polarised electrons as they tunnel through the depletion region and also on how to control the interface structure.

9.2 Future work

9.2.1 Growth control

In order to develop the Fe/GaAs(001) system further a deeper understanding of the formation of the interface structure is required. The work presented in this thesis, using the (1x1) GaAs surface reconstruction, shows that it is possible to create different interface structures. In these studies [45, 46] Fe deposition was performed on a β(2×4) surface reconstruction with post-deposition annealing at 200°C for 10 minutes or onto a *c*(4×4) surface reconstruction with a post-deposition annealing at 200°C for 1 hour. The thickness of the films in those studies and this work were approximately 5nm and the post-annealing conditions very similar. This suggests that the cause of the different interface structures is probably the GaAs(001) surface reconstruction. To confirm this hypothesis the interface structure of Fe/GaAs(001) films needs to be studied for various surface reconstructions. Several As- and Ga-rich reconstructions need to be explored to help understand the effect of diffusion on the interface structure.

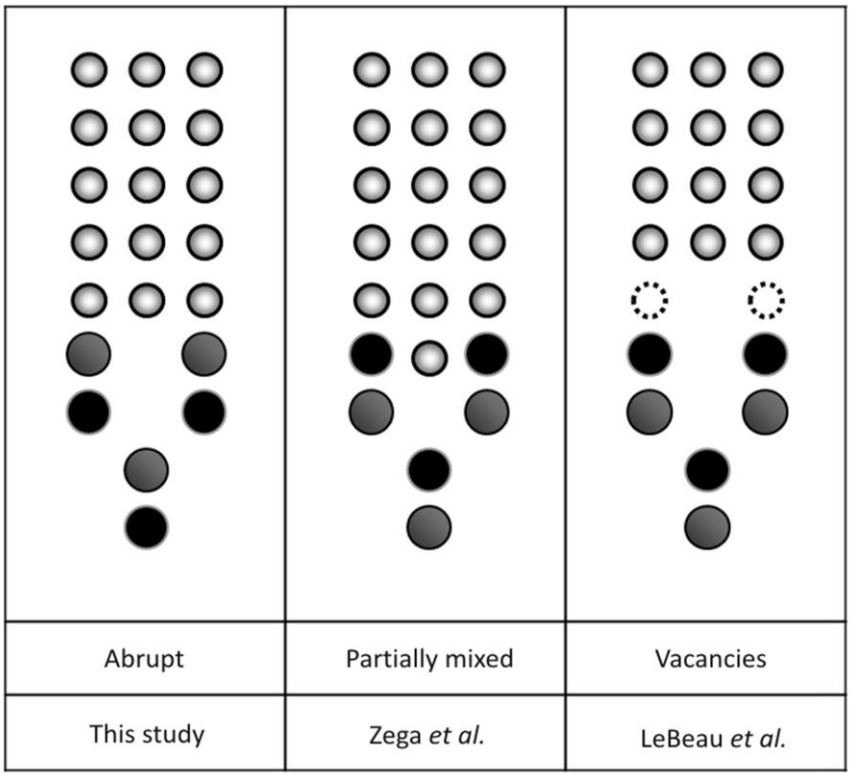

Figure 9.1 Three different interfacial structures observed in Fe/GaAs(001) films [45, 46].

As well as exploring the effect of the surface reconstruction of GaAs(001) it would be interesting to study different GaAs orientations. The main reason this is of interest is due to the 2009 paper by Grunebohm *et al*. [177]. In this report their calculations suggested that abrupt Fe/GaAs(110) interfaces could be created easily as the GaAs(110) surface does not reconstruct. This should eliminate the problems arising from the different interface structures but not the limitations arising from transport across the Schottky barrier. Li *et al.* used a spin-LED to explore the transport across the Fe/GaAs(110) interface [178]. They showed that the (110) structure behaves similarly to the (001) structure. This suggests that efficient injection may still be limited by the transport mechanisms across the barrier but further work is required to confirm that the (110) surface does not reconstruct and also to relate the interface structure to the transport properties.

9.2.2 Other systems

Although there has been a recent report on room temperature spin injection into Si [162] there is yet to be the same demonstration made in GaAs. As well as using the intrinsic Schottky barrier to overcome the limitations of the conductivity mismatch there are other possible solutions to achieve efficient injection into GaAs. For example an extrinsic barrier such as Al_2O_3 or MgO could be used or a material with a similar conductivity could be employed as the injector. Optimally a 100% spin-polarised material could be used as the injector. Using MgO as the tunnel barrier has many benefits as coherent tunnelling through the barrier could lead to an increase in the injection efficiency [57]. MgO also overcomes the limitations from the Schottky barrier and the various mechanisms that act to reduce the device efficiency. Achieving high quality devices using MgO is challenging and efficient injection has not been demonstrated across an Fe/MgO/GaAs(001) junction.

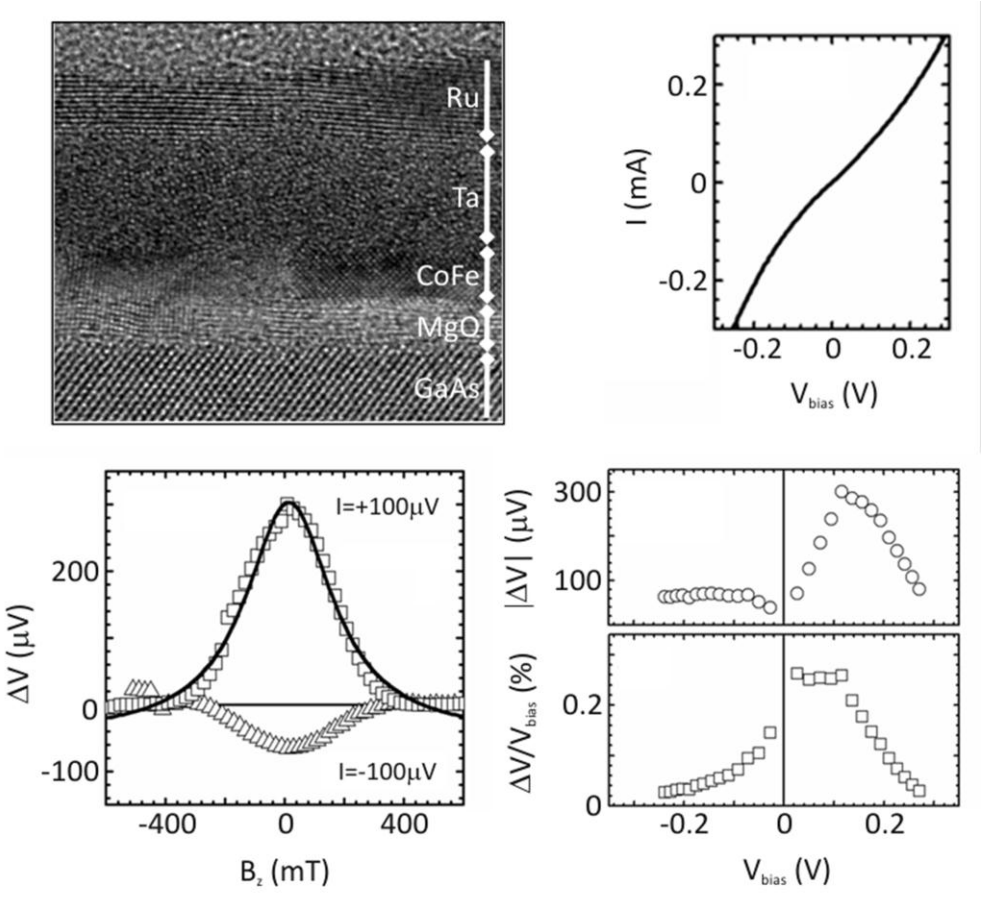

Figure 9.2 TEM image of Ru/Ta/CoFe/MgO/GaAs sample with the I-V characteristics and electrical properties obtained at 10K.

One of the major advantages of an extrinsic barrier is that it allows the use of other materials as the injector. This removes the need for lattice matching to GaAs which would allow for materials to be prepared using sputtering. One alternative system which has been explored is GaAs(001)/MgO/CoFe prepared by conventional magnetron sputtering, with the substrates fabricated using MBE. Using the same experimental set-up as the Fe/GaAs(001) system three-terminal devices were used to demonstrate spin-polarised injection. Hanle curves were obtained up to 160K but the spin lifetimes were only (146±7)ps at 10K, much lower than the Fe/GaAs(001) system. The devices also showed a strange bias dependence which is not well understood. It is clear that much work is required to advance these systems further.

List of Symbols

↑ (↓)	Up (down) spin band
A	Richardson's constant
A^*	Effective Richardson's constant
$A_{1(2)}$	Coefficients used to describe transport across FM/SC interface
A_0	constant used in calculating the conductance through the BDR model
α	$=\sigma_{\uparrow}/\sigma$ $=1-(\sigma_{\downarrow}/\sigma)$ Conductivity variable
α_C	Conductivity variable at the FM/SC contact
α_S	Conductivity variable in the semiconductor
β	Coupling parameter used in the model by Smith and Ruden
B	Applied magnetic field
B_{eff}	Effective magnetic field
c	Speed of light in vacuum
D	Diffusion constant
D_{grain}	Grain diameter
δn	Charge in particle density
$\Delta\Phi_{12}$	Difference in the two potentials used in the BDR model
e	Electronic charge
$\boldsymbol{E}$	Electric field
E	Energy
E_0	Parameter related to tunnelling current
E_{00}	Parameter relating importance of thermionic emission to tunnelling
E_C	Energy at the bottom of the conduction band
E_{ex}	Exchange energy
E_F	Fermi energy
$E_{F(M)}$	Fermi energy in metal
$E_{F(SC)}$	Fermi energy in semiconductor
E_G	Band gap energy
E_K	Eigen energy
E_V	Energy at the top of the valence band
ε'	Tunnelling parameter under reverse bias
ε_0	Permittivity of free space
ε_S	Dielectric constant
ε_{SC}	Semiconductor permittivity
$f(k)$	Electron distribution function
$f_1(k)$	Linear response to the distribution function
$f_{FD}(k)$	Equillibrium Fermi distribution
F	Fourier transform
F_{image}	Force due to image charges
F_p	Probability of emission
F_q	The ratio of the total current flow to the thermionic
g	Gyromagnetic ratio
G	Conductance
G_0	Saturation conductance

Γ-point	Centre of the Brillouin zone
h ($\hbar$)	Planck's constant (divided by 2π)
H_D	Demagnetising field
H_R	Rashba Hamiltonian
H_{SO}	Spin-orbit interaction Hamiltonian
η	$=J_{\uparrow}/J \quad =1-(J_{\downarrow}/J)$ Current density parameter
I	Current
$I_{0_{TE}}$	Saturation current due to thermionic emission
$I_{0_{TFE(F)}}$	Forward bias saturation current due to TFE
$I_{0_{TFE(R)}}$	Reverse bias saturation current due to TFE
$I_{0_{FE(F)}}$	Forward bias saturation current due to FE
$I_{0_{FE(R)}}$	Reverse bias saturation current due to FE
$\boldsymbol{J}$	Current density
$\boldsymbol{J}_{2D}$	Spin dependent current density due to the escape of localised electrons from bound states
J_{ex}	Exchange integral
φ	Projected slice potential
Φ_0	Neutral level
$\Phi_{1(2)}$	Barrier potentials used in the BDR model
Φ_B	Schottky barrier height
Φ_{eff}	Effective barrier height
Φ_{ideal}	Theoretical potential in the Schottky barrier (no image force lowering)
Φ_{image}	Potential due to image forces
Φ_{total}	Total potential in the Schottky barriers (accounting for image forces)
Φ_M	Metal work function
Φ_n	$=E_C-E_{F(SC)}$ Penetration of Fermi level into the band gap
Φ_{SC}	Semiconductor work function
$\psi(x)$	Wavefunction
ψ_0	Initial wavefunction
ψ_{ex}	Exit wavefunction
ψ_{SC}	Wavefunction in semiconductor
k	wave vector
$k_{\|\|}$	Parallel wave vector
k_B	Boltzmann's constant
k_S	Shape anisotropy constant
χ	Scattering coefficient
χ_S	Electron affinity in the Semiconductor
λ	Spin diffusion length (Position dependent)
λ_C	Spin diffusion length at the FM/SC contact
λ_e	Electron diffusion length
λ_{sf}	Spin-flip length
λ_S	Spin diffusion length in semiconductor
m_e	mass of electron
m^*	Effective mass

m^*_m	Effective mass in the metal near the Fermi level
M	Magnetisation
M_r	Remanent magnetisation
M_s	Saturation magnetisation
μ	Electrochemical potential
μ_B	Bohr magneton
μ_{ch}	Chemical potential
μ_e	Electron mobility
μ_{grain}	Median grain diameter
n	Excess particle density
n^-	Lightly doped
n^+	Heavily doped
n_j	areal density of electrons in the *j*th state whose energy is higher than the Fermi energy of the ferromagnet
n_k	electron occupation for each state
$N_{\|\|}$	Number of atoms on an atomic plane
$N(E_F)$	Density of states at the Fermi energy
N_d	Doping concentration
N_{short}	Shape demagnetising factor along the short axis of a prolate spheroid
N_{long}	Shape demagnetising factor along the long axis of a prolate spheroid
p	Momentum vector
P	Polarisation of a material
P_{TSP}	Tunnel spin polarisation
$\boldsymbol{P}_F$	Fresnel propagator
q	Charge
$\boldsymbol{q}_{PO}$	Phase object function
q_{Vi}	$=\Phi_M-\Phi_{SC}$
ΔR	Change in resistance between parallel and antiparallel orientations
R_A	Resistance for antiparallel orientation of electrodes in a spin-valve
R_C	Interface resistance
R_P	Resistance for parallel orientation of electrodes in a spin-valve
R_S	Semiconductor resistance
S	Diode area
$\boldsymbol{S}_{i(j)}$	Spin angular momentum vector of atom i(j)
$\boldsymbol{S}_{x(y)}$	Spin components along x(y)
$\boldsymbol{\sigma}$	Conductivity
σ_C	Interface conductivity
$\boldsymbol{\sigma}_i$	Pauli spin matrices
σ_{int}	Interaction constant
σ_S	Semiconductor conductivity
σ_{SD}	Standard deviation
Ω	Spin precession frequency
Ω_{av}	Average spin precession frequency
t_{SB}	Schottky barrier thickness
t_{rep}	Laser repetition pulse interval

T	Temperature
T_1 or τ_s	Spin relaxation time
T_2	Spin dephasing time
T_2^*	Spin dephasing time for reversible phase losses
$\boldsymbol{T}_{\uparrow(\downarrow)}$	Spin dependent transmission coefficient
τ_0	Minority carrier lifetime in the depletion region
$\tau_{\uparrow(\downarrow)}$ or τ_{sf}	Spin-flip times
$\tau_{j,\uparrow(\downarrow)}^{esc}$	Spin dependent escape rate of electrons from bound states
τ_C	Correlation time
τ_p	Momentum relaxation time
$\boldsymbol{U}_E$	Potential energy
$\boldsymbol{v}$	Velocity
V	Electrostatic potential difference
V_i	$= (\Phi_m - \Phi_s)/q$ internal voltage
$\boldsymbol{u}_D$	Drift velocity
$\boldsymbol{u}_K$	Group velocity
$\boldsymbol{u}_R$	Recombination velocity
w	Depletion layer width
Z	Proton number

List of Abbreviations

2DEG	2-dimensional electron gas
AMR	Anisotropic magnetoresistance
bcc	Body-centered cubic
BDR	Brinkman-Dynes-Rowell
BF	Bright field
C_5	Fifth order spherical aberration
C_C	Chromatic aberration
C_S	Spherical aberration
CCD	Charge-coupled-device
CEOS	Corrected electron optical systems
CMOS	Complimentary metal-oxide-semiconductor
CTF	Contrast transfer function
DFT	Density function theory
DIGS	Disordered gap states
DMS	Dilute magnetic semiconductor
DNP	Dynamic nuclear polarisation
DOS	Density of states
EDX	Energy-dispersive X-ray spectroscopy
E-gun	Electron gun
FE	Field emission
FEG	Field emission gun

FET	Field effect transistor
FM	Ferromagnet
FM/SC	Ferromagnet/Semiconductor interface
FWHM	Full width half maximum
GMR	Giant magnetoresistance
HAADF	High angle annular dark field
HMF	Half-metallic ferromagnet
HiTUS	High Target Utilisation Sputtering
HRTEM	High resolution transmission electron microscopy
I-V	Current-voltage
IRS	Interface resonance states
K-cell	Knudsen cell
LED	Light emitting diode
LEED	Low energy electron diffraction
MBE	Molecular beam epitaxy
Metal/SC	Metal/semiconductor interface
MIGS	Metal induced gap states
MOKE	Magneto-optical Kerr effect
MOSFET	Metal-oxide-semiconductor field effect transistor
MTJ	Magnetic tunnel junction
RHEED	Reflected high energy electron diffraction
RIEC	Research Institute of Electrical Communication
SAED	Selective area electron diffraction
SC	Semiconductor
SI	Metric international system
SKEM	Scanning Kerr electron microscopy
Spin-FET	Spin field effect transistor
Spin-LED	Spin light emitting diode
STEM	Scanning transmission electron microscopy
TE	Thermionic emission
TEM	Transmission electron microscopy
TFE	Thermionic field emission
TMR	Tunnelling magnetoresistance
UHV	Ultra high vacuum
UV	ultra-violet
VSM	Vibrating sample magnetometer
XRD	X-ray diffraction
ZBR	Zero bias resistance

References

[1] S. M. Sze and K. K. Ng, *Physics of semiconductor devices* (Wiley-Interscience, Hoboken, N.J., 2007).
[2] G. E. Moore, P Ieee **86**, 82 (1998).
[3] S. A. Wolf, D. D. Awschalom, R. A. Buhrman, J. M. Daughton, S. von Molnar, M. L. Roukes, A. Y. Chtchelkanova, and D. M. Treger, Science **294**, 1488 (2001).
[4] G. A. Prinz, J Magn Magn Mater **200**, 57 (1999).
[5] D. D. Awschalom and M. E. Flatte, Nature Physics **3**, 153 (2007).
[6] W. Thomson, Proceedings of the Royal Society of London **8**, 5 (1857).
[7] P. Wisniewski, Appl Phys Lett **90** (2007).
[8] G. Binasch, P. Grunberg, F. Saurenbach, and W. Zinn, Phys Rev B **39**, 4828 (1989).
[9] M. N. Baibich, J. M. Broto, A. Fert, F. N. Vandau, F. Petroff, P. Eitenne, G. Creuzet, A. Friederich, and J. Chazelas, Phys Rev Lett **61**, 2472 (1988).
[10] S. M. Thompson, J Phys D Appl Phys **41** (2008).
[11] M. Julliere, Phys Lett A **54**, 225 (1975).
[12] J. S. Moodera, L. R. Kinder, T. M. Wong, and R. Meservey, Phys Rev Lett **74**, 3273 (1995).
[13] T. Miyazaki and N. Tezuka, J Magn Magn Mater **151**, 403 (1995).
[14] S. Ikeda, J. Hayakawa, Y. Ashizawa, Y. M. Lee, K. Miura, H. Hasegawa, M. Tsunoda, F. Matsukura, and H. Ohno, Appl Phys Lett **93**, 082508 (2008).
[15] N. F. Mott, Proceedings of the Royal Society of London **156**, 10 (1936).
[16] I. A. Campbell, A. Fert, and R. Pomeroy, Philosophical Magazine **15**, 977 (1967).
[17] A. Fert and I. A. Campbell, Phys Rev Lett **21**, 1190 (1968).
[18] J. M. Kikkawa and D. D. Awschalom, Phys Rev Lett **80**, 4313 (1998).
[19] S. Datta and B. Das, Appl. Phys. Lett. **56**, 665 (1990).
[20] B. T. Jonker, P Ieee **91**, 727 (2003).
[21] G. Schmidt, D. Ferrand, L. W. Molenkamp, A. T. Filip, and B. J. van Wees, Phys Rev B **62**, R4790 (2000).
[22] E. I. Rashba, Phys Rev B **62**, R16267 (2000).
[23] A. Fert and H. Jaffres, Phys Rev B **64** (2001).
[24] R. A. de Groot, F. M. Mueller, P. G. v. Engen, and K. H. J. Buschow, Phys Rev Lett **50**, 2024 (1983).
[25] C. Felser, G. H. Fecher, and B. Balke, Angewandte Chemie International Edition **46**, 668 (2007).
[26] A. Hirohata and Y. Otani, (Transworld Research Network, 2009).
[27] H. Ohno, Science **281**, 951 (1998).
[28] K. F. Eid, B. L. Sheu, O. Maksimov, M. B. Stone, P. Schiffer, and N. Samarth, Appl Phys Lett **86**, 152505 (2005).
[29] B. L. Sheu, K. F. Eid, O. Maksimov, N. Samarth, and P. Schiffer, J Appl Phys **99**, 08D501 (2006).
[30] L. Chen, X. Yang, F. Yang, J. Zhao, J. Misuraca, P. Xiong, and S. von Molnár, Nano Lett **11**, 2584 (2011).
[31] K. Y. Wang, K. W. Edmonds, L. X. Zhao, M. Sawicki, R. P. Campion, B. L. Gallagher, and C. T. Foxon, Phys Rev B **72**, 115207 (2005).
[32] U. Wurstbauer, M. Sperl, M. Soda, D. Neumaier, D. Schuh, G. Bayreuther, J. Zweck, and W. Wegscheider, Appl Phys Lett **92**, 102506 (2008).
[33] W. Z. Wang, J. J. Deng, J. Lu, L. Chen, Y. Ji, and J. H. Zhao, Physica E: Low-dimensional Systems and Nanostructures **41**, 84 (2008).
[34] Y. J. Cho, K. M. Yu, X. Liu, W. Walukiewicz, and J. K. Furdyna, Appl Phys Lett **93**, 262505 (2008).

[35] G. M. Schott, C. Ruster, K. Brunner, C. Gould, G. Schmidt, L. W. Molenkamp, M. Sawicki, R. Jakiela, A. Barcz, and G. Karczewski, Appl Phys Lett **85**, 4678 (2004).
[36] X. Jiang, Phys. Rev. Lett. **94**, 056601 (2005).
[37] A. V. Narlikar, *Frontiers in magnetic materials* (Springer, Berlin ; New York, 2005).
[38] P. Mavropoulos, N. Papanikolaou, and P. H. Dederichs, Phys Rev Lett **85**, 1088 (2000).
[39] G. Kirczenow, Phys Rev B **63**, 054422 (2001).
[40] D. Grundler, Phys Rev B **63**, 161307 (2001).
[41] H. J. Zhu, M. Ramsteiner, H. Kostial, M. Wassermeier, H. P. Schonherr, and K. H. Ploog, Phys Rev Lett **87** (2001).
[42] A. T. Hanbicki, O. M. J. van 't Erve, R. Magno, G. Kioseoglou, C. H. Li, B. T. Jonker, G. Itskos, R. Mallory, M. Yasar, and A. Petrou, Appl Phys Lett **82**, 4092 (2003).
[43] S. A. Crooker, M. Furis, X. Lou, C. Adelmann, D. L. Smith, C. J. Palmstrom, and P. A. Crowell, Science **309**, 2191 (2005).
[44] X. H. Lou, C. Adelmann, S. A. Crooker, E. S. Garlid, J. Zhang, K. S. M. Reddy, S. D. Flexner, C. J. Palmstrom, and P. A. Crowell, Nature Physics **3**, 197 (2007).
[45] T. J. Zega, A. T. Hanbicki, S. C. Erwin, I. Zutic, G. Kioseoglou, C. H. Li, B. T. Jonker, and R. M. Stroud, Phys Rev Lett **96** (2006).
[46] J. M. Le Beau, Q. O. Hu, C. J. Palmstrom, and S. Stemmer, Appl Phys Lett **93** (2008).
[47] D. O. Demchenko and A. Y. Liu, Phys Rev B **73** (2006).
[48] B. D. Schultz, C. Adelmann, X. Y. Dong, S. McKernan, and C. J. Palmstrom, Appl Phys Lett **92** (2008).
[49] J. Moser, Appl. Phys. Lett. **89**, 162106 (2006).
[50] P. I. Good and J. W. Hardin, *Common errors in statistics (and how to avoid them)* (Wiley, Hoboken, N.J., 2009).
[51] W. Heisenberg, Z Phys **49**, 619 (1928).
[52] B. D. Cullity and C. D. Graham, *Introduction to magnetic materials* (IEEE/Wiley, Hoboken, N.J., 2009).
[53] N. W. Ashcroft and N. D. Mermin, *Solid state physics* (Holt, New York,, 1976).
[54] E. C. Stoner, Proc R Soc Lon Ser-A **169**, 0339 (1939).
[55] R. C. O'Hanley, *Modern magnetic material principles and applications* (John Wiley & Sons, New York, 2000).
[56] P. M. Tedrow and R. Meservey, Phys Rev B **7**, 318 (1973).
[57] J. S. Moodera and G. Mathon, J Magn Magn Mater **200**, 248 (1999).
[58] I. I. Mazin, A. A. Golubov, and B. Nadgorny, Journal of Applied Physics **89**, 7576 (2001).
[59] L. Lliboutry, *Quantitative geophysics and geology* (Springer, London ; New York, 2000).
[60] L. Neel, Adv Phys **4**, 191 (1955).
[61] K. K. Meng, J. Lu, S. L. Wang, H. J. Meng, J. H. Zhao, J. Misuraca, P. Xiong, and S. von Molnar, Appl Phys Lett **97**, 072503 (2010).
[62] D. L. Smith and R. N. Silver, Phys Rev B **64** (2001).
[63] F. Braun, Annalen der Physik und Chemie **229**, 556 (1875).
[64] W. Schottky, Naturwissenschaften **26**, 843 (1938).
[65] N. F. Mott, Proceedings of the Royal Society of London. Series A, Mathematical and Physical Sciences **167**, 384 (1938).
[66] W. Schottky and E. Spenke, Wiss. Veroff. Siemens Werke **18**, 1 (1939).
[67] H. A. Bethe, Massachusetts Institute of Technology Radiation Laboratory Report **43**, 12 (1942).
[68] J. Bardeen, Phys Rev **71**, 717 (1947).
[69] V. Heine, Phys Rev **138**, 1689 (1965).
[70] W. E. Spicer, P. W. Chye, P. R. Skeath, C. Y. Su, and I. Lindau, J. Vac. Sci. Technol. **16**, 1422 (1979).
[71] H. Hasegawa and H. Ohno, J Vac Sci Technol B **4**, 1130 (1986).
[72] R. T. Tung, Phys Rev B **64** (2001).

[73] C. R. Crowell and S. M. Sze, Solid State Electron **9**, 1035 (1966).
[74] F. A. Padovani and R. Stratton, Phys Rev Lett **16**, 1202 (1966).
[75] C. R. Crowell and V. L. Rideout, Appl Phys Lett **14**, 85 (1969).
[76] W. F. Brinkman, R. C. Dynes, and J. M. Rowell, J Appl Phys **41**, 1915 (1970).
[77] J. G. Simmons, J Appl Phys **34**, 2581 (1963).
[78] E. Burstein and S. Lundqvist, *Tunneling phenomena in solids; lectures* (Plenum Press, New York,, 1969).
[79] D. O. Demchenko, A. Y. Liu, E. Z. Kurmaev, L. D. Finkelstein, V. R. Galakhov, A. Moewes, S. G. Chiuzbaian, M. Neumann, C. R. Kmety, and K. L. Stevenson, Phys Rev B **69** (2004).
[80] A. N. Chantis, K. D. Belashchenko, D. L. Smith, E. Y. Tsymbal, M. van Schilfgaarde, and R. C. Albers, Phys Rev Lett **99** (2007).
[81] S. Honda, H. Itoh, and J. Inoue, Journal of Physics D: Applied Physics **43**, 135002 (2010).
[82] D. L. Smith and P. P. Ruden, Phys Rev B **78**, 125202 (2008).
[83] D. L. Smith and C. Mailhiot, Reviews of Modern Physics **62**, 173 (1990).
[84] H. Dery and L. J. Sham, Phys. Rev. Lett. **98**, 046602 (2007).
[85] P. C. van Son, H. van Kempen, and P. Wyder, Phys Rev Lett **58**, 2271 (1987).
[86] S. Hershfield and H. L. Zhao, Phys Rev B **56**, 3296 (1997).
[87] F. J. Jedema, B. J. van Wees, B. H. Hoving, A. T. Filip, and T. M. Klapwijk, Phys Rev B **60**, 16549 (1999).
[88] T. Valet and A. Fert, Phys Rev B **48**, 7099 (1993).
[89] R. I. Dzhioev, K. V. Kavokin, V. L. Korenev, M. V. Lazarev, B. Y. Meltser, M. N. Stepanova, B. P. Zakharchenya, D. Gammon, and D. S. Katzer, Phys Rev B **66**, 245204 (2002).
[90] C. Jacoboni, *Theory of electron transport in semiconductors : a pathway from elementary physics to nonequilibrium green functions* (Springer, Heidelberg ; New York, 2010).
[91] A. I. M. Rae, *Quantum mechanics* (Taylor & Francis, New York, 2008).
[92] G. Dresselhaus, Phys Rev **100**, 580 (1955).
[93] Y. A. Bychkov and E. I. Rashba, J Phys C Solid State **17**, 6039 (1984).
[94] M. I. Dyakonov, *Spin physics in semiconductors* (Springer, Berlin, 2008).
[95] F. H. L. Koppens, K. C. Nowack, and L. M. K. Vandersypen, Phys Rev Lett **100** (2008).
[96] I. Žutić, J. Fabian, and S. Das Sarma, Reviews of Modern Physics **76**, 323 (2004).
[97] F. Bloch, W. W. Hansen, and M. Packard, Phys Rev **69**, 127 (1946).
[98] D. Pines and C. P. Slichter, Phys Rev **100**, 1014 (1955).
[99] R. J. Elliott, Phys Rev **96**, 266 (1954).
[100] Y. Yafet, Solid State Phys **14**, 1 (1963).
[101] M. I. Dyakonov and V. I. Perel, Sov Phys Jetp-Ussr **33**, 1053 (1971).
[102] K. V. Kavokin, Phys Rev B **64**, 075305 (2001).
[103] A. Abragam, *The principles of nuclear magnetism* (Clarendon Press, Oxford,, 1961).
[104] A. Abragam and M. Goldman, Rep Prog Phys **41**, 395 (1978).
[105] D. Paget, Phys Rev B **25**, 4444 (1982).
[106] M. J. R. Hoch, J. Lu, P. L. Kuhns, W. G. Moulton, and A. P. Reyes, Phys Rev B **72**, 233204 (2005).
[107] G. Kaur and G. Denninger, Applied Magnetic Resonance **39**, 185 (2010).
[108] R. J. Epstein, I. Malajovich, R. K. Kawakami, Y. Chye, M. Hanson, P. M. Petroff, A. C. Gossard, and D. D. Awschalom, Phys Rev B **65**, 121202 (2002).
[109] R. J. Epstein, J. Stephens, M. Hanson, Y. Chye, A. C. Gossard, P. M. Petroff, and D. D. Awschalom, Phys Rev B **68**, 041305 (2003).
[110] S. Krishnamurthy, M. van Schilfgaarde, and N. Newman, Appl Phys Lett **83**, 1761 (2003).
[111] M. Furis, D. L. Smith, S. A. Crooker, and J. L. Reno, Appl Phys Lett **89**, 102102 (2006).

[112] M. A. Herman and H. Sitter, *Molecular beam epitaxy : fundamentals and current status* (Springer, Berlin ; New York, 1996).
[113] A. Chambers, *Modern vacuum physics* (Chapman & Hall/CRC, Boca Raton, 2005).
[114] C. Davisson and L. H. Germer, Phys Rev **30**, 705 (1927).
[115] S. Nishikawa and S. Kikuchi, Nature **122**, 726 (1928).
[116] E. N. C. f. I.-V. Technologies, http://www.epsrciii-vcentre.com/epitaxyservices.aspx?tab=1
[117] G. Wastlbauer and J. A. C. Bland, Adv Phys **54**, 137 (2005).
[118] Q. O. Hu, E. S. Garlid, P. A. Crowell, and C. J. Palmstrom, Phys Rev B **84** (2011).
[119] G. Snider, http://www.nd.edu/ gsnider/
[120] G. L. Snider, I. H. Tan, and E. L. Hu, J Appl Phys **68**, 2849 (1990).
[121] I. H. Tan, G. L. Snider, L. D. Chang, and E. L. Hu, J Appl Phys **68**, 4071 (1990).
[122] R. C. Jaeger, *Introduction to microelectronic fabrication* (Prentice Hall, Upper Saddle River, N.J., 2002).
[123] J. Pottu-Boumendil, *Microscopie électronique : principes et méthodes de préparation* (Ed. INSERM, Paris, 1989).
[124] J. Kerr, Philos. Mag. **50**, 337 (1875).
[125] M. Mansuripur, *The physical principles of magneto-optical recording* (Cambridge University Press, Cambridge ; New York, 1995).
[126] J. A. C. Bland, M. J. Padgett, R. J. Butcher, and N. Bett, J Phys E Sci Instrum **22**, 308 (1989).
[127] W. Hanle, Z Phys **30**, 93 (1924).
[128] D. B. Williams and C. B. Carter, *Transmission electron microscopy : a textbook for materials science* (Springer, New York, 2008).
[129] P. Stadelmann, http://cimewww.epfl.ch/people/Stadelmann/jemsWebSite/jems.html
[130] G. R. Anstis, Acta Crystallogr A **33**, 844 (1977).
[131] J. M. Cowley and A. F. Moodie, Acta Crystallogr **10**, 609 (1957).
[132] O. Scherzer, Optik **2**, 114 (1947).
[133] K. W. Urban, Science **321**, 506 (2008).
[134] P. W. Hawkes and E. Kasper, *Principles of electron optics* (Academic Press, London ; San Diego, 1989).
[135] O. L. Krivanek, N. Dellby, and A. R. Lupini, Ultramicroscopy **78**, 1 (1999).
[136] V. D. Beck, Optik **53**, 241 (1979).
[137] M. Haider, H. Rose, S. Uhlemann, E. Schwan, B. Kabius, and K. Urban, Ultramicroscopy **75**, 53 (1998).
[138] S. Uhlemann and M. Haider, Eur J Cell Biol **74**, 7 (1997).
[139] S. C. Erwin, S. H. Lee, and M. Scheffler, Phys. Rev. B **65**, 205422 (2002).
[140] B. D. Schultz, N. Marom, D. Naveh, X. Lou, C. Adelmann, J. Strand, P. A. Crowell, L. Kronik, and C. J. Palmstrom, Phys Rev B **80** (2009).
[141] A. Ohtake, Surf Sci Rep **63**, 295 (2008).
[142] O. Romanyuk, P. Jiříček, M. Cukr, and I. Bartoš, Czechoslovak Journal of Physics **53**, 49 (2003).
[143] B. T. Jonker, E. M. Kneedler, P. Thibado, O. J. Glembocki, L. J. Whitman, and B. R. Bennett, J Appl Phys **81**, 4362 (1997).
[144] H. Kurebayashi, S. J. Steinmuller, J. B. Laloe, T. Trypiniotis, S. Easton, A. Ionescu, J. R. Yates, and J. A. C. Bland, Applied Physics Letters **91** (2007).
[145] C. Daboo, R. J. Hicken, E. Gu, M. Gester, S. J. Gray, D. E. P. Eley, E. Ahmad, J. A. C. Bland, R. Ploessl, and J. N. Chapman, Phys Rev B **51**, 15964 (1995).
[146] G. Wedler, B. Wassermann, R. Notzel, and R. Koch, Appl Phys Lett **78**, 1270 (2001).
[147] G. Wedler, B. Wassermann, and R. Koch, Phys Rev B **66**, 064415 (2002).
[148] R. Moosbuhler, F. Bensch, M. Dumm, and G. Bayreuther, J Appl Phys **91**, 8757 (2002).
[149] R. Koch, J Phys-Condens Mat **6**, 9519 (1994).

[150] S. P. Dash, S. Sharma, J. C. Le Breton, J. Peiro, H. Jaffres, J. M. George, A. Lemaitre, and R. Jansen, Phys Rev B **84** (2011).
[151] C. Awo-Affouda, O. M. J. van 't Erve, G. Kioseoglou, A. T. Hanbicki, M. Holub, C. H. Li, and B. T. Jonker, Appl Phys Lett **94**, 102511 (2009).
[152] L. R. Fleet, K. Yoshida, H. Kobayashi, Y. Ohno, H. Kurebayashi, J. Y. Kim, C. H. W. Barnes, and A. Hirohata, Ieee T Magn **46**, 1737 (2010).
[153] L. R. Fleet, H. Kobayashi, Y. Ohno, and A. Hirohata, Ieee T Magn **47**, 2756 (2011).
[154] J. M. Kikkawa, I. P. Smorchkova, N. Samarth, and D. D. Awschalom, Science **277**, 1284 (1997).
[155] M. Furis, D. L. Smith, S. Kos, E. S. Garlid, K. S. M. Reddy, C. J. Palmstrom, P. A. Crowell, and S. A. Crooker, New J Phys **9** (2007).
[156] S. Takahashi and S. Maekawa, Sci Technol Adv Mat **9** (2008).
[157] M. Furis, D. L. Smith, S. Kos, E. S. Garlid, K. S. M. Reddy, C. J. Palmstrøm, P. A. Crowell, and S. A. Crooker, New Journal of Physics **9**, 347 (2007).
[158] Z. G. Yu and M. E. Flatté, Physical Review B **66**, 235302 (2002).
[159] A. T. Hanbicki and B. T. Jonker, Applied Physics Letters **81**, 2131 (2002).
[160] A. T. Hanbicki, B. T. Jonker, G. Itskos, G. Kioseoglou, and A. Petrou, Applied Physics Letters **80**, 1240 (2002).
[161] R. Jansen, Applied Physics Letters **81**, 2130 (2002).
[162] S. P. Dash, S. Sharma, R. S. Patel, M. P. de Jong, and R. Jansen, Nature **462**, 491 (2009).
[163] A. Hirohata, A. Kikuchi, N. Tezuka, K. Inomata, J. S. Claydon, Y. B. Xu, and G. van der Laan, Curr Opin Solid St M **10**, 93 (2006).
[164] I. Galanakis, P. H. Dederichs, and N. Papanikolaou, Phys Rev B **66**, 174429 (2002).
[165] T. Block, C. Felser, G. Jakob, J. Ensling, B. Muhling, P. Gutlich, and R. J. Cava, J Solid State Chem **176**, 646 (2003).
[166] Y. Sakuraba, J. Nakata, M. Oogane, H. Kubota, Y. Ando, A. Sakuma, and T. Miyazaki, Jpn J Appl Phys 1 **44**, 6535 (2005).
[167] N. Tezuka, N. Ikeda, F. Mitsuhashi, and S. Sugimoto, Appl Phys Lett **94**, 162504 (2009).
[168] T. Marukame, T. Ishikawa, T. Taira, K. Matsuda, T. Uemura, and M. Yamamoto, Phys Rev B **81**, 134432 (2010).
[169] R. Shan, H. Sukegawa, W. H. Wang, M. Kodzuka, T. Furubayashi, T. Ohkubo, S. Mitani, K. Inomata, and K. Hono, Phys Rev Lett **102**, 246601 (2009).
[170] I. Galanakis and P. H. Dederichs, *Half-metallic alloys : fundamentals and applications* (Springer, Berlin ; New York, 2005).
[171] M. Vopsaroiu, G. V. Fernandez, M. J. Thwaites, J. Anguita, P. J. Grundy, and K. O'Grady, J Phys D Appl Phys **38**, 490 (2005).
[172] M. Vopsaroiu, M. J. Thwaites, S. Rand, P. J. Grundy, and K. O'Grady, Ieee T Magn **40**, 2443 (2004).
[173] A. Hirohata, S. Ladak, N. P. Aley, and G. B. Hix, Appl Phys Lett **95**, 252506 (2009).
[174] J. Sagar, L. R. Fleet, A. Hirohata, and K. O'Grady, Ieee T Magn **47**, 2440 (2011).
[175] L. R. Fleet, G. Cheglakov, K. Yoshida, V. K. Lazarov, T. Nakayama, and A. Hirohata, Journal of Physics D: Applied Physics **45**, 032001 (2012).
[176] L. R. Fleet, H. Kobayashi, Y. Ohno, J. Y. Kim, C. H. W. Barnes, and A. Hirohata, J Appl Phys **109** (2011).
[177] A. Grunebohm, H. C. Herper, and P. Entel, Phys Rev B **80** (2009).
[178] C. H. Li, G. Kioseoglou, O. M. J. van 't Erve, A. T. Hanbicki, B. T. Jonker, R. Mallory, M. Yasar, and A. Petrou, Appl Phys Lett **85**, 1544 (2004).

List of Publications

1. L. R. Fleet, K. Yoshida, H. Kobayashi, Y. Ohno, H. Kurebayashi, K. Jun-Young, C. H. W. Barnes and A. Hirohata
"Schottky barrier height in Fe/GaAs films"
IEEE transactions on Magnetics **46**, 1737 (2010)

2. L. R. Fleet, H. Kobayashi, Y. Ohno, K. Jun-Young, C. H. W. Barnes and A. Hirohata
"Interface structure and transport properties of Fe/GaAs(001)"
Journal of Applied Physics **109**, 07C504 (2011)

3. H. Endo, A. Hirohata, J. Sagar, L. R. Fleet, T. Nakayama and K. O'Grady
"Effect of grain size on exchange-biased Heusler alloys"
J. Phys D: Appl. Phys. **44***,* 345003 (2011)

4. L. R. Fleet, H. Kobayashi, Y. Ohno, K. Jun-Young, C. H. W. Barnes and A. Hirohata
"Atomic interface structures in Fe/GaAs films"
IEEE transactions on Magnetics **47**, 2756 (2011)

5. J. Sagar, L. R. Fleet, K. O'Grady, and A. Hirohata
"Activation Volumes in Heusler Alloy Thin Films"
IEEE transactions on Magnetics **47**, 2440 (2011)

6. L. R. Fleet, G. Cheglakov, K. Yoshida, V.K. Lazarov, K. O'Grady, T. Nakayama and A. Hirohata
"Sub-micron size Co_2FeSi Heusler Alloy nano-particle formation and magnetic characterization"
*J. Phys. D: Appl. Phys.***45**, 032001 (2012)

7. Y.-J. Bae, N.-J. Lee, T.-H. Kim, H. Cho, C. Lee, L.R. Fleet, and A. Hirohata
"Effect of thin MgO(001) layer on thermal stability of Cu-Phthalocyanine for charge injection into top emitting OLED"
Submitted for publication

8. H. Endo, A. Hirohata, J. Sagar, L. R. Fleet, T. Nakayama and K. O'Grady
"Effect of Interface Structure on Exchange Biased Heusler Alloy Films"
Accepted for publication in IEEE transactions on Magnetics

9. M. Rummey, L. R. Fleet, Z. Xinyang, H. Hong and A. Hirohata
"Magnetic properties of epitaxial co-evaporated Fe:MgO anti-granular films"
Accepted for publication in IEEE transactions on Magnetics

10. L. R. Fleet, K. Yoshida, H. Kobayashi, Y. Kaneko, Y. Ohno, S. Honda, J. Inoue and A. Hirohata
"Observation of the abrupt Fe/GaAs(001) interface"
Submitted for publication

List of Presentations

1. L. R. Fleet, K. Yoshida, H. Kobayashi, Y. Ohno, H. Kurebayashi, K. Jun-Young, C. H. W. Barnes and A. Hirohata
   "Schottky barrier height in Fe/GaAs films"
   Presented at **11th Joint MMM–Intermag Conference** 2010, Washington, DC, USA (**BE-09**)

2. L. R. Fleet, H. Kobayashi, Y. Ohno, K. Jun-Young, C. H. W. Barnes and A. Hirohata
   "Interface structure and transport properties of Fe/GaAs(001)"
   Presented at **55th MMM conference** 2010, Atlanta, Georgia USA (**BD-06**)

3. N. Lee, Y. Bae, J. Lee, H. Cho, C. Lee, A. Hirohata, L.R. Fleet and T. Kim
   "Magneto-optoelectronic properties of Fe/MgO/CuPC heterostructures"
   Presented at **55th MMM conference** 2010, Atlanta, Georgia USA (**BR-06**)

4. Y. Bae, N. Lee, T. Kim, J. Lee, H. Cho, C. Lee, L.R. Fleet and A. Hirohata
   "Spin dependent Transport Properties in Fe/MgO(100)/CuPC/Py Hetero Tunnel Junctions"
   Presented at **55th MMM conference** 2010, Atlanta, Georgia USA (**DT-13**)

5. L. R. Fleet, H. Kobayashi, Y. Ohno, K. Jun-Young, C. H. W. Barnes and A. Hirohata
   "Correlations between atomic interface structures and transport properties in Fe/GaAs films"
   Presented at **Intermag conference** 2011, Taipei, Taiwan (**BP-12**)

6. L. R. Fleet, G. Cheglakov, K. Yoshida, V.K. Lazarov, K. O'Grady, T. Nakayama and A. Hirohata
   "Sub-micron size Co_2FeSi Heusler Alloy nano-particle formation and magnetic characterization"
   Presented **at Intermag confer**ence 2011, Taipei, Taiwan (**AO-08**)

7. J. Sagar, L. R. Fleet, K. O'Grady, and A. Hirohata
   "Activation Volumes in Heusler Alloy Thin Films"
   Presented at **Intermag conference** 2011, Taipei, Taiwan (**AO-09**)

8. H. Endo, A. Hirohata, J. Sagar, L. R. Fleet, T. Nakayama and K. O'Grady
   "Effect of grain size on exchange-biased Heusler alloys"
   Presented at **Intermag conference** 2011, Taipei, Taiwan (**AO-07**)

9. L. R. Fleet, K. Yoshida, H. Kobayashi, Y. Kaneko, Y. Ohno, and A. Hirohata
   "Observation of the Abrupt Fe/GaAs(001) Interface
   Presented at **56th MMM conference** 2011, Scottsdale, Arizona USA (**BS-08**)

10. Hirohata, L.R. Fleet, M.J. Walsh, J. Sagar, G. Cheglakov, K. Yoshida, V.K. Lazarov, Y. Ohba and T. Nakayama.
"Crystalline formation of Polycrystalline Co-based full Heusler alloy films observed by HRTEM with in-situ annealing (invited)"
Presented at **56th MMM conference** 2011, Scottsdale, Arizona USA (**AA-02**)

11. N. Lee, Y. Bae, T. Kim, H. Cho, C. Lee, L.R. Fleet, A. Hirohata and E. Ito
"Tailoring and understanding Metal/Organic Semiconductor interfaces using a thin oxide layer"
Presented at **56th MMM conference** 2011, Scottsdale, Arizona USA (**BR-14**)

12. L.R. Fleet, K. Yoshida, H. Kobayashi, Y. Kaneko, Y. Ohno, S. Honda, J. Inoue and A. Hirohata
"The interface structure and transport properties of Fe/GaAs(001) heterostructures"
Presented at **CMMP conference**, Manchester UK (**P.045**)

13. J. Sagar, H. Sukegawa, L.R. Fleet, L. Lari, V.K. Lazarov, S. Mitani and A. Hirohata
"Structure and compositional characterisation of single crystal and polycrystalline Co_2FeSi Heusler alloy thin films"
Presented at **CMMP conference**, Manchester UK

14. L.R. Fleet, K. Yoshida, H. Kobayashi, Y. Kaneko, Y. Ohno, S. Honda, J. Inoue and A. Hirohata
"Spin injection across abrupt Fe/GaAs(001) interfaces"
Presented at **Intermag conference** 2012, Vancouver, Canada (**AD-02**)

15. L.R. Fleet, M.J. Walsh, J. Sagar, T. Nakayama and A. Hirohata
"Low temperature in-situ crystallisation of Co_2FeSi Heusler alloy thin films"
Presented at **Intermag conference** 2012, Vancouver, Canada (**EB-09**)

16. H. Endo, A. Hirohata, J. Sagar, L. R. Fleet, T. Nakayama and K. O'Grady
"Effect of Interface Structure on Exchange Biased Heusler Alloy Films"
Presented at **Intermag conference** 2012, Vancouver, Canada (**AR-08**)

17. M. Rummey, L. R. Fleet, H. Hing, X. Zhang and A. Hirohata
"Magnetic properties of epitaxial co-evaporated Fe:MgO anti-granular films"
Presented at **Intermag conference** 2012, Vancouver, Canada (**FU-13**)

18. L.R. Fleet, K. Yoshida, H. Kobayashi, Y. Kaneko, Y. Ohno, S. Honda, J. Inoue and A. Hirohata
"The effect of an inhomogeneous interface on the transport properties across Fe/GaAs(001) films"
Presented at **ICM conference** 2012, Busan, Korea (**CG-02**)

19. L.R. Fleet, M.J. Walsh, J. Sagar, T. Nakayama and A. Hirohata
"Low temperature crystallization process in Co2FeSi Heusler alloy thin films"
Presented at **ICM conference** 2012, Busan, Korea (**SK-03**)